July 2018

Estimation of CDOM in Inland Waters via Water Bio-Optical Properties Using a Remote Sensing Approach

Jiwei Li
University of Massachusetts Amherst

Recommended Citation

Li, Jiwei, "Estimation of CDOM in Inland Waters via Water Bio-Optical Properties Using a Remote Sensing Approach" (2018). *Doctoral Dissertations*. 1278.
https://scholarworks.umass.edu/dissertations_2/1278

ESTIMATION OF CDOM IN INLAND WATERS VIA WATER BIO-OPTICAL PROPERTIES USING A REMOTE SENSING APPROACH

A Dissertation Presented

by

JIWEI LI

Submitted to the Graduate School of the
University of Massachusetts Amherst in partial fulfillment
of the requirements for the degree of

DOCTOR OF PHILOSOPHY

May 2018

Geosciences

ESTIMATION OF CDOM IN INLAND WATERS VIA WATER BIO-OPTICAL PROPERTIES USING A REMOTE SENSING APPROACH

A Dissertation Presented

by

JIWEI LI

Approved as to style and content by:

____
Qian Yu, Chair

____
Steve Petsch, Member

____
Paul Siqueira, Member

____
Donghui Yan, Member

____
Julie Brigham-Grette, Department Head
Department of Geosciences

DEDICATION

To my supportive & lovely wife
and my energetic son

ACKNOWLEDGMENTS

I would like to express my greatest gratitude to my advisor, my dissertation committee members, my collaborators, my friends, and my family. This dissertation cannot be done without all their guide, help and support.

First, I would like to thank my advisor, Dr. Qian Yu for being an excellent model as researcher, teacher, and mentor. Her advice, guidance, patience, and finical support made me to be a much better thinker and researcher over years. Her office door was always open to my questions in paper, proposal, and presentation. I believe her advice will be always precious through my life.

I also appreciate my dissertation committee members. Dr. Steve Petsch, for his taught in Organic Geochemistry course, serving in the Ph.D. comprehensive exam, advice in dissertation prospectus. Dr. Paul Siqueira, for his comment on the research proposal, the suggestion in scientific writing, advice in dissertation prospectus. Dr. Donghui Yan, for his advice on statistical issues and suggestion in dissertation prospectus. I also thank Dr. David Boutt, Dr. Laurie Brown and Dr. Michael Rawlins, for serving on my Ph.D. comprehensive exam committee. I would like to thank many other faculty, students, and staff in the Department of Geosciences for their numerous help in the past years.

I would like to give sincere thanks to the project PI, Dr. Yong Tian, for his great help and suggestion in scientific writing, discussion, experimental design, biological experiment, and field sampling. I also want to thank all my collaborators, including Dr. Brian Becker, Dr. Weining Zhu, Mr. Changjiang Ye, and Ms. Huijiao Qiao.

I want to express my deepest gratitude to my wife, Rong Chen, for her support and love. She gave up her own career for helping me to chase my dream. I gained the endless support from her. I would like to thank my aunt, Dr. Xiaojuan Li, for helping and encouraging me to choose an academic career. The understandings of my parents always encouraged me. At last, I should also thank my son, Jason, for letting me learn to be much more patient with any challenges.

ABSTRACT

ESTIMATION OF CDOM IN INLAND WATERS VIA WATER BIO-OPTICAL PROPERTIES USING A REMOTE SENSING APPROACH

MAY 2018

JIWEI LI, B.S., NORTHWEST UNIVERSITY, CHINA

M.S., CAPITAL NORMAL UNIVERSITY, CHINA

Ph.D., UNIVERSITY OF MASSACHUSETTS AMHERST

Directed by: Professor Qian Yu

Monitoring of Colored dissolved organic matter (CDOM) in inland waters provides important information for tracing carbon cycle at the land-water interface and studying aquatic ecosystem. Remote sensing estimation of CDOM in the inland waters offers an alternative approach to field samplings in examining CDOM spatial-temporal dynamics. However, CDOM retrieval is a challenge due to the lack of algorithm for resolving bottom effect in shallow inland waters. Moreover, an effective approach based on multi-spectral, high spatial resolution and global coverage satellite images is in urgent need. To resolve these challenges, shallow water bio-optical properties (SBOP) algorithm was developed to overcome bottom reflectance effect on the total water leaving reflectance in shallow inland water. SBOP algorithm included the bottom reflectance in building underwater light transfer model. It was designed based on the field spectral data from four cruises in Lake Huron. SBOP algorithm had an obviously advantage over previous deep water CDOM algorithm (e.g. QAA-CDOM). In this study, Landsat-8 multi-spectral satellite imagery was selected to derive CDOM spatial-temporal dynamics in lake and river waters. The coastal blue band (443 nm), global coverage and high spatial resolution (30 m) of Landsat-8 images offered suitable data for inland water CDOM mapping. The SBOP algorithm was applied on Landsat-8 images in broad ranges of inland waters with high accuracy (Lake Huron (R^2 = 0.87), 14 northeastern freshwater lakes (R^2 = 0.80), and 6 large Arctic Rivers (R^2 = 0.87)). Both the spatial patterns and seasonal dynamics were derived to study the multiple factors' impact on terrestrially derived CDOM input to the rivers and lakes, including river discharge, watershed landcover, and temperature. This new satellite approach of CDOM estimation in inland waters provided high accuracy spatial-temporal information for studying land-water carbon cycle and aquatic environment.

TABLE OF CONTENTS

Page

LIST OF TABLES

Table Page

LIST OF FIGURES

CHAPTER 1

BACKGROUND

1.1 Colored dissolved organic matter

Colored dissolved organic matter (CDOM) is defined as the photoactive portion of dissolved organic matter (DOM) (Brando and Dekker 2003). The ‘dissolved’ represents the small physical size of CDOM that it could pass through 0.7 µm-pore size filter (or 0.2 µm in some studies) (Mannino et al. 2008). This small size allowed CDOM to well mix in the natural waters. The ‘colored’ represents its optical properties, the most notable feature of CDOM. It could be used to quantify CDOM level through the optical measurements, including lab measurement and remote sensing estimation (Del Vecchio and Blough 2002). This absorption property of CDOM was often used by remote sensing community (Blough and Del Vecchio 2002). The CDOM light absorption is represented by strong absorption in UV and blue wavelengths, and sharp decrease through visible wavelength to minimal at a longer wavelength (Del Castillo et al. 1999). Because the strongest absorption of CDOM was from UV and blue bands, the 440 nm was often selected by many previous studies. Moreover, this band is available from many satellite sensors (Rochelle-Newall and Fisher 2002). Therefore, $a_{cdom}(440)$ was generally adopted in current remote sensing studies to indicate the CDOM level in the waters.

The previous CDOM remote sensing product were mostly made as one of the productions of ocean color algorithms (Carder et al. 2004; Maritorena et al. 2010; O'Reilly et al. 1998). In the ocean color studies, the major efforts were made on the deriving of ***Chl-a or phytoplankton*** because they have strong reflectance signals and easy to derive from the simple empirical algorithm. Also, the remote sensing of phytoplankton was the mainstream because of its strong relationship to the sea surface temperature. The phytoplankton is used as an indicator of the climate change (Babin et al. 2003b; Diehl 2002; Larkum and Wood 1993; Meon and Kirchman 2001). Remote sensing of CDOM has not been well studied by the ocean color community. The normal ocean color algorithm often derived the combined absorption of CDOM and non-algae particles as colored dissolved and detrital material absorption (CDM) (Dall'Olmo et al. 2005; Darecki and Stramski 2004; Gordon and Wang 1994; O'Reilly et al. 1998; O’Reilly et al. 2000). Until very recently, more attention of CDOM estimation was moved from open ocean to the inland waters (Chen et al. 2017; Frey et al. 2016; Kutser et al. 2016a; Kutser et al. 2016b; Yang et al. 2015; Zhu et al. 2014).

CDOM in ***inland waters***, including the streams, rivers, and lakes, had significant implications for both land-water carbon cycle and inland aquatic environment (Brezonik et al. 2015). DOC transport from land to water represents one active carbon exchange pathway at the land-water interface (Butman and Raymond 2011). Many previous studies had confirmed the inland water CDOM was highly correlated to DOC where the conservative terrestrially derived DOM was the major sources (Del Castillo et al. 1999; Del Castillo and Miller 2008; Del Vecchio and Blough 2004; Ferrari et al. 1996; Hestir et al. 2015; Kowalczuk et al. 2003; Sand-Jensen and Staehr 2009; Stedmon et al. 2006). Therefore, CDOM could be applied as the tracer for monitoring the transport of terrestrial DOC from land to aquatic environment through the remote sensing approach (Mannino et al. 2008).

CDOM in the inland waters also impacts ***inland aquatic ecosystems*** in different aspects (Williamson et al. 1999). CDOM in the waters has strong absorption in UV and blue light which would affect underwater light intensity and consequently impact the growth of plankton in the lake environment (Diehl 2002; Williamson et al. 1996). Meanwhile, the terrestrial CDOM in lake waters represent important DOM sources as joining in the food web in lake ecosystems (Cole et al. 2006). Lake waters were also important drinking water sources. According to the statistics data from U.S. Environmental Protection Agency (EPA), nearly 68% of total drinking waters of community consumption came from the lake waters (EPA 2008). The estimation of lake water CDOM could provide useful knowledge for monitoring and treatment of drinking water (Baghoth et al. 2011; Matilainen et al. 2010).

1.2 Water optical components

When light penetrates water surface, it interacts with water-self and different components in natural waters. The different ***water color components***, including phytoplankton, non-algae particles, CDOM, and pure water together determine the underwater light field (Mobley 1994). These natural water components absorb (phytoplankton, non-algae particles, CDOM, and water) or scatter (phytoplankton, non-algae particles, and water) the light under the water surface to determine underwater light transfer (Mobley et al. 1993). The remote sensing estimation of water bio-optical properties is aiming to invert these water inherent properties (absorption and scattering) so as to quantify water components.

Among all the water color components, phytoplankton was the major target in the water color studies. ***Phytoplankton*** is the major component in the aquatic food web and basic member in aquatic ecosystem and global carbon cycle (Jansson et al. 2000). Phytoplankton photosynthesis absorbs sunlight to produce organic material, releasing oxygen and exchange CO_2 through its internal chlorophyll (Falkowski and Raven 2013). Chlorophyll and other pigments (carotenoids, billiproteins) impact the optical properties of the phytoplankton. The chlorophyll is often used in the water color studies to represent the phytoplankton because it is the most important and major pigment in phytoplankton cell (Bricaud et al. 1998; Carder et al. 1999; Dall'Olmo et al. 2005; Gons et al. 2008; Kahru and Mitchell 2001; Kowalczuk et al. 2006; Le et al. 2013; O’Reilly et al. 2000). The dominant absorption peaks of chlorophyll is at blue and red wavelength. These absorption features of chlorophyll formed the remote sensing estimation foundations (Dierssen 2010; Gregg et al. 2005; Ruddick et al. 2001).

Non-algae particles is domantly inorganic particles in the diverse natural waters (Babin et al. 2003a). Numerous components in the waters could be included as the non-algae particles, including bacteria, zooplankton, and mineral particles (Babin et al. 2003b; Bricaud et al. 1998; Doxaran et al. 2012). Non-algae particles absorbed and backscattered underwater light and had similar absorption characters as CDOM and scattering. Non-algae particles were also found highly related to the suspended particulate matter, especially in river plume and coastal water regions (Bricaud et al. 1998; Doxaran et al. 2002; Giardino et al. 2015; Miller and McKee 2004; Volpe et al. 2011).

Water also contributes to both light absorption and scattering. Water effects in both ocean and inland waters generally cannot be ignored due to its contribution to light attenuation. The water absorption and backscattering to light significantly increases from red to NIR bands. Although absorption and scattering properties of water were slightly affected by salinity and temperature, these parameters were used the constant empirical values in building the water optical properties model (Morel 1974; Pope and Fry 1997).

1.3 Radiative transfer from top of atmosphere to sensor radiance

Sunlight offers energy for the photosynthesis of aquatic environment. It also could be applied to derive the information of water bio-optical properties for remote sensing estimation. ***Solar radiation*** transfers from top of the atmosphere to the bottom of inland waters, and transfers back through water and atmosphere. Then it is received by sensor. During this radiative transfer, the light was absorbed and scattered by both atmosphere and aquatic environment. The atmospheric correction is an pre-processing procedure in aquatic remote sensing (Gordon 1997). This process aims to extract water-leaving radiance from top-of-atmosphere (TOA) radiance based on different empirical and optical models (Siegel et al. 2000). Non-water contribution portions, including Rayleigh scattering, aerosols scattering, sun glint, surface reflectance, and whitecap, need to be removed from satellite images.

Previous ***atmospheric correction methods*** mainly focus on chlorophyll dominated waters in open ocean regions (Case-1 waters) (Hu et al. 2000; Jamet et al. 2011; Ruddick et al. 2000). In clean open ocean waters (Case-1 waters), the NIR band of water leaving radiance are almost negligible so that the atmospheric effect can be estimated through these bands (Jamet et al. 2011). However, the inland waters (Case-2 waters) are not “dark” at NIR bands due to rich suspended sediments. Moreover, the high CDOM level in Case-2 waters leads to high absorption in blue bands, so the satellite sensors receive extremely low upwelling radiance at these bands (Shi and Wang 2014; Vanhellemont and Ruddick 2014). Therefore, it is essential to examine current empirical and radiative transfer-based atmosphere correction models for inland waters.

Water inherent optical properties were independent of the sunlight. So ***apparent optical properties (AOPs)*** were introduced by the water color community to describe the properties determined by both water body and directional radiance distribution (Mobley 1995). One of the most important AOPs is remote sensing reflectance (R_{rs}). It is the principal information can be extracted from field measured spectra data and satellite images. The inversion of water IOPs is a computation process for retrieving water IOPs from AOPs, particularly R_{rs}. In the aquatic remote sensing, the R_{rs} is generally caculated from the upwelling radiance (L_t), sky radiance (L_s) and the downwelling irradiance (E_d) as:

$$R_{rs} = \frac{L_t - \phi L_s}{E_d} \qquad (1)$$

Where the ϕ is empirical factor for calculating the water surface reflectance from the sky radiance. The value of the ϕ was set as 0.028 (Mobley 1999). Then the R_{rs} was applied to calculate below-surface remote sensing reflectance r_{rs} as following (Lee et al. 1998):

$$r_{rs}(\lambda) = \frac{R_{rs}(\lambda)}{0.52 + 1.7 R_{rs}(\lambda)} \qquad (2)$$

Radiance received by the sensor is contributed by both water column and ***bottom in shallow inland waters***. In previous open ocean color studies, waters are assumed to be optically deep, and bottom reflectance is often ignored (Stedmon et al. 2000). However, this assumption is often not valid for shallow inland waters because the total water leaving reflectance was contributed by bottom reflectance (Aitkenhead-Peterson et al. 2003a). Therefore, in shallow water regions, below-surface remote sensing reflectance needs to be considered as two separate parts: one is water column, and the other is bottom sediments. Also, the bottom reflectance was also absorbed and scattered by water components when it transferred back to the water surface. The contamination of bottom reflectance will cause high uncertainty if simply applying current ocean color algorithms (Volpe et al. 2011). Moreover, the current semi-analytical algorithms were originally calibrated by *in situ* data collected in coastal regions (Brando and Dekker 2003). Accordingly, it is a key issue to develop CDOM retrieval algorithm which can be applied in shallow inland waters.

1.4 CDOM retrieval algorithms by remote sensing

The ***empirical approach*** estimates CDOM absorption by using R_{rs} band ratios. Regression coefficients are often calibrated with field measurements at specific locations (Cory et al. 2014; Morel and Gentili 2009). For instance, Morel and Gentili (2009) quantified monthly CDOM level in open ocean waters from SeaWiFS images as $(R_{rs}(412)/R_{rs}(443))/\ (R_{rs}(490)/R_{rs}(555))$. In another research, CDOM was derived from band ratio $R_{rs}(443)/R_{rs}(540)$ in the California coast regions, where remarkable increases of chlorophyll and CDOM were observed during a La Niña year (Kahru and

Mitchell 2001). Similarly, $a_g(412)$ calculated from band ratio $R_{rs}(412)/R_{rs}(555)$ has been applied to study CDOM dynamics response to river discharge in the Mississippi River plume (D'Sa and Miller 2003). Kutser et al. (2016a) applied ***band ratio*** between green to red to derive the carbon content in Estonian lake waters. Olmanson et al. (2016) performed the band ratio of ($5.13(R_{rs}(550)/R_{rs}(640))^{-2.67}$) to estimate the lake water CDOM spatial dynamics in Minnesota State. Cherukuru et al. (2016) generated the CDOM absorption in turbid coastal waters by using the ratio of $R_{rs}(412)/R_{rs}(448)$ to examine river flood effects on the CDOM input to the ocean. Chen et al. (2017) designed exponential model of ($(40.75 * \exp(-2.46 * \frac{R_{rs}(550)}{R_{rs}(640)}))$ for studying the potential of Landsat-8 satellite estimation of CDOM in inland waters. Cao et al. (2018) used the band ratio $R_{rs}(443)/R_{rs}(555)$ to derive the CDOM absorption in Chesapeake Bay for examining tidal effects on CDOM dynamics. As the empirical coefficients change across locations and over seasons, the algorithms cannot be simply applied from one study site to another. Therefore, more robust algorithms based on semi-analytical, bio-optical model have been developed to retrieve water IOPs.

In the past decade, there is a handful ***semi-analytical water color algorithms*** developed to derive water absorption, including Garver-Siegel-Maritorena (GSM) and quasi-analytical algorithm (QAA) (Lee et al. 2002). The GSM model is based on the quadratic relationship between R_{rs} and water IOPs, designed for deep ocean waters (Maritorena et al. 2010). Along with a few other algorithms, GSM is limited to open oceans and has high uncertainly when applied to coastal and inland waters (Zhu and Yu 2013). In contrast, QAA is a widely used semi-analytical method which can be applied in both coastal and inland waters (Matsuoka et al. 2013). Based on the framework of QAA, Zhu et al. (2011) presented the first semi-analytical algorithm QAA-CDOM to invert CDOM absorption based on absorption-backscattering relationship from EO-1 Hyperion satellite images. Shanmugam (2011) developed a method to derive CDOM absorption by establishing a quantitative relationship between $a_g(\lambda)$ and exponential fit of spectral slope (S) of CDOM from SeaWiFS images. Watanabe et al. (2016) optimized the parameters of QAA algorithm for detecting CDOM in eutrophic lake waters. Matsuoka et al. (2017) Derived the CDOM dynamics based on optimized GSM model in Arctic coastal regions for examining river export effects on CDOM dynamics. However, all these semi-analytical algorithms have not including the bottom reflectance in the calculating of the CDOM absorption. Suitable semi-analytical algorithm for the shallow inland waters need to be developed.

Several water remote sensing studies have considered the ***bottom effects***, including the water depth measurements (Brando et al. 2009; Majozi et al. 2014; Maritorena et al. 1994; Zhao et al. 2013), the estimation of the bottom sediments properties (Klonowski et al. 2007; Lee et al. 2013; Thompson et al. 2017), and the monitoring of the water body attenuation coefficient (Barnes et al. 2014; Barnes et al. 2013; Dekker et al. 2011; Giardino et al. 2015; Volpe et al. 2011). For instance, Dekker et al. (2011) derived the depth of the shallow waters by considering the bottom reflectance in the under-water radiative transfer model. Barnes et al. (2014) analysis the diffuse attenuation of light in the underwater light field by considering bottom reflectance contribution in shallow coastal waters. Lee et al. (2013) designed hyperspectral optimization processing exemplar (HOPE) method to derived bottom reflectance for shallow waters, but this method derived the combined absorption of CDOM and non-algal particle, rather than CDOM. Thompson et al. (2017) Used Bayesian optimal estimation for mapping the benthic reflectance features in the shallow coastal regions. In these studies, bottom reflectance has been included to develop the algorithms. These studies inspired me to develop a new CDOM estimation method by considering the bottom reflectance in the total upwelling radiance in the optically shallow waters.

1.5 Satellite sensors for CDOM observation

The remote sensing estimation of inland lakes and rivers needs the satellite images have both ultra-blue bands and suitable spatial resolutions. The ultra-blue wavelength (e.g., 440nm) is required for detecting the water-leaving radiance to build an underwater bio-optical model (Lee et al. 2002). So previous studies often assessed ***ocean satellite sensors***, such as MODIS, EO-1 Hyperion, and SeaWiFS to derive the ocean colors (Kutser et al. 2005; Miller and McKee 2004; O'Reilly et al. 1998). These images are not sufficient enough to be applied in inland waters CDOM retrieval. Global coverage sensor MODIS (500m) is too coarse to observe inland waters. Inland rivers and streams built the important transport system for carrying the terrestrial CDOM (Allen and Pavelsky 2015). The widths of these CDOM input pathway were less than two kilometers. Although experimental imagery sensors EO-1 Hyperion had the high spatial resolution, it isn’t operational now, and its spatial coverage is too narrow to cover relative large inland lakes and to monitor CDOM transport along the rivers (Zhu and Yu 2013).

Until recent years, several ***multi-spectral terrestrial-view satellite*** imagery sensors offered new coastal blue band which provided an opportunity for inland water CDOM estimation, like Landsat-8 images with 30 m spatial resolution (Roy et al. 2014). The 30 m spatial resolution would greatly expand geographic regions to rivers and lakes for satellite estimation of water bio-optical properties (Pahlevan et al. 2014). Also, the new coastal blue bands of the Landsat-8 satellite image also provide the key bands for the CDOM estimation. A couple of empirical algorithms have used Landsat-8 images as the sources for deriving the inland water CDOM through the band ratio methods (Chen et al. 2017; Kutser et al. 2016a). However, semi-analytical CDOM retrieval algorithm, including atmospheric correction, need to be exploited for multispectral images.

CHAPTER 2

REMOTE SENSING ESTIMATION OF CDOM IN OPTICALLY SHALLOW WATERS

2.1 Abstract

It is not well understood how bottom reflectance of optically shallow waters affects the algorithm performance of colored dissolved organic matters (CDOM) retrieval. This chapter proposes a new algorithm that considers bottom reflectance in estimating CDOM absorption from optically shallow inland or coastal waters. The field sampling was conducted during four research cruises within the Saginaw River, Kawkawlin River and Saginaw Bay of Lake Huron. A stratified field sampling campaign collected water samples, determined the depth at each sampling location and measured optical properties. The sampled CDOM absorption at 440nm broadly ranged from 0.12 to 8.46 m^{-1}. Field sample analysis revealed that bottom reflectance does significantly change water apparent optical properties. We developed a CDOM retrieval algorithm (Shallow water Bio-Optical Properties algorithm, SBOP) that effectively reduces uncertainty by considering bottom reflectance in shallow waters. By incorporating the bottom contribution in upwelling radiances, the SBOP algorithm was able to explain 74% of the variance of CDOM values (RMSE = 0.22 and R2 = 0.74). The bottom effect index (BEI) was introduced to efficiently separate optically shallow and optically deep waters. Based on the BEI, an adaptive approach was proposed that references the amount of bottom effect in order to identify the most suitable algorithm (optically shallow water algorithm [SBOP] or optically deep water algorithm [QAA-CDOM]) to improve CDOM

estimation (RMSE = 0.22 and R2 = 0.81). Our results potentially help to advance the capability of remote sensing in monitoring carbon pools at the land-water interface.

2.2 Introduction

Inland waters (streams, rivers and lakes) are responsible for transporting and transforming large amounts of carbon from terrestrial ecosystems to aquatic environments (Tranvik 2014). Each year, inland waters emit about 1 gigaton of carbon as CO_2 to the atmosphere and transfer an equivalent amount of carbon to ocean waters (Battin et al. 2009). This flux is larger than originally estimated and more than half of it results from the movement of dissolved organic carbon (DOC) from terrestrial environments (Stedmon et al. 2000). Accordingly, riverine systems (streams and rivers) govern much of the DOC export from terrestrial to aquatic environments (IPCC 2007) and dictate the spatial and temporal variability of freshwater DOC in drainage watersheds. Shallow coastal and estuarine areas are the primary interface regions for carbon exchange from terrestrial to aquatic ecosystems. The variations of terrestrial carbon exports in these regions are heavily associated with anthropogenic activities (Palmer et al. 2015). Therefore, increased attention is being devoted to carbon monitoring of optically shallow waters. Several studies have demonstrated that remote sensing technologies show great promise for monitoring freshwater DOC dynamics through bio-optical properties (Brezonik et al. 2015; Kutser et al. 2015; Olmanson et al. 2016; Zhu et al. 2015).

Colored dissolved organic matter (CDOM) is defined as the photoactive fraction of dissolved organic matters in water (Brando and Dekker 2003). Light absorption by

CDOM tends to be strongest at short wavelengths (ultraviolet to blue) while diminishing to near zero in the red wavelength region of the electromagnetic spectrum (Markager and Vincent 2000). So CDOM level is often represented by a CDOM absorption coefficient within the highly absorbed short wavelengths, and 440 nm is frequently used by the remote sensing community (Brando and Dekker 2003; Matsuoka et al. 2013; Menon et al. 2011; Watanabe et al. 2016). Many previous studies have confirmed that CDOM levels are highly correlated to DOC concentrations in coastal & inland waters influenced by river discharge, regulated by terrestrial sources and seasonal effect (Del Castillo et al. 1999; Del Vecchio and Blough 2004; Ferrari et al. 1996; Hestir et al. 2015; Kowalczuk et al. 2003). Therefore, CDOM is often used as a proxy to trace the spatial distribution of DOC so as to help quantify the transport of terrigenous organic carbon (Mannino et al. 2008). Thus, the quantitative estimation of CDOM absorption via remote sensing aids in the better understanding of carbon cycling at the land-water interface.

Most research efforts on the remote sensing of water biogeochemistry (CDOM, Chl-a and non-algal particles) have focused on the estimation of water bio-optical properties in open oceans (Lee 2006; Mobley 1999; Siegel et al. 2002). Generally, many of these remote sensing algorithms empirically utilize band ratios calibrated from regional datasets to retrieve water properties (Kutser et al. 2005; Matthews 2011). However, they are often site-specific and need intensive calibration when applied to a new environment. Semi-analytical algorithms made a significant improvement to location independence by extracting water biochemical properties based on bio-optical radiative transfer models. Representative algorithms include multi-band quasi-analytical algorithm (QAA) (Lee et al. 2002), Carder-MODIS (Carder et al. 2004), Garver-Siegel-Maritorena (GSM) (Maritorena et al. 2010; Maritorena et al. 2002), and Linear Matrix (LM) model (Hoge and Lyon 1996; Yang et al. 2011). Unfortunately, these algorithms cannot separate CDOM absorption from $a_{dg}(440)$, the combined absorption of CDOM and non-algal particles (NAP), due mainly to their similar absorption spectra. Recently, several studies endeavored to extend mainstream ocean color algorithms to derive CDOM absorption for coastal and open ocean waters (Budhiman et al. 2012; Cui et al. 2014; Matsuoka et al. 2013; Shanmugam 2011; Zhu and Yu 2013). However, when these relatively mature semi-analytical ocean color algorithms are directly applied to inland waters, the uncertainty of the resulting CDOM estimation is prohibitively high (Miller et al. 2007; Zhu et al. 2013b).

In general, there are two major challenges with the current semi-analytical algorithms used for CDOM retrieval of inland waters. First, the bottom effect of shallow freshwater introduces significant uncertainty on CDOM estimation. Ocean color algorithms are developed for optically deep waters, which assume the upwelling water leaving radiance is only the result of water column constituents and ignore bottom reflection (Stedmon et al. 2000). This assumption is not valid for optically shallow inland and coastal waters, and therefore greatly limits the usage of these algorithms for inland waters (Aitkenhead-Peterson et al. 2003b). Specifically, none of the aforementioned algorithms consider the contribution of bottom reflectance and therefore they are not capable of accounting for the high uncertainty introduced by bottom effects in optically shallow waters. Second, semi-analytical algorithms often incorporate empirical parameters into bio-optical models (water radiative transfer models). Such parameters are largely calibrated via ocean and offshore observations. Inland fresh waters are often much richer in water-borne constituents, (i.e., a higher concentration of CDOM, Chl-a and/or suspended sediment), so these algorithms are often not optimal for handling in-land water environments (Zhu and Yu 2013; Zhu et al. 2013b). Except for a few cases, the majority of published research on CDOM retrieval in optically shallow lake waters adopt empirical methods (Campbell et al. 2011; Kutser et al. 2005; Kutser et al. 2015; Odermatt et al. 2012; Olmanson et al. 2016).

Bottom effects have been considered in some aquatic remote sensing studies, including estimating water optical depth (Brando et al. 2009; Majozi et al. 2014; Maritorena et al. 1994; Zhao et al. 2013), retrieval of the diffuse attenuation coefficient (Barnes et al. 2014; Barnes et al. 2013; Dekker et al. 2011; Giardino et al. 2015; Volpe et al. 2011), and monitoring bottom sediments properties (Klonowski et al. 2007). All of these approaches include the contribution of bottom sediment reflectance to the total upwelling radiance, which inspired us to develop a CDOM retrieval algorithm for optically shallow waters that also incorporates bottom reflectance.

First, this chapter examines *in situ* spectral data and demonstrates the spectral variation in response to water depths. Second, we developed the shallow water bio-optical properties (SBOP) algorithm which incorporates the bottom contribution into a CDOM retrieval algorithm. Third, we investigated the effectiveness of a proposed bottom effect index (BEI) to quickly separate optically shallow and optically deep waters. Finally, an adaptive approach based on our BEI was presented to identify the most suitable algorithm according to varied levels of bottom effect (optically shallow or deep water algorithms) in an effort to reduce overall uncertainty. This study aims to improve the capability of remote sensing to monitor carbon transportation from terrestrial to aquatic ecosystems across broad spatial and temporal scenarios.

2.3 Method

2.3.1 Study sites

In this chapter, Saginaw Bay in Lake Huron was selected for sampling CDOM levels concurrently with *in situ* remote sensing measurements across a broad range of CDOM levels. The sampling locations encompassed the Saginaw River, Kawkawlin River and inner Saginaw Bay (Figure 2-1). The bathymetry ranged from 0.25 to 4 meters with a median value of 1.6 meters. Generally, the bottom is dominated by sand with intermittent patches of benthic algae (Cladophora) and other aquatic plants. Compared to that of pure sand, the sediments of the lake bottom are relatively dark due to this mixture of the sand and benthic plants. The two rivers mentioned above are of vastly different size and composition and their drainage basins are covered by different dominant vegetation. The Saginaw River is 36 km long with a watershed area of 22,260 km^2. The river has a mean annual discharge of 130 m^3/s (2010 to 2016). The dominant landcover type is agriculture, which accounts for approximately 52 % of the watershed. The Kawkawlin River flows into the Saginaw Bay approximately 1 km north of the Saginaw River mouth. Its length (28 km), discharge and drainage area (647 km^2) are at a significant lower magnitude than those of the Saginaw River. The Kawkawlin River watershed is dominated by deciduous forest (40.2%) with a relatively high percentage of wetland (7.9%).

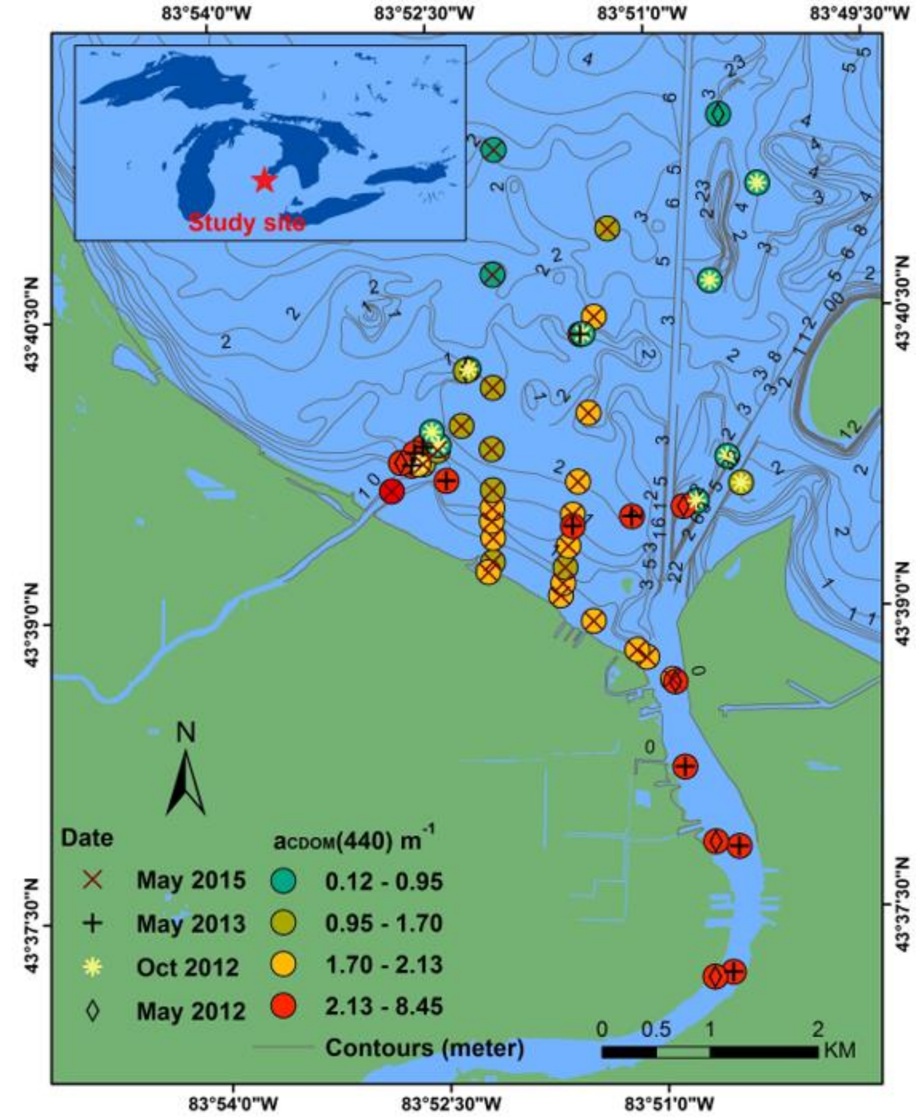

Figure 2-1: The 54 samples located in the Saginaw River, Kawkawlin River, Saginaw Bay, and Lake Huron. The four field cruises were conducted from May, 2012 to May 2015.

2.3.2 Field and laboratory measurements

A total of four cruises were carried out from 2012 to 2015. The cruises covered both spring and autumn seasons: May 7, 2015, May 7, 2013, May 10, 2012 and October 18, 2012. Field sampling design used a spatially stratified method to distribute the sampling locations at several water depth intervals within and near the river plumes; 54 samples were collected (Figure 2-1). The sample points were distributed along five transects and sample locations were slightly shifted due to the conditions present on each sampling date. The water depths of 27 sampling locations were measured by a Vexilar® Hand-held Depth Sonar during the cruise on May 7, 2015. The depths of the earlier sampling locations were generated from bathymetry contours downloaded from Michigan Geographic Data Library (MiGDL). These generated depths have been verified by the 2015 field depth measures with a mean error of less than 10%.

Surface water samples and *in situ* spectral data were collected in parallel at each sampling location. Water samples collected were stored in amber bottles (polypropylene 500ml) and kept chilled in a cooler until laboratory measurements of CDOM levels were performed. Samples at 5 locations were replicated for sampling uncertainty assessment (mean error < 3%). The *in situ* spectral data were collected at 2 meters above the water surface with a Satlantic® HyperSAS and HyperOCR sensors. The cruises were arranged during cloud free weather and under ~2 - 8 meter/sec wind speed so that wave effect is minimum. The HyperSAS instrument was deployed by following the operation instructions to ensure sensor view angles were adjusted according to the solar position during above-surface spectra data measurements (Figure 2-2). The *in situ* spectral data included sky radiance (L_s), total upwelling radiance (L_t) and downwelling irradiance (E_d) from 400 nm to 800 nm. The radiance sensor for measuring L_t was pointed to the water surface at an angle of 40° from nadir. The radiance sensor for measuring L_i was pointed skyward with an angle of 40° from solar zenith. Both sensors were set at the angle of 90° from solar azimuth angle. The E_d irradiance sensor was mounted separately and perpendicularly to the water surface. At least 20 radiance/irradiance measures were recorded at each location. The averages of these 20 spectral curves were used for all further analyses.

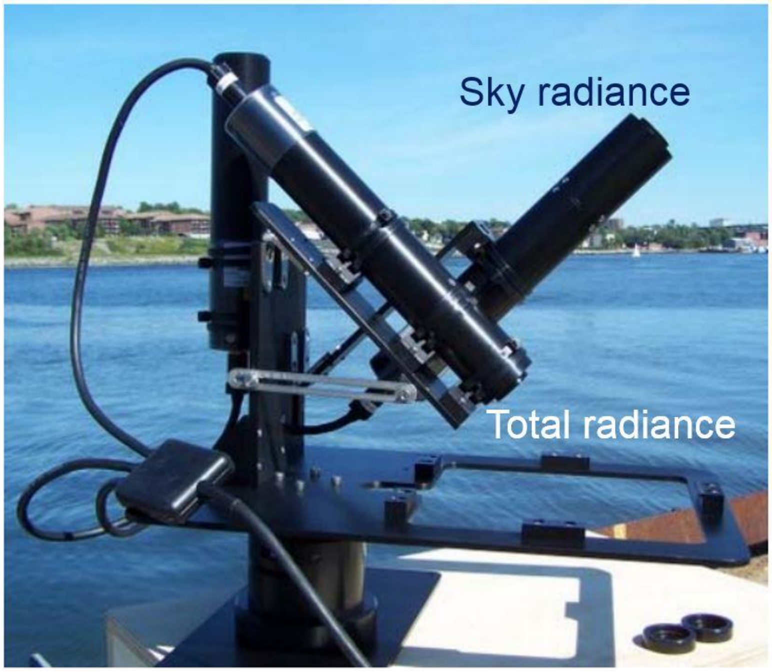

Figure 2-2: The HyperSAS instrument photo. This instrument was deployed to measure remote sensing reflectance of water.

In situ below-surface spectral data were measured to observe the water column light field. The below-surface upwelling irradiance was logged via a ASD® Fieldspec equipped with an under-water cosine corrected receptor. These below-surface spectra across 300 nm - 1000 nm were collected at 6 locations with varied depths (from ~0.6 m to ~4 m). These below-surface measurements were conducted vertically from just below the water surface to just above the bottom sediments at 0.3 meters interval. All spectral measurements were carried out between 10 A.M. and 2 P.M. in cloud free weather and wind conditions ranged from ~2 – 4 m/s (2 to 8 knots) that were associated with waves ranging from 0.15 to 0.45 meters according to the data from the National Weather Service. Other environment conditions did not vary significantly during the field measurements (depth, sediments, etc).

The CDOM measurements for all the collected water samples were completed within six hours of collection. The water samples were first filtered using glass microfiber filters GF/F (nominal 0.7 µm pore size) according to the standard laboratory measurement of CDOM (Mannino et al. 2008; Vodacek et al. 1997). Then the filtrate was transferred into 0.01 m cuvettes to measure CDOM absorbance $A(\lambda)$ via a Cary® 60 UV-Vis Spectrophotometer with Milli-Q water as blank. The CDOM absorption coefficient $a_g(\lambda)$ was calculated from Equation 1:

$$a_g(\lambda) = \frac{\ln(10)}{L} \times \ A(\lambda) \qquad (1)$$

where L is the diameter of cuvette in meters. All laboratory measurements were performed in triplicate and averaged in order to increase overall accuracy.

2.3.3 The shallow water bio-optical properties (SBOP) algorithm

In this chapter, A shallow water bio-optical properties algorithm (SBOP) was developed for CDOM absorption retrieval to reduce the uncertainty caused by bottom sediments (Li et al. 2017). In optically shallow waters, the water-leaving reflectance is made up of contributions from both waterbody and bottom sediments. So the below-surface remote sensing reflectance r_{rs} can be modeled as (Lee et al. 2007):

$$r_{rs} = r_{rs}^{c} + r_{rs}^{b} = r_{rs}^{dp}\left(1 - e^{-D_c(a_t+b_b)H}\right) + \frac{1}{\pi}\rho e^{-D_b(a_t+b_b)H} \tag{2}$$

where r_{rs}^{c} represents the water column contribution. r_{rs}^{b} represents the bottom sediments contribution. $D(a_t + b_b)$ represents the light attenuation caused by water column absorption and backscattering for water column light components (D_c) or light components from bottom (D_b). Finally, D_c and D_b are empirical factors associated with under-water photon path elongation due to scattering and can be calculated as below (Lee et al. 1999):

$$D_c = 1.03(1 + 2.4\frac{b_b}{a_t+b_b})^{0.5} \tag{3}$$

$$D_b = 1.05(1 + 5.5\frac{b_b}{a_t+b_b})^{0.5} \tag{4}$$

The value 1.05 and 5.5 used in the calculation were determined after repeated experiments and they were found to be the optimal. r_{rs}^{dp} represents below-surface remote sensing reflectance when the water is infinitely deep and can be modeled as (Lee et al. 2013):

$$r_{rs}^{dp} = \left(0.089 + 0.125\frac{b_b}{a_t+b_b}\right)\frac{b_b}{a_t+b_b} \tag{5}$$

Several previous studies as well as our model calibration results showed that using 0.089 and 0.125 for the calculation of r_{rs}^{dp}would improve model applicability to shallow waters (open waters, coastal waters, and inland waters) (Barnes et al. 2013; Lee et al. ; Lee et al. 2013; Yang et al. 2013; Zhu and Yu 2013). Then r_{rs} can be determined by the following bio-optical variables: bottom reflectance ρ, water depth H, absorption and backscattering coefficients a_t and b_b. For the SBOP algorithm, the total absorption coefficients (a_t) at a given wavelength (λ) is modeled from three components:

$$a_t(\lambda) = a_w(\lambda) + a_p(\lambda) + a_g(\lambda) \tag{6}$$

where $a_w(\lambda)$ is the pure water absorption coefficient, $a_g(\lambda)$ is the CDOM absorption coefficient, and $a_p(\lambda)$ represents the particle absorption coefficient, which include both phytoplankton and non-algal particles. The total backscattering coefficients $b_b(\lambda)$ is calculated via two components:

$$b_b(\lambda) = b_{bw}(\lambda) + b_{bp}(\lambda) \tag{7}$$

where $b_{bw}(\lambda)$ and $b_{bp}(\lambda)$ are backscattering coefficients of pure water and particles, respectively. The values of $a_w(\lambda)$ and $b_{bw}(\lambda)$ are known (Morel 1974; Pope and Fry 1997). The $b_{bp}(\lambda)$ and $a_g(\lambda)$ were modeled as follows (Lee et al. 2013):

$$b_{bp}(\lambda) = P\left(\frac{\lambda}{555}\right)^{y} \tag{8}$$

$$a_g(\lambda) = Me^{-S(\lambda-440)} \tag{9}$$

where *y* is the spectral parameter that determines the scattering decay and was estimated as (Lee et al. 2002):

$$y = 2(1 - 1.2e^{-0.9\frac{R_{rs}(444)}{R_{rs}(555)}}) \tag{10}$$

S is the parameter establishing the absorption decay slope (spectral slope) and its value is approximately 0.015 as derived from the global average value (Zhu et al. 2014). This value is more applicable to a broad range of water cases and reduces the bias in algorithm comparison. The unknown factor *M* is the CDOM absorption coefficient at 440 nm. *P* is the particle backscattering coefficient at 555 nm. There is a good positive correlation between $a_p(\lambda)$ and $b_{bp}(\lambda)$ as both are associated with suspended particulate matter (Babin et al. 2003b; Zhu et al. 2014). Ultimately, $a_p(\lambda)$ was modeled as:

$$a_p(\lambda) = qP\left(\frac{\lambda}{555}\right)^y \tag{11}$$

where *q* = 0.75 which represents the empirical ratio of a_p and b_{bp} (Zhu and Yu 2013; Zhu et al. 2013b). The bottom reflectance ($\rho(\lambda)$) at each wavelength is expressed as:

$$\rho(\lambda) = B\rho_{bottom}(\lambda) \tag{12}$$

where $\rho_{bottom}(\lambda)$ is the dominant bottom material spectrum (sand) and it is normalized by the reflectance at 555 nm (Figure 2-3). Then B is the bottom reflectance at 555 nm which is unknown.

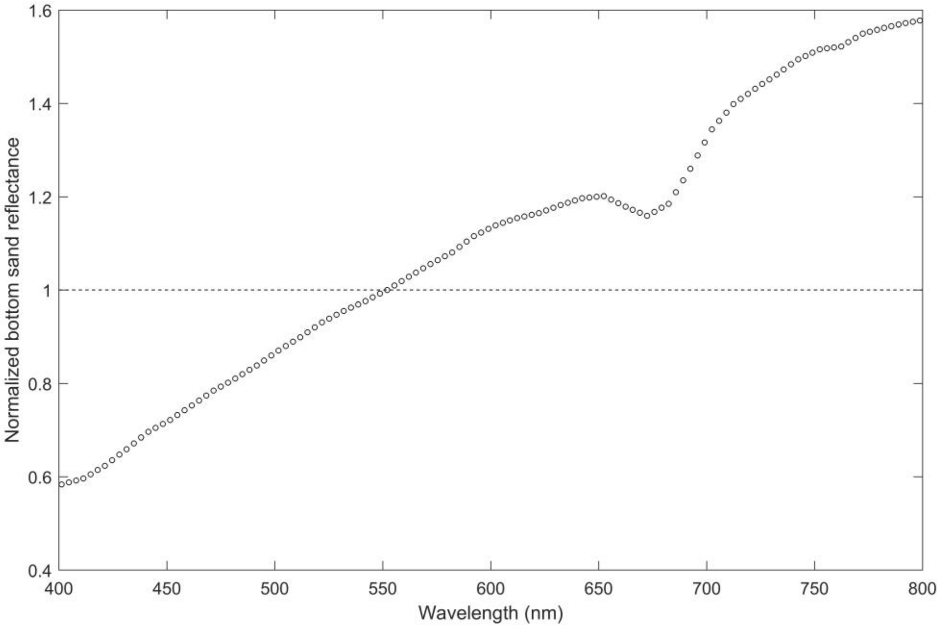

Figure 2-3: The normalized spectra curve of the bottom reflectance. Bottom reflectance at 550 nm was assessed to normalize the bottom spectrum curve.

All the empirical parameters selected in the SBOP algorithm were global average values. So, A sensitivity analysis was conducted in order to confirm that global values are suitable for the relevant parameters (Table 1). Overall, using alternative settings has a negligible effect on the results compared to general setting. The general setting is preferable as algorithm validation is dependent less upon the study site.

Table 2-1: The sensitivity analysis for the parameter settings

Parameters	General setting	Alternative setting	Accuracy change
$D_b = 1.05(1 + 5.5\frac{b_b}{a_t + b_b})^{0.5}$	1.05, 5.5 New version HOPE	1.04, 5.4 Old version HOPE	+ 0.5%
$r_{rs}^{dp} = \left(0.089 + 0.125\frac{b_b}{a_t + b_b}\right)\frac{b_b}{a_t + b_b}$	0.089, 0.125 General water	0.084, 0.17 High scattering water	+ 2.5%
Spectral slope *S*	0.015 Global mean	0.0152 Field data-based	- 0.5%

Through equations (2)-(12), r_{rs} is constructed to describe optically shallow waters' bio-optical properties and contains four unknown variables *B*, *M*, *P* and *H*:

$$r_{rs}(\lambda) = f(B, M, P, H)\ (\lambda) \tag{13}$$

The SBOP algorithm solves for these four unknown variables via spectral optimization. In the SBOP processing, the initial values of the B, M, P and H were set as following (Lee et al. 2013):

$$B = 0.1 \tag{14}$$

$$M = 0.075\left(\frac{R_{rs}(444)}{R_{rs}(555)}\right)^{-1.7} \tag{15}$$

$$P = 0.025\left(\frac{R_{rs}(444)}{R_{rs}(555)}\right)^{-1.7} \tag{16}$$

$$H = 1.5 \tag{17}$$

B, bottom reflectance at 555nm, was set as 0.1. H, the average depth was set as 1.5 meters according to study site conditions. After tests these initial values were found to be the best. Our optimization process minimizes the differences between modeled below-surface reflectance $\widehat{r_{rs}}$ and measured below-surface reflectance $r_{rs}(\lambda)$ (obtained from *in situ* spectral measurements or remote sensing images), ultimately determining each variable in order to derive CDOM absorption and bottom contribution. Specifically, the optimization aims to find these four variables that minimize the following error function:

$$err = \frac{\sqrt{\sum_{i=1}^{N}(r_{rs}(\lambda_i) - \widehat{r_{rs}}(\lambda_i))^2}}{\sqrt{\sum_{i=1}^{N} r_{rs}(\lambda_i)}} \tag{18}$$

The nonlinear system solver function in Matlab was applied in this study, which used the trust region dogleg algorithm to process the optimization (Powell 1968). The SBOP algorithm requires a minimum of four r_{rs} values at different wavelengths as input. So potentially it can be applied to both multispectral and hyperspectral data. In this study, the hyperspectral data (120 r_{rs} bands) was applied to estimate the CDOM absorption. The algorithm performance was evaluated by comparing remote sensing derived CDOM results with laboratory measurements of CDOM using field water samples. The following five statistical metrics were assessed: *bias*, mean normalized bias (MNB), absolute mean error (AME), root mean squared error (RMSE, log space) and R^2 (regression, Type II).

The validation of the algorithm performances was performed based on the following statistical metrics:

The *Bias*:

$$bias = \frac{\sum_{i=1}^{n}(a_i^{est} - a_i^{obs})}{n} \tag{19}$$

The MNB:

$$MNB = \frac{\sum_{i=1}^{n}\left(\frac{a_i^{est} - a_i^{obs}}{a_i^{obs}}\right)}{n} \tag{20}$$

The AME is:

$$AME = \frac{\sum_{i=1}^{n}\left(\left|\frac{a_i^{est} - a_i^{obs}}{a_i^{obs}}\right|\right)}{n} \tag{21}$$

The RMSE is:

$$RMSE = \sqrt{\frac{\sum_{i=1}^{n}\left[\log(a_i^{est}) - \log(a_i^{obs})\right]^2}{n-2}} \tag{22}$$

where a_i^{est} is remote sensing derived results and a_i^{obs} is laboratory measured results of CDOM absorptions.

2.3.4 Adaptive approach for computation efficiency

In estimating CDOM in inland and coastal waters, a single scene of satellite data often contains a broad range of water depths (e.g. Landsat 8). The estimation of CDOM through the SBOP algorithm is generally both time and computation intensive, for the relatively complex equations illustrated above need to be solved through optimization. One way to improve optimization efficiency is to separate the water spectral data into high or low bottom effect groups and only apply SBOP to the high bottom effect (optically-shallow) group. We introduce an adaptive approach of applying the SBOP algorithm only to optically shallow waters and applying the deep water semi-analytical algorithm (QAA-CDOM) to optically deep waters.

The QAA-CDOM is a representative semi-analytical algorithm for CDOM retrieval in deep waters (Zhu et al. 2014). This algorithm can be efficiently applied to a wide range of water conditions, including estuarine and coastal waters assuming the water is optically deep. It calculates CDOM absorption directly from R_{rs} in 13 steps. The first ten steps derive the total absorption coefficient $a_t(440)$ and $b_{bp}(555)$ (Lee et al. 2002; Zhu et al. 2013a). Then last three steps derive the absorption of particulates $a_p(440)$ from $b_{bp}(555)$ in order to calculate $a_g(440)$ by the following equations:

$$a_p(\lambda) = J_1 b_{bp}(555)^{J_2} \tag{23}$$

$$a_g(440) = a_t(440) - a_w(440) - a_p(440) \tag{24}$$

where $J_1 = 0.63$ and $J_2 = 0.88$ are two parameters that were estimated from *in situ* data from inland waters (Zhu and Yu 2013). The required inputs of the QAA-CDOM algorithm are R_{rs} at wavelengths of 440, 490, 555 and 640 nm.

Water depth is a key factor determining the bottom effect and is often used to separate optically deep or optically shallow waters. However, the bottom effect is also highly influenced by water column attenuation (Barnes et al. 2014; Zhao et al. 2013). A tangible example is that bottom reflectance could contribute significantly to water-leaving radiance for deep but clear/transparent water with a highly reflective bottom such as sand. Therefore, the bottom effect index (BEI) was introduced which considers both the bathymetry and water column attenuation to quickly identify waters for which bottom reflectance is significant. It is defined as an exponential function because it has been established that underwater light is exponentially attenuated with water depth (Markager and Vincent 2000):

$$BEI = e^{-\left(\frac{R_{rs}(\lambda_1)}{R_{rs}(\lambda_2)}\right)H} \tag{25}$$

where H is the water depth. The R_{rs} band ratio (e.g. 690/555 nm) represents light attenuation by the water column and was often used as a proxy for water turbidity in previous research (Dall'Olmo et al. 2005; Dogliotti et al. 2015; Doxaran et al. 2005; Doxaran et al. 2002). The ratio 690/555 nm was applied in this study.

The adaptive approach applies either the SBOP or QAA-CDOM algorithm for individual location/spectra depending on the significance of bottom effect (Figure 2-4).

Initially, the field spectral data is subjected to the BEI in order to determine whether the waters are categorized as optically shallow or optically deep waters. Then, the optically shallow waters are processed via SBOP while the optically deep waters are processed by QAA-CDOM to estimate the CDOM absorption. This adaptive approach aims to improve the computation efficiency for the regions with known bathymetry data (e.g. the Great Lakes regions), which are largely available for near-coastal shallow waters. Alternatively, for multi-temporal CDOM monitoring, the bathymetry of the site can be derived from SBOP algorithm once, and then be applied for other seasons when using the adaptive approach.

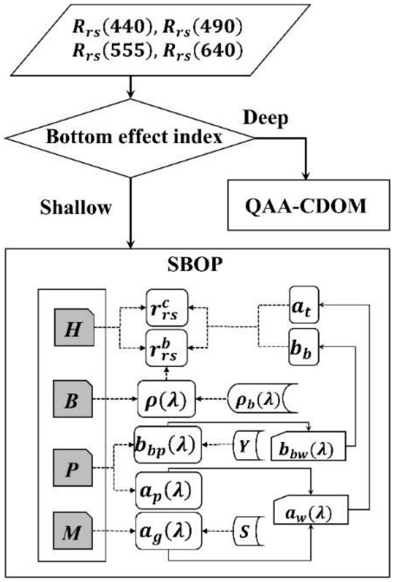

Figure 2-4: Conceptual flowchart of adaptive approach and SBOP algorithm. In the SBOP algorithm, the H, B, P, and M were four unknown factors which were derived from optimization. The depth H affected the water column reflectance and bottom reflectance. The bottom reflectance B contributed to the below-surface remote sensing reflectance $\mathrm{r_{rs}}$. The CDOM absorption M and the particle backscattering P determined the light attenuation.

2.4 Results and Discussions

2.4.1 Spatial and seasonal dynamics of the CDOM field sampling results

Field water samples showed that CDOM levels exhibit a distinct spatial trend, descending from the near-shore lower river channel and river plume regions to the inner bay. The sampled CDOM absorption $a_g(440)$ widely ranged from 0.12 m^{-1} - 8.46 m^{-1} (Figure 2-1). CDOM levels at the river sample locations were generally high, with the Saginaw River having a value as high as 8.45 m^{-1}. The average of CDOM levels around the plume area of the Kawkawlin River (5.38 m^{-1}) is much higher than that of the Saginaw River (1.73 m^{-1}). This marked difference was attributed to the terrestrial ecology of the drainage watersheds. The large proportion of both deciduous forest and associated litter and wetland areas within the Kawkawlin River watershed likely caused the higher CDOM levels in its plume area. The field sampling generally captured the complex spatial variation of CDOM in this area and provided a good foundation for evaluating these remote sensing algorithms.

Distinct seasonal variations of freshwater CDOM between May and October were also observed, likely driven by the organic carbon supply in the drainage watersheds and hydrological processes (Tian et al. 2013). The mean CDOM absorption of samples collected in May was 2.75 m^{-1}, much higher than that in October (mean value of 0.54 m^{-1}). The higher CDOM levels during the spring season are analogous to trends reported in a recent study, which reported that the surface and subsurface hydrology associated with snow melt is responsible for transporting organic matters from soil organic carbon pools into the river systems (Tian et al. 2013). Similarly, the Saginaw

River watershed is dominated by the agricultural land use which has increased metabolic activities on crop residues in the spring (Spedding et al. 2004). The second most dominant land cover in the Saginaw River watershed is deciduous forest. The large proportion of soil carbon originates from the biological decay of both crop litters and forest leaf litters, so the soil carbon levels are much higher in spring when the large accumulation of carbon is flushed out of the soil through snowmelt. Meanwhile, the consumption of organic matters throughout the growing season leads to relatively lower soil carbon levels in October (Kalbitz et al. 2000a).

These seasonal hydrological processes also explain inter-annual CDOM variability (Berto et al. 2010; Raymond and Oh 2007). The sampled CDOM level in May 2015 was clearly lower (mean 2.05 m^{-1}) than that in 2013 (mean 3.51 m^{-1}) and 2012 (mean 3.70 m^{-1}). The winter of 2014-15 had relatively large snowfall accumulations and peak snowmelt occurred in April, much earlier than in 2012 and 2013 (Figure 2-5). The available soil organic matter in the watersheds was largely depleted during this early spring thaw in mid-April 2015, which likely resulted in the observed lower CDOM levels during the May 2015 sampling campaign. Contrarily, the relatively higher CDOM levels sampled in May 2012 and 2013 were associated with the receding leg of a more normal spring discharge event.

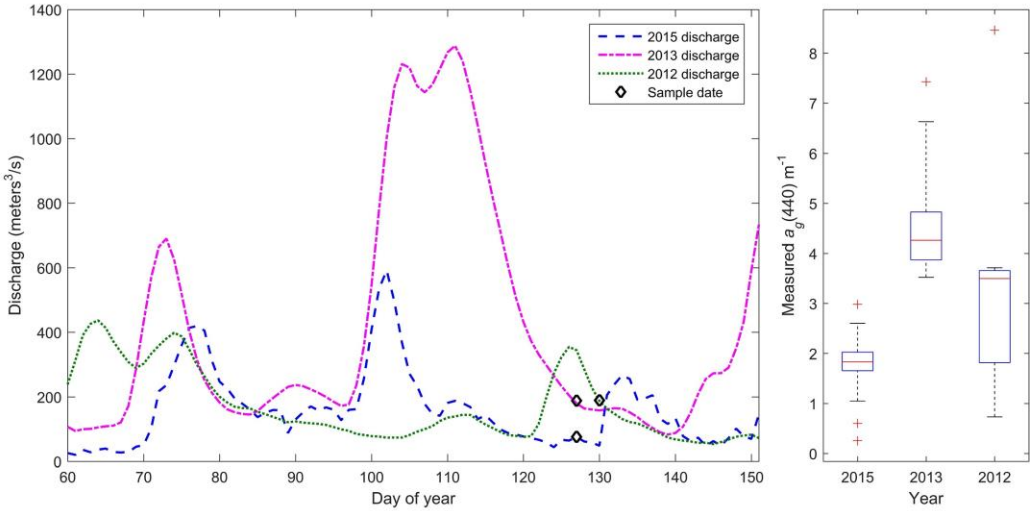

Figure 2-5: River discharge of the Saginaw River from USGS streamflow data (the left) and sampled CDOM absorption in boxplot (the right). The boxplot draws the 75th, the median and the 25th percentiles of the CDOM absorption. The snowmelt started in March 2015. Spring flood depleted much of the terrestrial organic carbon before the sample date in May 2015, so the CDOM level in May 2015 is lower than that in May 2013 and May 2012.

Above-surface R_{rs} measured by the HyperSAS spectrometer demonstrated the potential of using remote sensing for the estimation of CDOM levels and other bio-optical properties of water. Figure 2-6 illustrates how R_{rs} measured via HyperSAS is spectrally contaminated by strong bottom reflectance. The 27 samples on turbidity measurements (Secchi disk depth) were collected in May 2015 and were accompanied with comparable measurements of CDOM levels. All the spectra data in Figure 2-6 were under the same general water turbidity conditions. The light attenuations by the water column were generally the same in these sites, but did differ with depth. The shallow water samples (0.6 m < Depth < 0.9 m) show reflectance (R_{rs}) twice as high as that of the deep water samples (2.7 m < Depth < 3.7 m), which is attributed to the bottom sediments reflectance. Therefore, neglecting bottom reflectance could introduce significant uncertainties in CDOM retrieval for optically shallow waters. Higher bottom effect will lead directly to higher water-leaving radiance. Consequently, the prevailing deep waters CDOM retrieval algorithms would significantly overestimate CDOM levels (Zhu et al. 2013b). Therefore, our *in situ* spectra observations strongly suggest that bottom reflectance must be considered when applying CDOM retrieval algorithms for optically shallow waters.

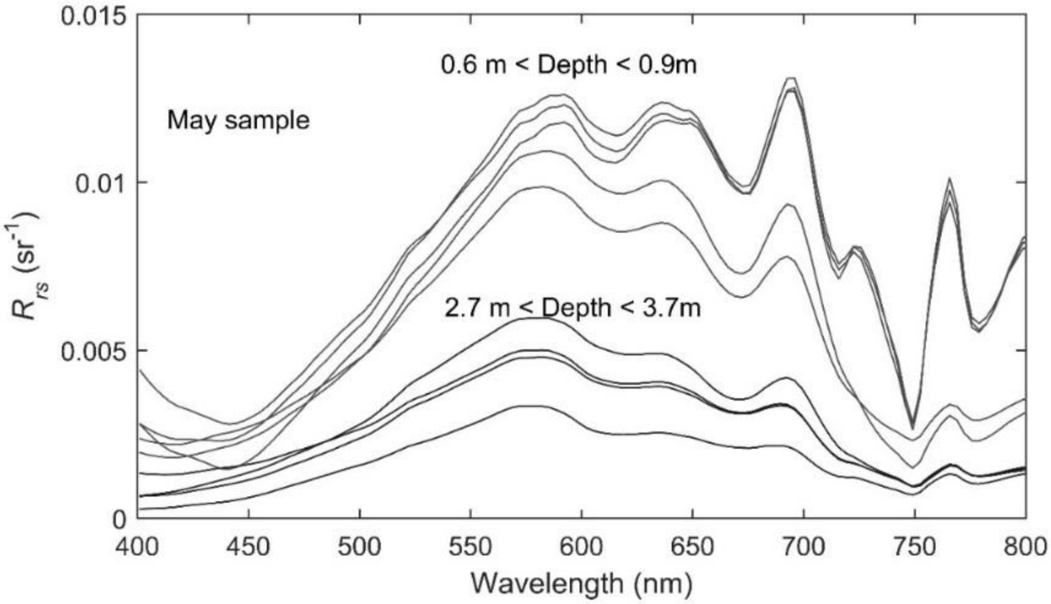

Figure 2-6: The measured remote sensing reflectance at shallow (0.6 m < depth < 0.9 m) and deep (2.7 m < depth < 3.7 m) waters with similar CDOM absorption ($1.8^{-1} < a_g(440) < 2.3$ m^{-1}) and turbidity in May 2015.

2.4.2 Algorithm performance and validation of SBOP

We validated SBOP with laboratory measured CDOM from field water samples and assessed the algorithm performance in comparison to QAA-CDOM (Table 2-2). The SBOP algorithm performed better than QAA-CDOM with respect to all five error metrics. In particular, QAA-CDOM resulted in a much higher bias (1.61). In the shallow waters, the high bottom reflectance significantly increases the reference at longer wavelengths, which leads to the high spectral slope of remote sensing reflectance (440 nm to 600 nm). Consequently, CDOM is overestimated in deep water algorithm QAA-CDOM. In contrast, the SBOP (bias = 0.07) successfully modeled both the bottom and water column components of R_{rs} and greatly reduced the error and bias. Since over half of the sample sites were located in optically shallow waters, the performance of the QAA-CDOM algorithm was indeed affected by the intrusive bottom reflectance, whereas the SBOP algorithm successfully reduced uncertainty on CDOM retrieval for optically shallow waters. The SBOP algorithm dramatically improves the accuracy of CDOM estimation in optically shallow freshwater environments.

Table 2-2: Performance comparisons of SBOP and QAA-CDOM. SBOP algorithm showed better performance in the study sites which contains more than half of the shallow water sites.

Method	RMSE	bias	MNB	AME	R^2
QAA-CDOM	0.31	1.61	0.85	0.93	0.48
SBOP	0.22	0.07	0.34	0.54	0.74

The remote sensing derived $a_g(440)$ vs. ground truth $a_g(440)$ for individual samples is shown in Figure 2-7. The overall R^2 of SBOP (R^2 = 0.74) significantly outperformed QAA-CDOM (R^2 = 0.48). The SBOP performs significantly better by taking into consideration the bottom reflectance in the shallow water regions (labeled as Group A and Group B). Furthermore, the error range resulting from the QAA-CDOM algorithm was also larger and some samples have estimated CDOM (between ~10 m^{-1} and ~14 m^{-1}) two or three times larger than the measured values. These overestimations were from samples located at the most shallow and clearer locations (less than 1 meter) in the Saginaw River and near shore regions where ground-truthed CDOM levels were relatively low (labeled as group A). These results further confirmed that neglecting bottom reflectance does indeed result in much higher algorithm uncertainty. Comparatively, the QAA-CDOM algorithm produced more accurate CDOM estimation for samples in shallow waters that had relatively high CDOM levels (between ~4 m^{-1} and ~8 m^{-1}) (labeled as group B). This scenario occurred in the Kawkawlin River plume regions where water color was stained brown resulting from its watershed being dominated by deciduous forest (leaf litters) and wetland. In essence, high CDOM levels and associated strong water column absorption reduced the overall negative influence of the bottom effect. CDOM levels of deep water samples labeled as group C were slightly underestimated by the SBOP algorithm. This is caused by the over-estimation of bottom reflectance for deep water samples, as the trend line deviated from the 45 degree 1:1 line. However, the performance of both algorithms degraded when the CDOM level is very low. Specifically, low CDOM samples collected in May 2015 have relatively larger errors.

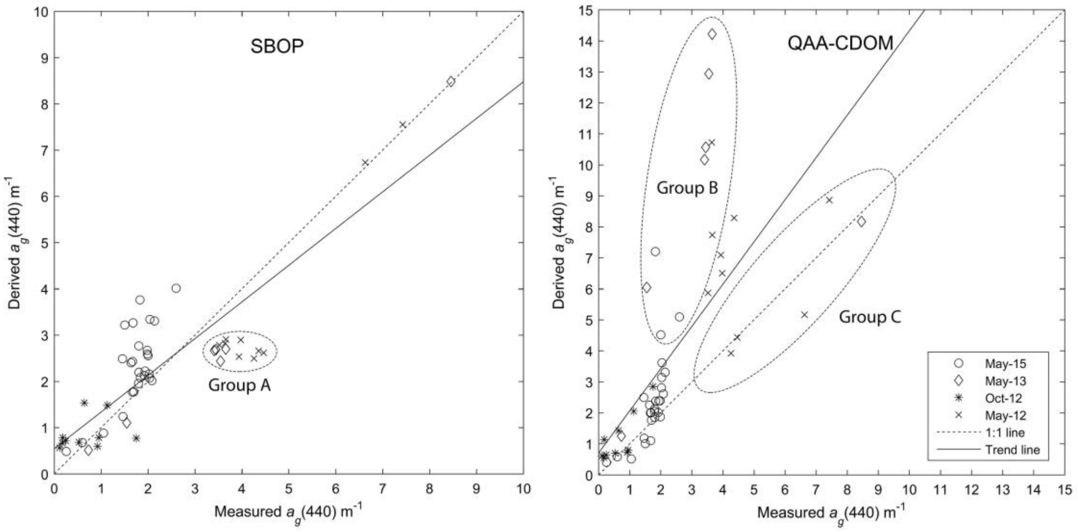

Figure 2-7: The measured vs. derived a_g(440) from SBOP (the left) and QAA-CDOM (the right) algorithm. Group A represents the shallow water samples (<1 m) with low CDOM levels (between ~1.8 m^{-1} to ~3.5 m^{-1}). Group B represents the shallow water samples (< 1 meter) with high CDOM levels (between ~4 m^{-1} and ~8 m^{-1}). Group C is the deep water samples (> 1.5 m).

2.4.3 Shallow water bottom effect on the SBOP algorithm estimation

The ASD measured spectra within the water column at six selected locations were assessed to study the relative role of bottom effect and to examine the SBOP algorithm's overall effectiveness. Figure 2-8 is an example of the differences in the remote sensing reflectance at three levels of water depths: just below water surface, just above bottom, and at mid depth measured with ASD Fieldspec. Remote sensing reflectance decreases with measurement depth due to absorption and scattering in the optical transmission processes.

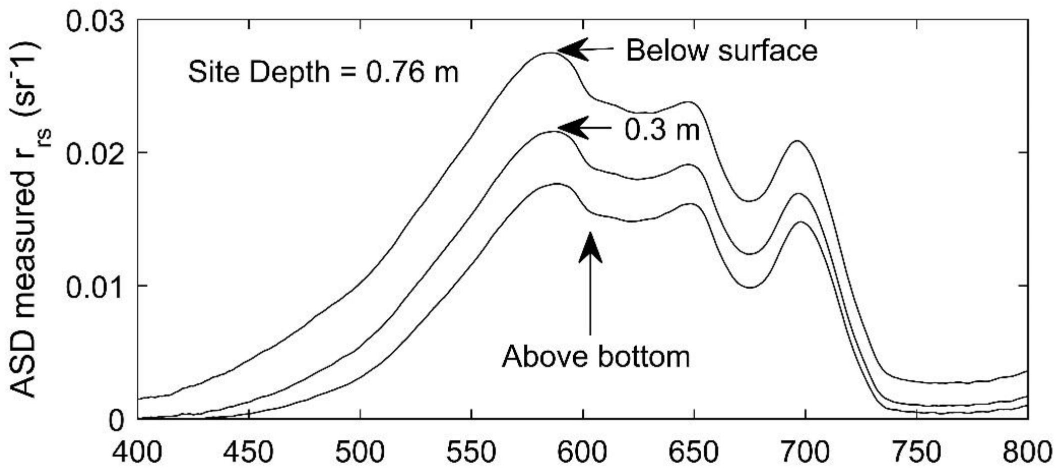

Figure 2-8: The below surface remote sensing reflectance was measured by the ASD Fieldspec from just below the water surface to just above the bottom. The plot showed the spectral results on shallow (0.76 m) site.

We choose two measured variables, just below surface reflectance (r_{rs}) and just above bottom sediments reflectance (ρ) at 555 nm to be compared to their estimated values by SBOP. Figure 2-9 compared these ASD measured values and the SBOP estimated r_{rs} and ρ. The R^2 value was 0.89 for $r_{rs}(555)$ and 0.79 for ρ (555). These relatively high correlations demonstrate that SBOP reasonably modeled water optical properties with a bottom reflectance effect. This deviation is understandable since r_{rs} and B were solved via optimization with 54 total samples/locations. The relative error of SBOP modeled $r_{rs}(555)$ and $B(555)$ were displayed for different depths (Figure 2-9 c). The algorithm generally performs well at shallow to moderate depths (~1 meter to ~2.5 meters). In these regions the bottom contributions account for a relatively lower percentage of total water leaving reflectance (~ 15%) when compared to the extremely shallow water sites (~30%). The large percentage of the bottom contribution in extremely shallow waters (< 1 m) does indeed lead to relatively high errors. Overall, the errors are smaller in optically shallow waters than optically deep waters. The implication might be that the set of parameters (determined by optimization) describe the light field of the well-mixed water columns in these near-shore waters better, but introduces increasing errors as water depth increases lead to absorption and scattering.

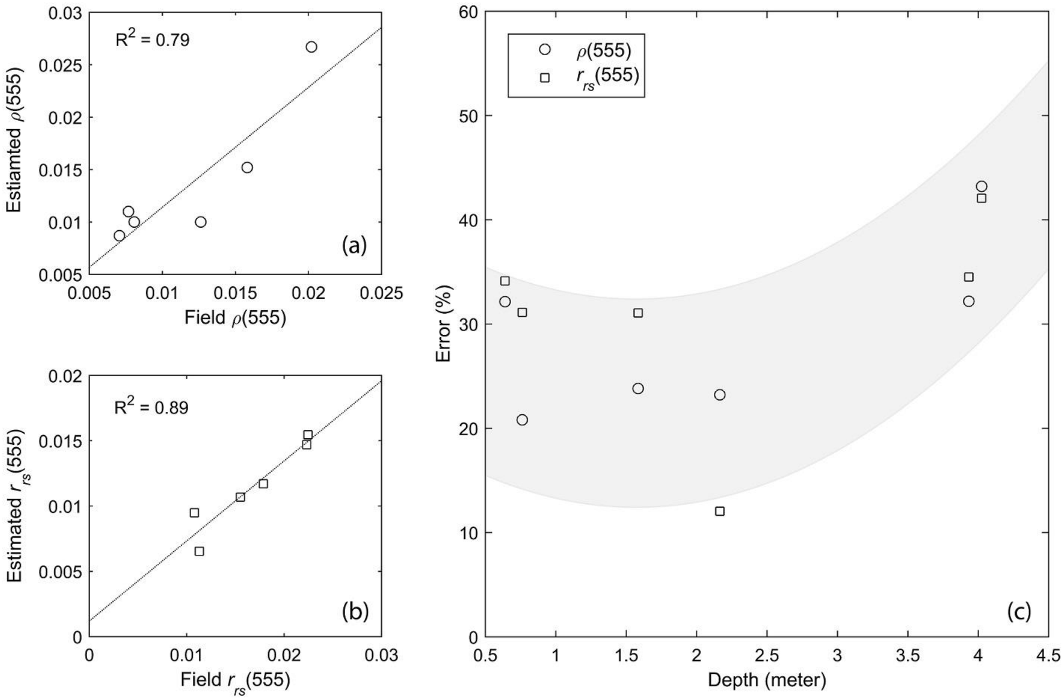

Figure 2-9: Comparisons of ASD measured reflectance and SBOP modeled just above the bottom (a) and just below the surface (b) reflectance. The relative errors of below surface remote sensing reflectance and bottom reflectance at 555nm were assessed at six different locations (c). The shaded area indicates the error trend of the SBOP. The shaded area indicates the error range of the SBOP. The maximum of the error was calculated to be the shade area boundary.

We plotted percent error with regard to depth or bottom effect index (BEI) at individual sampling sites, to investigate the influence of bottom effect on algorithm performance of the optically shallow water algorithm (SBOP) and the optically deep water semi-analytical algorithm (QAA-CDOM) (Figure 2-10). Such comparisons help to determine the threshold for the optically deep and optically shallow waters at our study site. At a depth < 1.5 meters, the SBOP generated a reasonably small error (MNB = 0.09, R^2 = 0.67) while the QAA-CDOM algorithm significantly over-estimates CDOM levels. The MNB (1.20) and R^2 (0.24) indicated that the QAA-CDOM caused very large uncertainty in such shallow waters (Table 3, Figure 2-11). Similarly, in waters with high bottom effect (BEI >= 0.2), the SBOP (RMSE = 0.16, R^2 = 0.75) generates more reasonable results compared to the QAA-CDOM (RMSE = 0.32, R^2 = 0.30). Conversely, in the waters with negligible bottom effect (BEI < 0.2) the QAA-CDOM results in a slightly lower RMSE and higher R^2 than SBOP (QAA-CDOM: RMSE = 0.26, R^2 = 0.81; SBOP: RMSE = 0.27, R^2 = 0.47). CDOM levels were under-estimated by SBOP compared to the QAA-CDOM where the bottom effect was low (Figure 2-11). As water depth increases, the light is strongly attenuated by the water column and its constituents in both the downward and upward paths. Theoretically, at a certain depth, bottom reflectance contributed no light to the total water leaving radiance (Dogliotti et al. 2015). However, the SBOP output does indicate a minimal bottom contribution to the total water leaving radiance at these relatively high depths, which inherently over-emphasizes the bottom contribution and consequently underestimates the water column contribution. The constraints of B was set to the range of $0.01 \leq B \leq 0.9$. After the optimization, the minimal B was approximately 0.05 for the optically deep waters. The SBOP algorithm does not produce a B constraint for the non-bottom effect waters. This might explain why SBOP outputs slightly under-estimation for the optically deep waters. This limitation of the SBOP algorithm creates the need to choose the more suited CDOM retrieval algorithm (QAA-CDOM and SBOP) for waters with low bottom effect or high bottom effect respectively.

Table 2-3: Validations of QAA-CDOM and SBOP for optically shallow and deep groups when applying Depth or BEI threshold for separation.

Method	RMSE	bias	MNB	AME	R^2	Optically Depth
QAA-CDOM	0.26	0.25	0.59	0.72	0.80	*Depth > 1.5 m*
SBOP	0.26	0.14	0.51	0.67	0.72	*Depth > 1.5 m*
QAA-CDOM	0.35	3.52	1.19	1.20	0.24	*Depth <= 1.5 m*
SBOP	0.16	-0.03	0.09	0.36	0.67	*Depth <= 1.5 m*
QAA-CDOM	0.26	0.26	0.61	0.70	0.81	*BEI < 0.2*
SBOP	0.27	0.12	0.52	0.68	0.47	*BEI < 0.2*
QAA-CDOM	0.32	2.93	0.98	1.05	0.30	*BEI >= 0.2*
SBOP	0.16	0.03	0.15	0.38	0.75	*BEI >= 0.2*

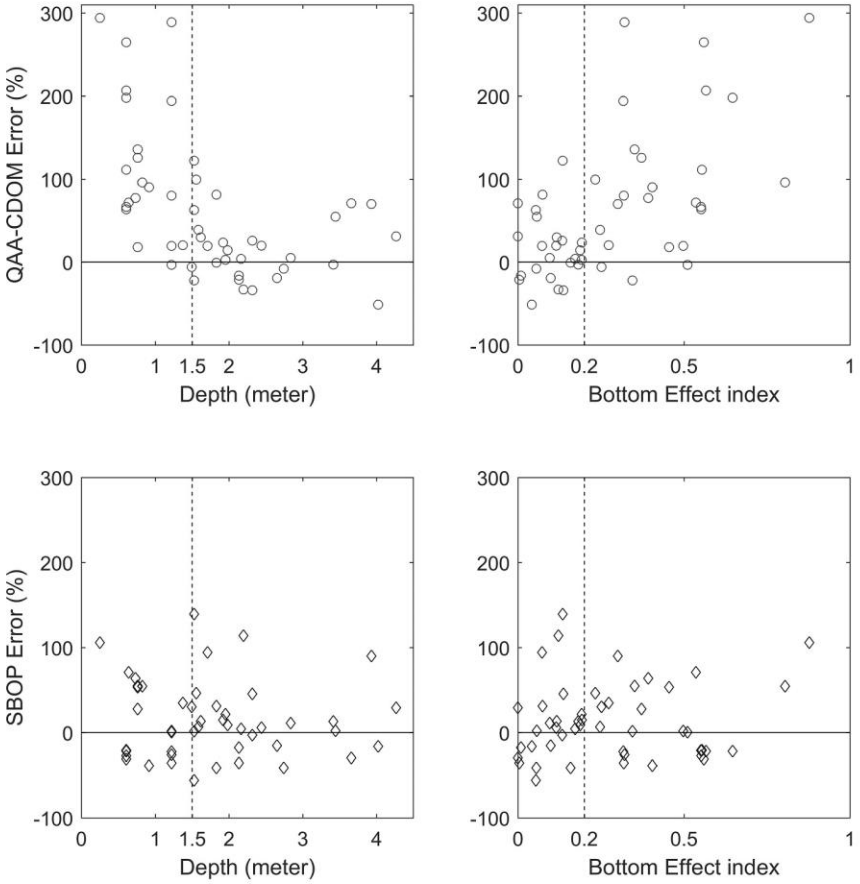

Figure 2-10: The percent errors of CDOM estimation from QAA-CDOM and SBOP methods related to depth and bottom effect index. When depth < 1.5m or BEI > 0.2, the QAA-CDOM outputs high error results.

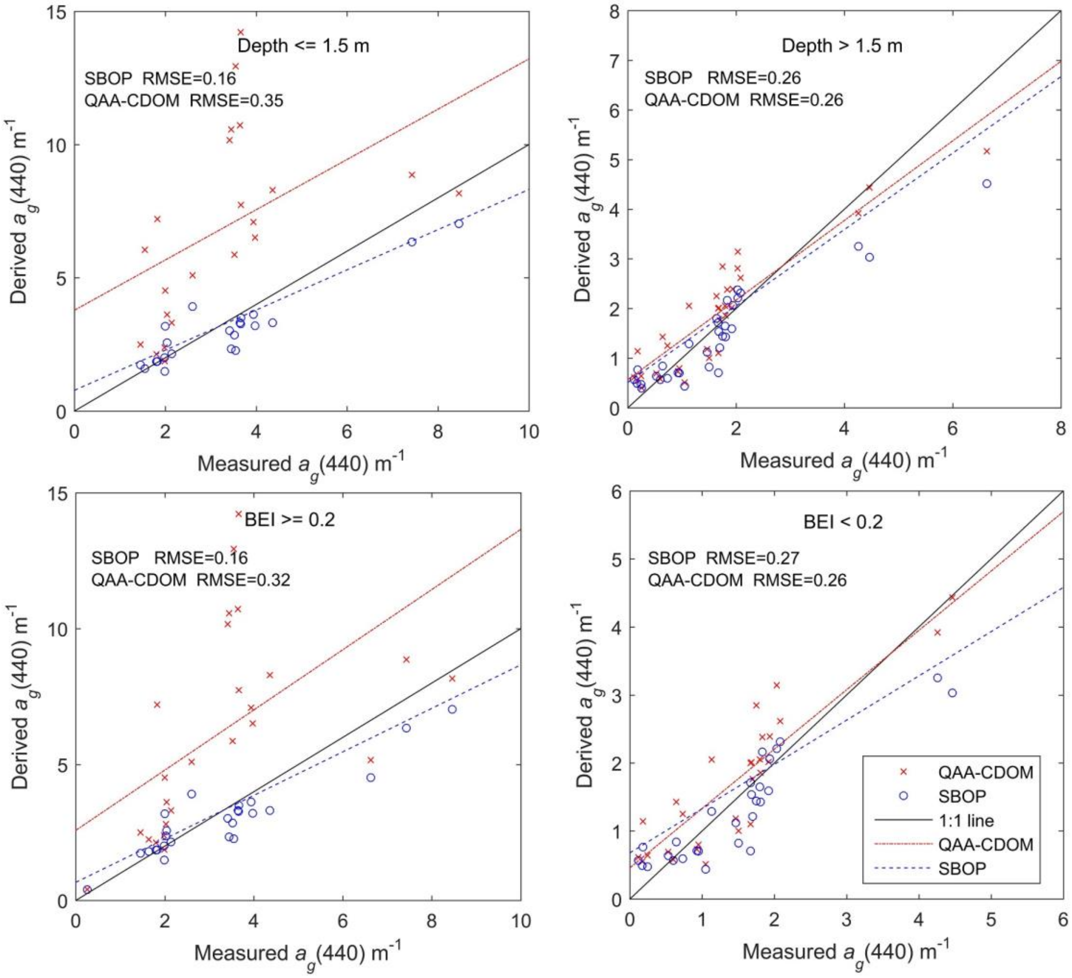

Figure 2-11: Derived vs. measured $a_g(440)$ for optically shallow and deep groups when separated by the depth or BEI threshold. SBOP significantly outperforms QAA-CDOM in optically shallow waters (depth <= 1.5 m or BEI >= 0.2), while it slightly under-estimates for optically deep waters (depth > 1.5m or BEI < 0.2).

2.4.4 Bottom effect adaptive approach

Adaptive approach improves the CDOM retrieval accuracy and saves computation time by applying the most suitable algorithm according to the amount of bottom effect (i.e., SBOP for optically shallow waters and QAA-CDOM for optically-deep waters). It overcomes the limits of each individual algorithm and considers bottom contribution only when necessary. We examined both water depth and BEI as a metric used to classify optically deep vs. optically shallow waters. The thresholds were set as optically deep waters (depth <= 1.5 m or BEI >= 0.2) and optically shallow waters (depth > 0.5 or BEI < 0.2). The threshold values were assessed through the comparisons of the algorithm performances. The BEI = 0.2 and depth = 1.5 m was generated through the performances of SBOP and QAA-CDOM algorithms (Figure 2-10). These two threshold values also provide the most separation in accuracy for the adaptive approach (optically deep waters used QAA-CDOM & optically shallow waters used SBOP). We tested multiple values to get these threshold values. The estimation results from the adaptive method are validated in Figure 2-12 and Table 2-4. The BEI and depth adaptive methodologies can both utilize the advantages of the QAA-CDOM and SBOP algorithms to output reliable results (Table 2-2 and 2-4). The performance evaluation shows that the BEI adaptive method (RMSE = 0.22 and $R^2 = 0.81$) has the advantage over the depth adaptive method (RMSE = 0.23 and $R^2 = 0.78$) (Table 2-4). The trend line of the BEI method is closer to the 45 degree 1:1 line at relatively high CDOM levels, indicating BEI introduces less bias for these high CDOM samples (Figure 2-12). Due to the relatively lower number of samples with deep clear waters and high bottom effect, the performance of the BEI adaptive approach is not markedly better than the depth adaptive method. When one considers both the computation efficient and accuracy, the adaptive approach is the suggested scheme to derive CDOM levels for inland freshwater and shallow coastal waters.

Table 2-4: Validations of Depth and BEI adaptive methods for $a_g(440)$ retrieval.

Method	RMSE	bias	MNB	AME	R^2
Depth Adaptive	0.23	0.14	0.39	0.57	0.78
BEI Adaptive	0.22	0.15	0.39	0.55	0.81

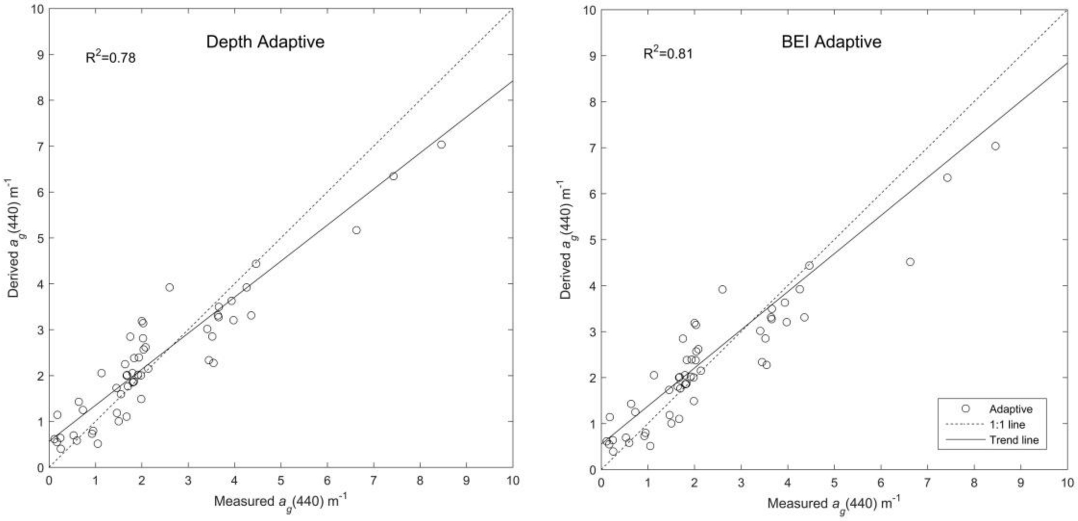

Figure 2-12: Derived vs. measured $a_g(440)$ from Depth (the left) and BEI (the right) adaptive methods. The trend line resulted from BEI adaptive approach is closer to the 1:1 line and indicates a better overall performance.

Our newly proposed BEI quickly separates optically shallow vs. optically deep waters based on both water depth and light attenuation (approximated by a band ratio) prior to the implementation of the adaptive method. In order to compare how well the two metrics, water depth and BEI, represent bottom effect, each was independently plotted relative to bottom contribution in Figure 2-13a and 2-13b, respectively. Note that for this investigation, bottom contribution (BC) for each sample was calculated as the ratio of bottom reflectance (B) and below-surface reflectance (r_{rs}). In Figure 2-13a and 2-13b, the shaded region represents a bottom contribution of < 20%, which referenced very turbid waters having low light penetration and negligible bottom effect. Bottom contribution greater than 20% represents optically shallow waters, which theoretically not only include shallow water, but also some relatively deep clear water samples. Depth ranging from 0 to 4 meters represents a gradient from optically shallow to optically deep waters. In contrast, a BEI index ranging from 1 to 0 represents a gradient from optically shallow to optically deep waters.

The depth metric cannot properly classify these clear deep or optically shallow waters (dashed circle in Figure 2-13a). These samples lead to the high uncertainties in the depth adaptive approach since they were processed by QAA-CDOM without considering bottom reflectance. In contrast, BEI takes into account both water depth and column attenuation. The deep clear water samples circled in Figure 2-13a (e.g. 4.2 meters with the bottom contribution of 40 %) were properly distinguished as high bottom contamination samples (with BEI > 0.2) in Figure 2-13b. For the "deep clear water", the low turbidity waters have relatively low light attenuations, so even the physically deep waters have a high bottom effect. Therefore, these “deep clear water” locations should be classified as optically shallow waters. Figure 2-13c presents the bottom effect index expressed as isolines as a function of the depth and turbidity (R_{rs} ratio). The BEI 0.2 isoline (blue shaded area) expresses the threshold between optically shallow and optically deep waters that effectively separates high/low bottom effect zones. High turbidity waters lead to high light attenuation which indicates a much lower amount of light was reflected upwards by the bottom, so only very shallow waters (less than 1 meter) were classified as optically shallow waters. In contrast, the low turbidity waters have relatively low light attenuations, so even the deeper sample locations have a high bottom effect and should therefore be classified as optically shallow waters. Therefore, it is clear that utilizing the BEI metric leads to a more accurate adaptive approach than using our depth metric. Moreover, it can be easily derived and applied to many other aquatic remote sensing studies for fast identification of those areas where bottom reflectance influences CDOM measurements.

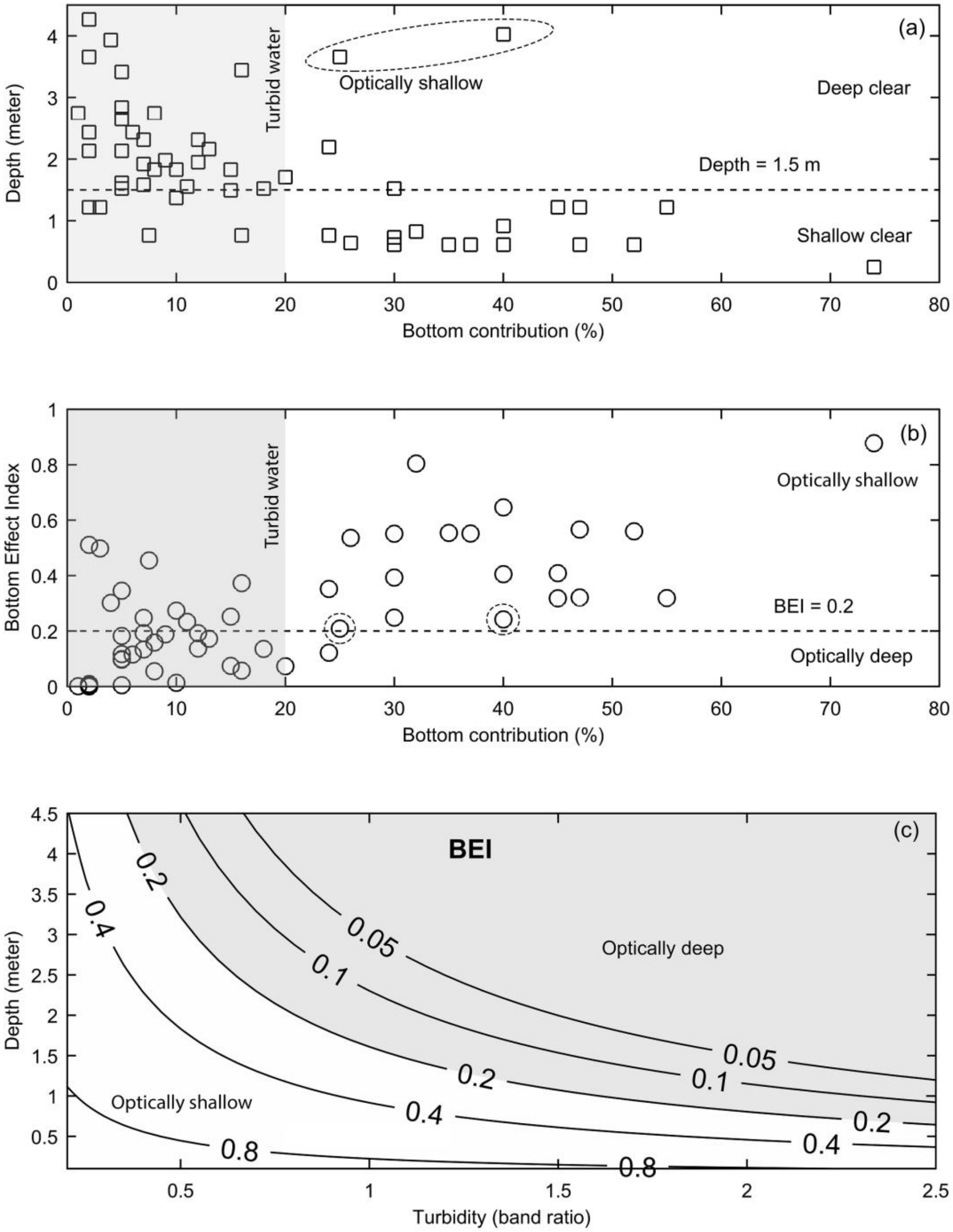

Figure 2-13: The bottom contribution vs. depth (a) and bottom contribution vs. bottom effect index (b) for individual samples. The turbid water samples indicate that the bottom contributions are less than 20%. Two deep clear water samples with high bottom contribution were reasonably categorized as optically shallow water by the BEI method, different from using our Depth threshold. Panel c plots the BEI value as isolines as a function of the depth and turbidity. The BEI considers both the bathymetry and water column attenuation to separate the optically shallow and optically deep waters.

2.5 Conclusions

The optically shallow inland and coastal waters are important pathways for exporting terrestrially derived carbon sources into aquatic ecosystems. However, bottom reflectance introduces high uncertainty to the remote sensing estimation of water bio-optical properties (e.g. $a_g(440)$). In addition, for terrestrial carbon dominated freshwater environments, CDOM levels exhibit a very broad range (e.g. 0.12 m^{-1} to 8.46 m^{-1} in this study). These two characteristics present challenges for the remote sensing retrieval of freshwater biogeochemistry in the coastal and inland waters. Based on multi-date *in situ* measurements, this study developed an efficient shallow water CDOM estimation algorithm (SBOP). The overall performance evaluation (RMSE = 0.22 and R^2 = 0.74) demonstrated that the SBOP algorithm can be successfully applied to the optically shallow fresh waters with relatively homogeneous bottom sediments/conditions.

Ultimately, the SBOP model is uniquely designed for estimating CDOM absorption in optically shallow waters by taking into account the bottom reflectance component of total upwelling radiance. The SBOP algorithm significantly outperforms QAA-CDOM in these optically shallow waters (SBOP R^2 = 0.74 and QAA-CDOM R^2 = 0.48). In addition, the algorithm separately derives CDOM absorption as opposed to a combined absorption a_{dg} from prevailing ocean color algorithms. The removal of bottom effect from total radiance reduces the CDOM estimation uncertainty, and therefore extends effective carbon monitoring capabilities to optically shallow inland and coastal waters.

Widespread monitoring of water carbon from remote sensing data in the inland and coastal shallow waters demand the processing of large volumes of satellite data. We propose a BEI adaptive approach for algorithm selection. The BEI is designed to improve the computation efficiency for the regions having reliable bathymetry data, which are largely available for near-coastal and inland shallow waters. The BEI is able to quickly identify bottom contaminated water spectra/pixels based on both the bathymetry and water turbidity, so as to differentiate optically shallow waters. The BEI adaptive approach (BEI $R^2 = 0.81$) can efficiently as well as accurately aid in the selection of the proper algorithm for the estimation of water CDOM absorption.

In summary, our study investigated the potentials of remote sensing methods for capturing seasonal and spatial dynamics of CDOM in optically shallow water environments. Our newly developed SBOP algorithm offers a new inversion algorithm that directly considers bottom effect in radiative transfer equation. The BEI based adaptive approach presents a more efficient and fast method for monitoring terrigenous carbon export to inland and coastal waters with broad CDOM conditions. The outcome of this investigation will ultimately improve the monitoring of carbon pools and their transport gradients and mechanisms from terrestrial to aquatic systems at both regional and global scales.

CHAPTER 3

SPATIO-TEMPORAL VARIATIONS OF CDOM IN INLAND WATERS FROM A SEMI-ANALYTICAL INVERSION OF LANDSAT-8

3.1 Abstract

Bottom reflectance is often the main cause of high uncertainty in Colored Dissolved Organic Matters (CDOM) estimation for optically shallow waters. This chapter presents an improved Shallow Water Bio-optical Properties (SBOP) algorithm compared to normal deep water CDOM algorithm to overcome bottom effects from Landsat-8 OLI imagery. So SBOP algorithm could successfully observe spatial and temporal CDOM dynamics in inland waters. We evaluated the algorithm via 130 images and a large set of field measurements collected across seasons of multiple years in the Saginaw Bay, Lake Huron and fourteen lakes of different sizes in the northeastern USA. Results showed that the SBOP algorithm reduced estimation errors by as much as 4 times (RMSE = 0.17 and R^2 = 0.87 in the Saginaw Bay; R^2 = 0.80 in the northeastern lakes) when compared to the QAA-CDOM algorithm that did not take into account bottom reflectance. These improvements in CDOM estimation are consistent and robust across lakes with broad characteristics (coastal ecology, sizes, and different depth). Our analysis revealed: 1) the proposed remote sensing algorithm resulted in significant improvements in tracing spatial-temporal CDOM inputs from terrestrial environments to lakes, 2) CDOM distribution captured with high resolution land-viewing satellite is useful in revealing the impacts of terrestrial ecosystems on the aquatic environment, and 3) Landsat-8 OLI, with its 16 days revisit time, provides valuable time series data for studying CDOM

seasonal variations at land-water interface and has the potential to reveal its relationship to adjacent terrestrial biogeography and hydrology. The chapter presents a shallow water algorithm for studying freshwater or coastal ecology, as well as carbon cycling science.

3.2 Introduction

The assessment of Colored Dissolved Organic Matter (CDOM) in lake waters help the scientific community better understand both global/regional carbon cycling and aquatic ecosystem biogeochemistry. CDOM can be used as a surrogate for terrestrially derived dissolved organic carbon (DOC) transport (Kutser et al. 2015). The export of terrestrial DOC to lakes and oceans represents a significant carbon exchange at the land-water interface (Roulet and Moore 2006; Tian et al. 2013). This carbon flux is a key pathway leading to widespread CO_2 supersaturation in aquatic environments (Jonsson et al. 2003; Sobek et al. 2005). Inland waters also play a significant role in the sequestration, transport and mineralization of terrestrially sourced organic carbon (Battin et al. 2009). In addition, soil carbon loss to rivers and lakes has an important impact on net terrestrial carbon budgets (Davidson et al. 2010). CDOM in inland waters also influences the aquatic ecosystem in a variety of ways (Williamson et al. 1999). CDOM in inland water absorbs short wavelength incoming light, and this absorption will further affect the growth of plankton communities (Diehl 2002; Williamson et al. 1996). Moreover, terrestrial DOC transportation to inland waters represents a very important nutrient exportation pathway from land to water (Cole et al. 2007). These terrestrial carbon inputs will ultimately impact the food webs within the lake environment (Brezonik et al. 2015; Cole et al. 2006).

Remotely sensed satellite imagery provides an efficient solution for monitoring CDOM dynamics (Keith et al. 2016). The remote sensing estimation of water biogeochemistry is based on observation of water bio-optical components, including CDOM, which influence the underwater light field (Hoge and Lyon 1996; Yu et al. 2010), and therefore leads to changes in water leaving radiance received by the satellite sensor (Zhu et al. 2011). Previous research centered on inland and coastal water CDOM estimation by high resolution satellite data often relied on empirical band ratios algorithms, which were developed for specific study areas and require additional intensive regional tuning when applied or upscaled to other regions (Kutser et al. 2005; Mannino et al. 2008). Location-independent semi-analytical algorithms based on bio-optical water radiative transfer models have been developed to improve the retrieval of water biogeochemistry, particularly chlorophyll absorption (Carder et al. 1999; Kahru and Mitchell 2001; Le et al. 2013). In addition, the need to better estimate carbon amounts in coastal regions resulted in the development of several semi-analytical algorithms designed to retrieve CDOM absorption in optically deep waters (Matsuoka et al. 2013; Shanmugam 2011; Zhu and Yu 2013). Unfortunately, these semi-analytical CDOM algorithms are not applicable to optically shallow waters, and therefore remote sensing techniques are limited for assessing carbon dynamics at the land-water interface. An algorithm specific to the estimation of CDOM in inland, optically shallow waters is needed.

Growing interest in inland water CDOM observation via remote sensing requires suitable satellite images with both the proper spectral wavelengths and finer spatial resolution (Brezonik et al. 2015; Palmer et al. 2015). Semi-analytical algorithms for (Chlorophyll or CDOM) typically use an “ultra-blue” band (e.g. from 435 nm to 450 nm) to build the bio-optical model (Lee et al. 2002). Because studies often used CDOM absorption in the ultra-blue band to present CDOM levels, previous studies are mainly based on the ocean-viewing multispectral or hyperspectral satellites, such as MODIS, SeaWIFS and EO-1 Hyperion that record data in this wavelength domain (Kutser et al. 2005; Miller and McKee 2004; O'Reilly et al. 1998). However, these images are not applicable to studies involving smaller inland lakes and rivers because of coarse spatial resolutions (e.g. MODIS) or narrow coverage (e.g. Hyperion). Rivers, that are important pathways for transporting terrestrial CDOM, typically have a width narrower than two kilometers (Allen and Pavelsky 2015). The spatial resolution or pixel size of most ocean-viewing sensors such as MODIS are far too coarse to observe inland waters, and much uncertainty is introduced when these images contain land-water mixed pixels (Zhu et al. 2013a). In contrast, the experimental high resolution hyperspectral sensor Hyperion provided the spatial resolutions needed for inland waters, but it isn’t operational now and its utility was very limited with respect to terrestrial CDOM estimation due to its narrow and limited worldwide image footprint or coverage (Zhu and Yu 2013). In recent years, several multispectral land-viewing satellite sensors have offered new promise for the retrieval of inland water bio-optical properties with the addition of an ultra-blue band, predominantly, Landsat-8 (30 m spatial resolution) (Roy et al. 2014). With its relatively high spatial resolution, Landsat 8 is able to effectively capture images of the lower reaches and plumes of rivers, thereby increasing its potential for observing inland water biogeochemistry (Pahlevan et al. 2014). Several empirical algorithms have been applied to Landsat-8 images for observing CDOM absorption based on band-ratio methodologies in optically deep waters as mentioned above (Chen et al. 2017; Kutser et al. 2016a; Olmanson et al. 2016).

This chapter continues validates the SBOP algorithm (Li et al. 2017), an approach to create a semi-analytical CDOM estimation algorithm for Landst-8 multispectral imagery in shallow waters.. To our knowledge, our research represents the first attempt to explore a semi-analytical CDOM retrieval algorithm for Landsat-8 multispectral imagery in shallow waters. SBOP was initially developed based on *in situ* spectroradiometer data. This study investigates its application to Landsat-8 OLI images and evaluates the effectiveness of the multispectral land-viewing images on the retrieval of CDOM absorption at a large number of lakes with significant variations in biogeochemical properties. Our approach strives to address the challenges of employing appropriate atmospheric correction, determining the influence of bottom reflectance, and refining a semi-analytical algorithm for bio-optical properties retrieval in optically shallow waters. Finally, 130 satellite images were processed and analyzed, 84 from Saginaw Bay, Lake Huron as principal study sites and 46 from northeastern USA inland lakes/estuaries to better understand CDOM spatio-temporal dynamics and its associated driving factors.

3.3 Method

3.3.1 Study sites

Saginaw Bay, Lake Huron was selected as our principal study site to develop our Landsat-8 methodologies (Figure 3-1). A total of four data collection cruises were conducted in Saginaw Bay and vicinity to conduct *in situ* sampling focused on CDOM spatial variations. The field data generated from two of these collection cruises were used as algorithm validation data because their collection dates corresponded nicely to the overpass dates of select Landsat-8 satellite images. Fortunately, Saginaw Bay and the Saginaw River near their interface exhibit a wide range of CDOM levels, dynamically changing throughout the seasons. This variability makes this location perfect for testing if indeed satellite images can adequately capture CDOM seasonal dynamics in optically shallow waters. Generally, the major bottom sediments in Saginaw Bay were sand with the intermittent spot of aquatic plants and benthic algae. Moreover, the different landcover types surrounding Saginaw Bay also provide an opportunity to study the impact of various terrestrial CDOM export pathways into an aquatic ecosystem. For example, east coast of Saginaw Bay is dominated by agricultural cropland, while west coast of Saginaw Bay is dominated by a mixture of agriculture and forest. In addition, two major coastal wetland areas border Saginaw Bay and the Saginaw River, Wigwam Bay State Wildlife Area and Shiawassee National Wildlife Refuge, respectively. Saginaw River represents the largest river discharging into Saginaw Bay and has an overall length of 36 km and a watershed area of 22,260 square km^2. Also, there are several major agricultural drainage channels that discharge into Saginaw Bay.

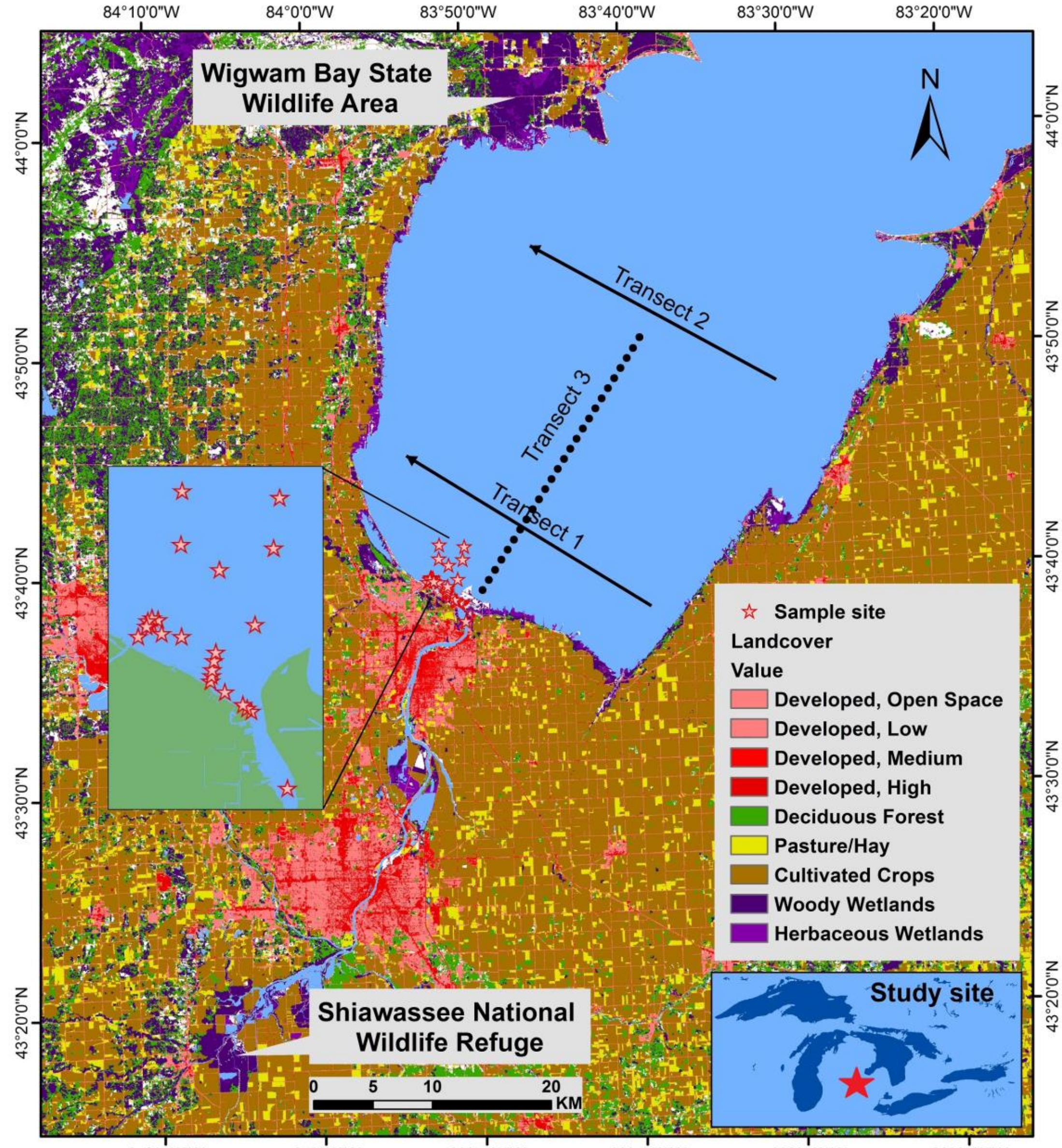

Figure 3-1: The study area of Saginaw Bay, Lake Huron. The surrounding area contains varied landcover types, including wetlands, agricultural cropland, and forest. Red stars marked the filed samplings locations.

Fourteen diverse freshwater lakes and the Great Bay estuary complex located in northeastern USA were selected to further validate the transferability and scalability of the algorithm to a different ecoregion, and to evaluate to what extent CDOM spatio-temporal dynamics can be monitored (Figure 3-2 & Figure 3-3). Northern New England USA (Maine, New Hampshire, Vermont / NNE) is dominated by Eastern Temperate Forest with areas of Atlantic Maritime Highlands, Northeastern Coastal Zone, and Acadian Plains and Hills (Omernik 1987). Most lakes are classified as being in "good" condition based on a suite of assessment parameters (e.g., chlorophyll-a, secchi depth, plankton, total phosphorus, taxa, lake shore habitat) with half of all lakes falling within the mesotrophic category (Torbick et al. 2014). Lake Champlain is located along the border between the states of New York and Vermont with the area of 1,269 km^2. The Great Pond (34.5 km^2) and China Lake (15.6 km^2) are located in the state of Maine. The Great Bay estuary complex (24 km^2), Baxter Lake, Swains Lake, Northwood Lake and Brindle Lake are located in southern New Hampshire. The Lake Winnipesaukee (180 km^2), Newfound Lake (18 km^2), Webster Lake, Pleasant Lake, Sunapee Lake, Crystal Lake and Mascoma Lake are located in the northern New Hampshire. The Great Bay is a drowned river valley which located in the Gulf of Maine watershed. The water of Great Bay flowed into the Piscataqua River. The contributing areas of these northeastern lakes have different landcover types. As one might expect due to their wide distribution, the landcover surrounding these lakes is highly varied. This variation in landcover, and thus CDOM levels, is ideal for algorithm validation. For example, the north and east coast regions of Lake Champlain are dominated by agricultural farmlands, while the west coast regions are generally covered by mixed forests. Generally, southern New Hampshire has more agricultural land that gradually transitions into mixed forest to the north.

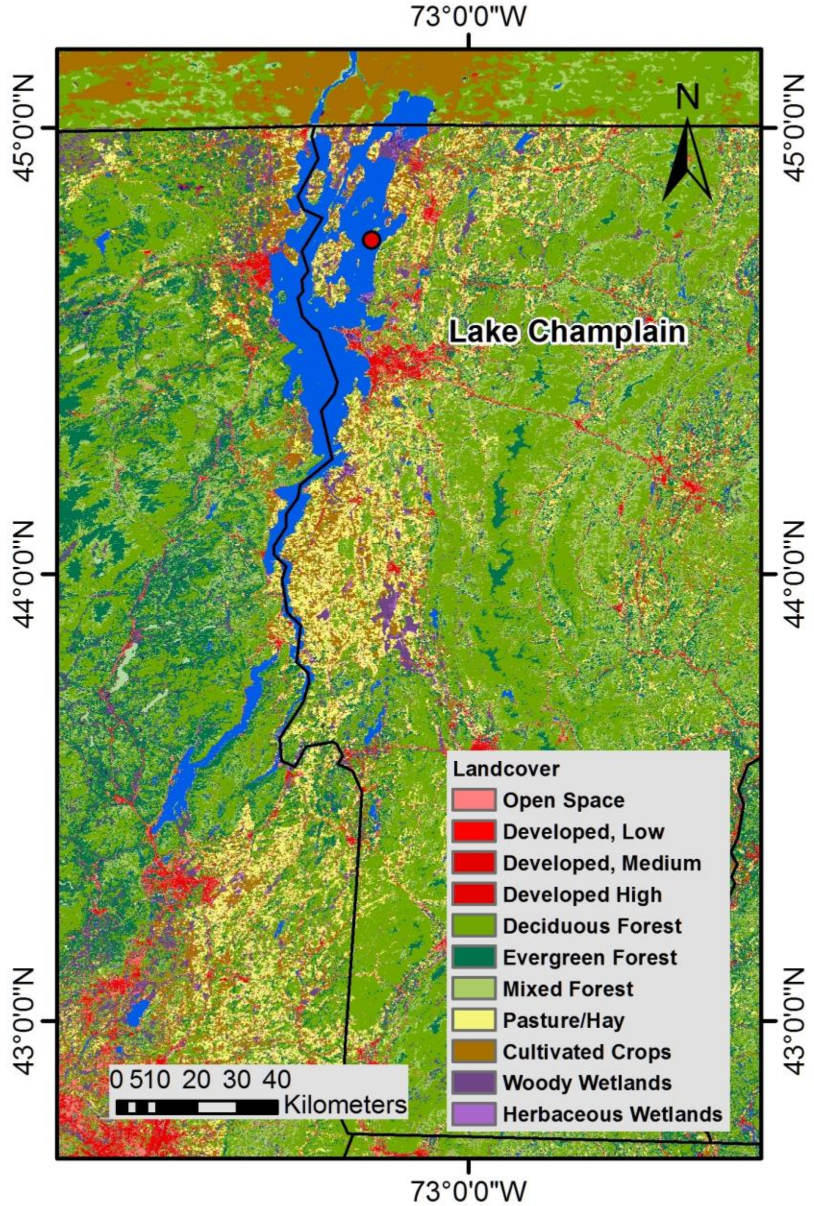

Figure 3-2: Lake Champlain was in the state boundary of New York and Vermont. It was surrounded by different terrestrial landcover. A large area of cropland was in north coast regions.

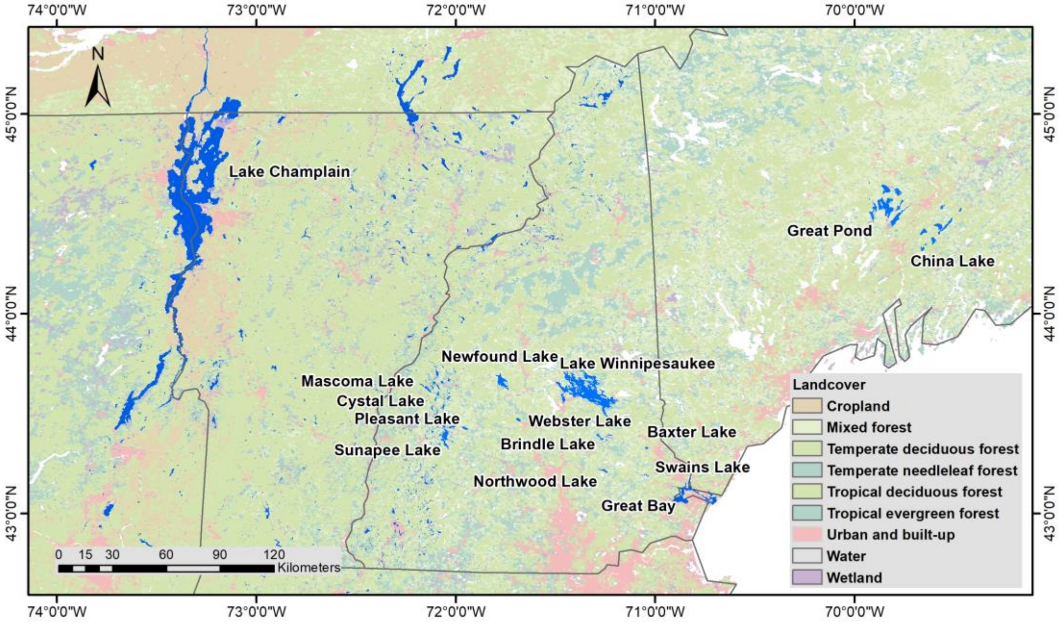

Figure 3-3: The 14 freshwater lakes and Great Bay in the northeastern of US. These freshwater lakes were important drinking water sources.

3.3.2 Processing of the Landsat-8 images

Landsat-8 satellite was launched in February 2013, with the addition of a new coastal blue band (443 nm). Its worldwide spatial coverage and high spatial resolution show promise for inland water CDOM monitoring. A total of 11 images were identified for validation of the SBOP algorithm in the two regions because their overpass date corresponded to our field sampling date. First, 84 Saginaw Bay images (path 20-21, row 29-30) between May 2013 and Feb 2016 were processed. Of these, most of the images were acquired between March and November in all four years. Ice cover and high cloud cover (> 20%) plagued most of the images during winter months. Two images (May 1, 2013 and May 7, 2015) nicely corresponded to our field sampling date for comparison against our field measurements. Satellite image derived CDOM information from 56 images were selected to discuss the CDOM spatial-temporal dynamics. The other 25 processed images didn't have positive output results due to the cloud coverage. Second, 46 images of the northeastern USA (paths 12-14, rows 29-30) were processed in northeastern USA lakes and Great Bay estuary. Analogous to the approach outlined above, a subset of 9 images were selected to be compared to our field sampled CDOM measurements for model validation.

Level-1 satellite images were selected to process. The initial step of satellite image processing was the removing of atmospheric effect. This processing aims to derive the spectra data which only contains water body information. The processing was beginning at the top of atmospheric (TOA) radiance and ending at the remote sensing reflectance. The atmospheric correction was processed through ACOLITE software. TOA reflectance ($\rho_t(\lambda)$) could be divided as the following different components as (Gordon and Wang 1994):

$$\rho_t(\lambda) = \rho_r(\lambda) + \rho_a(\lambda) + t_v\rho_{wc}(\lambda) + T\rho_g(\lambda) + t_0 t_v \rho_w(\lambda) \quad (1)$$

In the equation, the λ means wavelength of the light. $\rho_r(\lambda)$ is reflectance which is caused by Rayleigh scattering during transfer in the atmosphere. $\rho_a(\lambda)$ is the reflectance which is caused by aerosol (solid particles or water droplets in the air) scattering. $\rho_{wc}(\lambda)$ is light signal which is reflected by foams and whitecaps of water surface. $\rho_g(\lambda)$ is sun light specular reflectance of water surface which also can be called as the sun glint. $\rho_w(\lambda)$ is water-leaving reflectance which only contained information of water column. T is direct transmittance which represented the path from the water surface to satellite sensors. t_0 is atmospheric diffuse transmittance which represented the path from the sun to the water surface. t_v is the diffuse transmittance which represented the path from the water surface to the satellite sensor. The processing of the atmospheric correction aims to derive the water leaving radiance ($\rho_w(\lambda)$) from the TOA reflectance ($\rho_t(\lambda)$). From the TOA, the radiance measured at the top of atmospheric $L_t(\theta, \varphi)$ is:

$$L_t(\theta, \varphi) = L_{path}(\theta, \varphi) + t(\theta, \varphi) L_{w(total)}(\theta, \varphi) \qquad (2)$$

Where the $L_{path}(\theta, \varphi)$ is the radiance along the path of the atmosphere. $L_{w(total)}$ is the radiance in just above the water surface. The transmittance t could be calculated as the equation as:

$$t(\xi) = \frac{L_w^{(TOA)}(\xi)}{L_w(\xi)} \qquad (3)$$

In the equation, the $L_w(\xi)$ is the water leaving radiance from the water body as the direction of ξ, the $L_w^{(TOA)}(\xi)$ is the radiance which is contributed by the water in the TOA (Gordon 1997). Then the t_0 and t_v could be estimated through:

$$t = \exp[-(\frac{\tau_r}{2} + \tau_{oz})/cos\theta] \qquad (4)$$

Where the τ_r is the average optical thickness for having the Rayleigh scattering. τ_{oz} is the optical thickness for the Atmosphere Ozone (Wang 2000). In the equations for calculating the TOA reflectance, the $\rho_r(\lambda)$ could be built from the empirical database which is generated under the wind speed as the key controlling factor. (Gordon and

Wang 1992). The components contributed by the whitecaps and foams of the water surface can be calculated as:

$$S_{wc} = 2.95 \times 10^{-6} U^{3.52} \tag{5}$$

Where the S_{wc} is the proportion of the whitecaps in the water surface. The U is the wind speed for controlling the whitecaps proportion. Therefore, the reflectance contributed by the whitecaps can be estimated as following:

$$\rho_{wc}(\lambda) = 0.22\epsilon_{wc}(\lambda)S_{wc} \tag{6}$$

Where the ϵ_{wc} is the empirical spectral curve profile of the whitecaps (Gordon and Wang 1994). Due to the viewing angle of the Landsat-8 satellite sensor, the $\rho_g(\lambda)$ is often ignored in the processing. Then the marine reflectance at two wavelength ($565nm, 670nm$) often have the constant linear relationship, so the $\rho_a(\lambda)$ is modeled as (Ruddick et al. 2000):

$$\rho_w(670) = a\rho_w(565) + b \tag{7}$$

where a and b are constant values. Then the key information, the $\rho_a(\lambda)$ was calculated as the SWIR methods as:

$$\rho_a(\lambda) = \ \epsilon_a R(\lambda)_e \Delta R(\lambda) \tag{8}$$

Where the $R(\lambda)_e$ is corrected from the SWIR bands and the $\Delta R(\lambda)$ is the correction factor (Vanhellemont and Ruddick 2015).

The Figure 3-4 shows the comparisons between the TOA (Figure 3-4a) and water leaving reflectance in the Saginaw Bay (Figure 3-4b). After the atmospheric correction, we can visually examine that the image was corrected by removing atmospheric effects (Figure 3-4b). Only some heavy cloud coverage regions (white color) cannot be corrected. These cloud regions would be masked out in the next processing step. The contributions along the path from the water surface to the top of atmosphere were corrected. After the atmospheric correction, the image now contain the reflectance which was only from the water. So we can derive the optical information of the water regions from the corrected image.

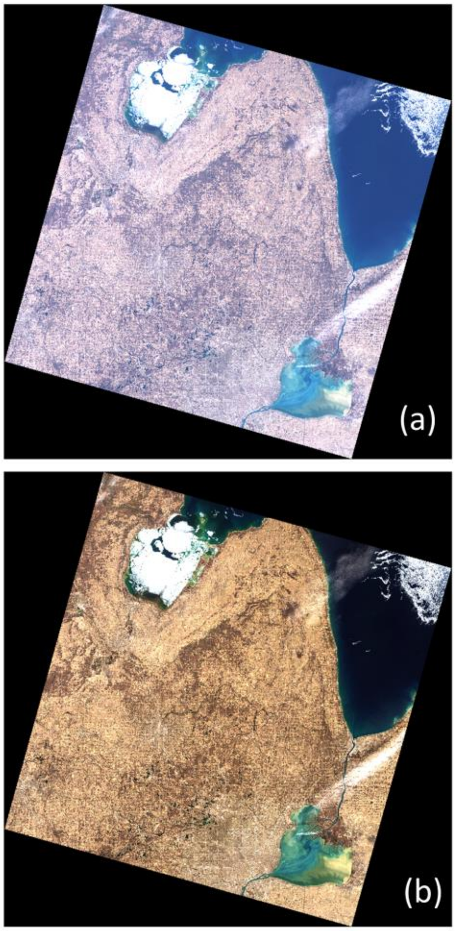

Figure 3-4: The RGB display of the satellite image of TOA and water leaving reflectance. Atmospheric effects were removed from the satellite images.

After the correction of the atmospheric effect in the satellite images, the next step aims to derive the water body extent from the entire image. The whole satellite image often cover a large area of the land surface. The reflectance of these terrestrial objectives often had much higher values than the water bodies. Normally, the signal levels of vegetations, bare land surface, and human constructions were at least one magnitude higher than lakes and rivers. If we visually check the different objectives through the Figure 3-4, we can find most of the lake water regions showed dark color which indicated low signals. Therefore, the removing of the land surface would be helpful for reducing computation times and image illustration.

The normalized difference water index (NDWI) was used to separate water bodies from land surface. The NDWI used band ratio for detecting the water boundaries (Stedmon et al. 2006). It aims to derive the water bodies by comparing the signal levels in green and near-infrared bands. The NDWI can be calculated as the function of NDWI = (Green – NIR) / (Green + NIR), where the Green means the wavelengths from the 533 nm to 590 nm and the NIR means the near-infrared bands from 851nm to 879 nm. The output values of the water bodies were positive values. Then the water bodies can be derived from the atmospherically corrected images. The Figure 3-5 shows the water bodies delineation result in 443 nm. The large terrestrial surface areas were masked out from the image. Meanwhile, the cloud regions were also masked out. Moreover, the floating ice in the lake surface had significantly abnormal values which could be easily excluded in the processing of the SBOP algorithm. Then the following steps would be processed based on the water bodies only images.

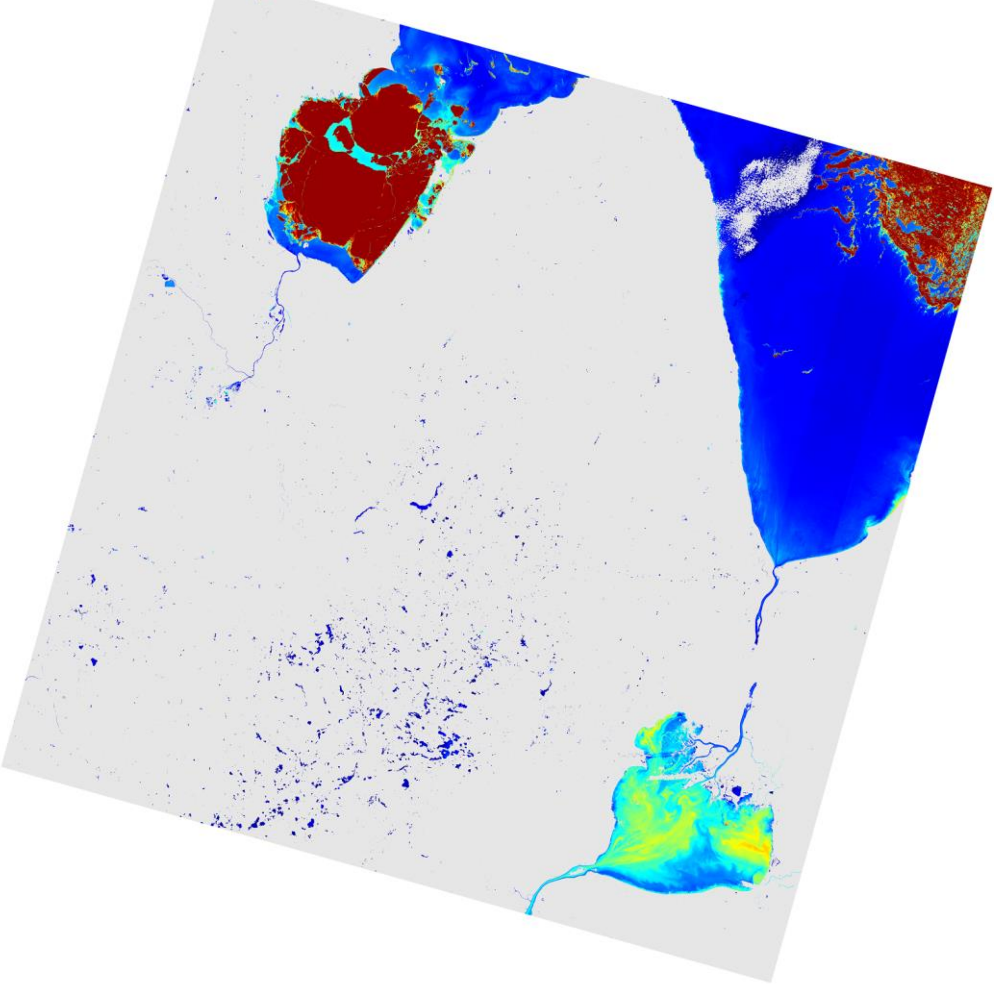

Figure 3-5: Remote sensing reflectance at the 443 nm without the land targets. Water bodies were identified by the NDWI index.

SBOP algorithm selected four wavelengths to calculate CDOM absorption. These four wavelengths were 440 nm, 490 nm, 555 nm, and 640 nm. The selection was agreeing with the other water semi-analytical algorithms, like QAA and QAA-CDOM. The consistent wavelengths would be helpful in algorithm incorporation and comparison. The central wavelengths of the Landsat-8 satellite images were 443 nm (coastal blue), 483 nm (blue), 561 nm (green), and 655 nm (red). So I interpolated the SBOP required remote sensing reflectance ($R_{rs-SBOP}(\lambda)$) from the four Landsat-8 remote sensing reflectance ($R_{rs-Lat}(\lambda)$) through the spectral reference data as (Barsi et al. 2014):

$$R_{rs-SBOP}(440) = R_{rs-Lat}(443) * 0.990 \quad (9)$$

$$R_{rs-SBOP}(490) = R_{rs-Lat}(483) * 1.032 \quad (10)$$

$$R_{rs-SBOP}(555) = R_{rs-Lat}(561) * 0.987 \quad (11)$$

$$R_{rs-SBOP}(640) = R_{rs-Lat}(655) * 0.968 \quad (12)$$

Then the remote sensing reflectance could be processed by SBOP algorithm for the lake water CDOM estimation.

3.4 Results and Discussions

3.4.1 Landsat-8 satellite images CDOM estimation validations

The CDOM absorption values derived from the Landsat-8 OLI images were validated with the laboratory measurement of CDOM in water samples. The results showed the SBOP algorithm can be effectively applied to optically shallow waters with relatively homogenous bottom sediment to improve the accuracy of CDOM estimation (Table 3-1). A representative optically deep water semi-analytically algorithm (i.e .QAA-CDOM) was chosen to compare with the SBOP algorithm in the Saginaw Bay area (Zhu et al. 2014). Both SBOP and QAA-CDOM are the semi-analytical algorithm with the same strategy for designing the absorption coefficient. The SBOP remarkably outperformed QAA-CDOM with respect to all four error metrics. The SBOP algorithm achieved a R^2 of 0.87, much higher than that of the QAA-CDOM algorithm (R^2 =0.33). The substantially larger bias (MNB) and error (AME) of QAA-CDOM (MNB = 1.65 and AME = 1.82) showed that it overestimates CDOM levels dramatically. The filed sampling sites majorly concentrated in Saginaw River and nearshore regions (depth was less than the 2 m). These shallow water sites were largely affected by the bottom reflectance. So, the normal deep water CDOM estimation algorithm could not be easily applied to these shallow water regions. However, SBOP algorithm was designed to include the bottom contributions in the underwater light field modeling. It can largely reduce the estimation errors caused by the bottom reflectance. Due to the improvements of SBOP algorithm, CDOM absorption could be estimated through the Landsat-8 images in the inland waters.

Table 3-1: The validation results from both the SBOP and QAA-CDOM algorithms

Method	RMSE	MNB	AME	R^2
SBOP	0.17	-0.12	0.22	0.87
QAA-CDOM	0.48	1.65	1.82	0.33

To examine how errors change across sampling locations, $a_g(440)$ derived from satellite images vs. field measured $a_g(440)$ from field water samples were plotted in Figure 3-6. These samples are located at a range of depth between 0.6 to 4 meters, including both optically shallow and optically deep waters. The samples were categorized as shallow (depth < 1 m), medium (1 m < depth < 2 m) and deep waters (depth > 2 m) to evaluate algorithm performances respect to bottom contribution. Generally, in Saginaw Bay, the shallow (depth < 1m) and medium (1 m < depth < 2 m) sites had the bottom reflectance over 10% to the total water leaving radiance. The shallow water sites are in Saginaw River and near shore regions. In these shallow areas in the similar rages of CDOM values, SBOP produced much better results than QAA-

CDOM algorithm. In contrast, the largest errors of the QAA-CDOM algorithm resulted in these shallow areas. In optically shallow water sites, the underwater light reflected by bottom sediments significantly contributes to water-leaving radiance, some of which is received by the satellite sensor. QAA-CDOM essentially does not consider bottom reflectance and includes it as a component of water column reflectance, which leads to the overestimation of CDOM absorptions due to its calculation strategy. The higher the proportion of bottom reflectance included in the total water leaving reflectance, the higher the uncertainties resulting from QAA-CDOM. QAA-CDOM could produce a few accurate results in medium and deep depth waters. Almost half of the field sample locations in southern Saginaw Bay regions were classified as optically shallow water according to field measured depth results (depth < 1.5 m). Our results show QAA-CDOM is not directly applicable to these shallow waters. On the contrary, the SBOP algorithm considers bottom reflectance in the water radiative transfer model and treats r_{rs} as a sum of both water column and bottom sediment reflectance. Moreover, bottom reflectance also involved in the total water leaving radiance in deep depth and clean waters (Li et al. 2017). So SBOP demonstrated a marked advantage over QAA-CDOM for estimating CDOM in a broad range of inland waters.

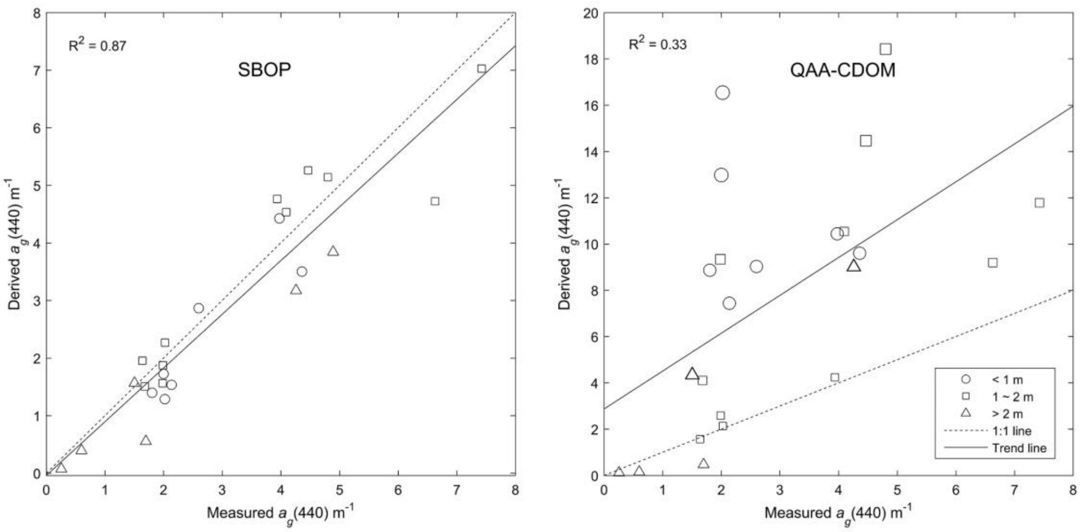

Figure 3-6: Image derived vs measured a_g(440) from both SBOP and QAA-CDOM algorithms in Saginaw Bay. The larger symbol size indicated the higher error of the algorithm. Water samples were separated by the depths of field sampling sites.

The SBOP algorithm was further validated via the fourteen northeastern USA lakes and the Great Bay estuary complex by comparing the image retrieved CDOM absorption and field sampled CDOM absorption (Figure 3-7). As most of the waterbodies are small and appear spatially homogeneous, mean CDOM absorption of non-cloud covered pixels was calculated to represent a single lake CDOM level. As Figure 3-7 illustrates, SBOP algorithm performed well across this broad range of lake types. The addition of these additional validation sites seems to confirm that SBOP algorithm can be effectively applied to multi-spectral Landsat-8 images of inland waters. Moreover, Landsat-8 OLI imagery, particularly the four bands (443nm, 482nm, 561nm, and 654nm), provide sufficient spectral information to retrieve inland water CDOM levels. Ultimately, if a proper algorithm like SBOP is used, the spectral, radiometric and spatial resolutions of Landsat-8 OLI imagery are capable of achieving large-scale lake/estuary CDOM monitoring.

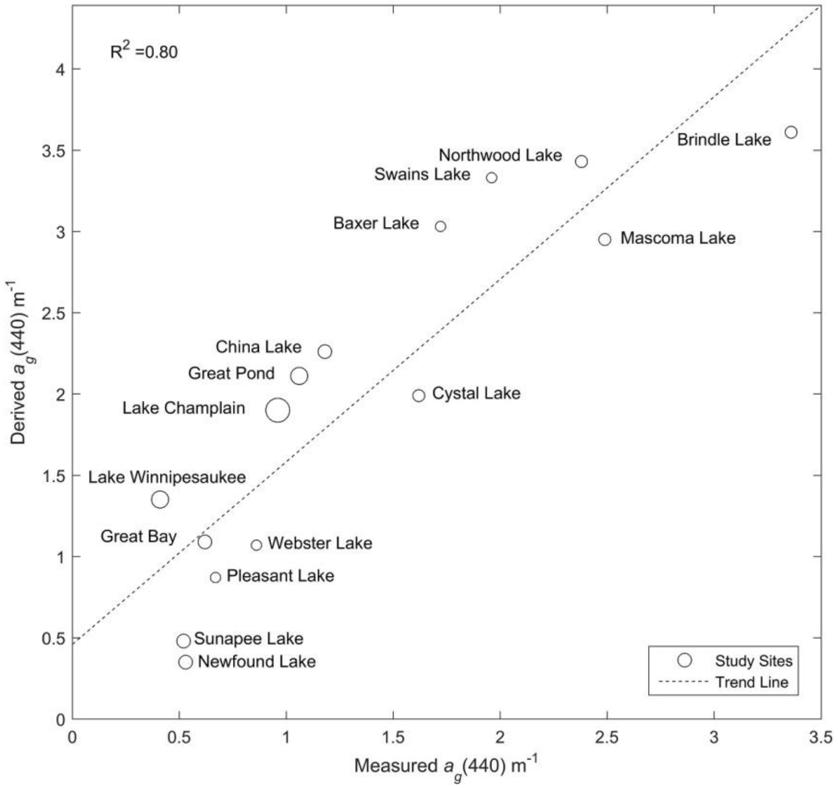

Figure 3-7: The SBOP algorithm validations in the 14 northeastern lakes and Great Bay. SBOP algorithm and Landsat-8 satellite images could be applied in broad types of inland waters to derive CDOM absorption.

3.4.2 CDOM spatial patterns from land to water

CDOM spatial distribution from the Saginaw River into Saginaw Bay in July 2013, April 2015 and September 2015 are illustrated in Figure 3-8. The lake water CDOM levels in Saginaw Bay displayed distinct spatial heterogeneity. The CDOM level significantly decreased from shallow near shore regions to the deeper inner bay. CDOM was highest around the near shore regions where rivers and agricultural channels discharged into Saginaw Bay. For example, CDOM levels in Saginaw River and channels were almost two times higher than that of Saginaw Bay. Specifically, Saginaw River had much higher CDOM levels than the other regions of Saginaw Bay for three non-winter seasons.

Scenes in Figure 3-8 strongly suggested that large amounts of CDOM were transported by this river system to the lake waters.

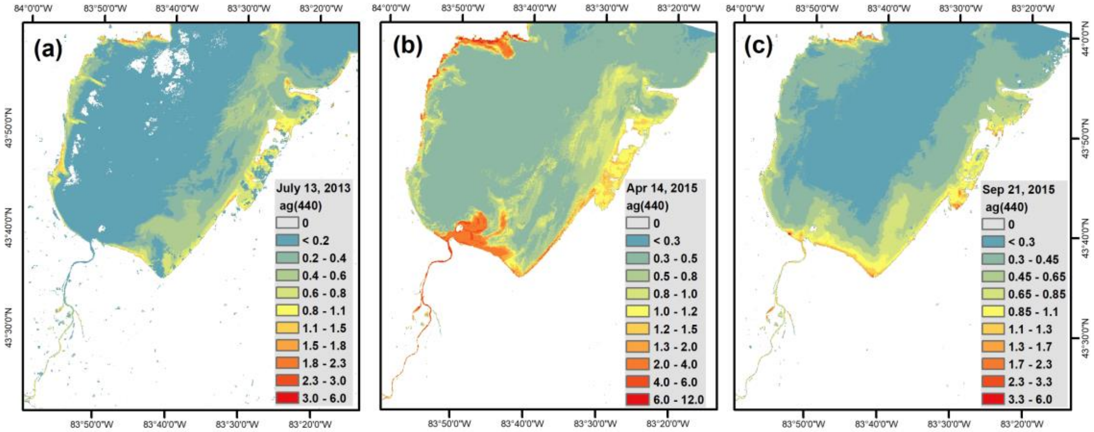

Figure 3-8: Spatial distribution of $a_g(440)$ across three different seasons in Saginaw Bay.

In order to more closely examine CDOM spatial distribution from the river into Saginaw Bay, CDOM absorption at 440 nm for five non-consecutive months across three years was plotted (Figure 3-9) along transect 3 shown in Figure 3-1. The point locations along transect 3 were evenly distributed from the Saginaw River mouth out into the inner Bay at an interval of 1 km. Figure 3-9a shows that CDOM absorption decreased almost by a factor of four in 10 kilometers moving towards the inner bay. Similar data generated from September 2015 imagery for two additional transects (transect 1 & transect 2) is shown in Figure 3-9b. Both transects are oriented from east to west, roughly perpendicular to transect 3. Transect 1 is located near the Saginaw River plume region while transect 2 is located in the inner Bay region. The CDOM levels along the nearshore transect (transect 1) were two times higher than CDOM levels within the deeper inner bay (transect 2).

Two groups of the transects were further applied along the west and east coast, respectively (Figure 3-10). The transect started from north to east along the coastline at the interval of 1.5 km. In the Figure 3-10a, these transects were located near the east coast regions. The CDOM levels decreased from the nearshore regions to the inner Bay regions. CDOM peak levels in east transects were the small agricultural channels along the shore regions. In the Figure 3-10b, the transects were located near the west coast regions. Similar decreasing patterns were showed from the nearshore regions to the inner Bay regions. By combination analysis of all the transects in the Figure 3-10, we can find the CDOM decreased almost two times in the distance of 3 km from land to water. Meanwhile, CDOM values in the east coast were higher than west coast.

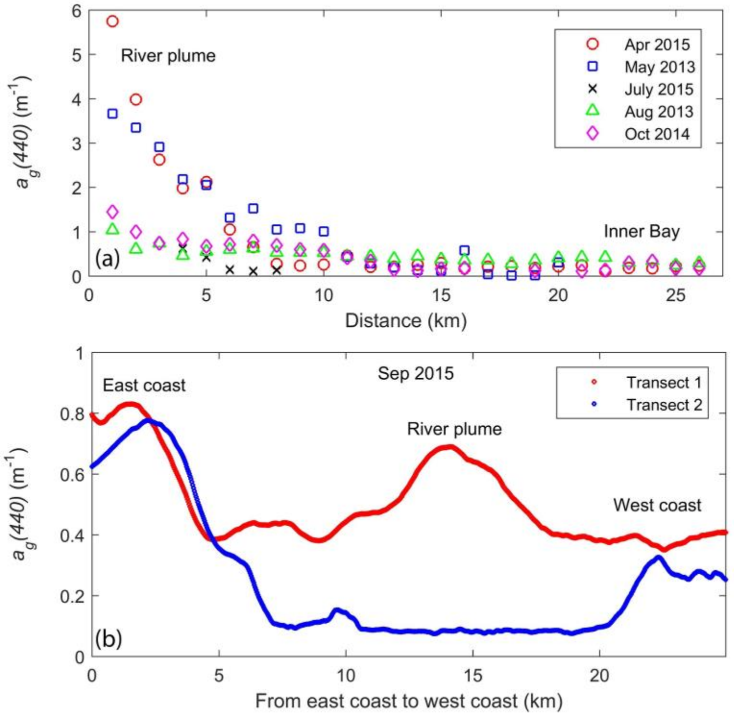

Figure 3-9: CDOM spatial patterns in the Saginaw Bay. CDOM shows the decreased pattern from river plume regions to the inner Bay regions.

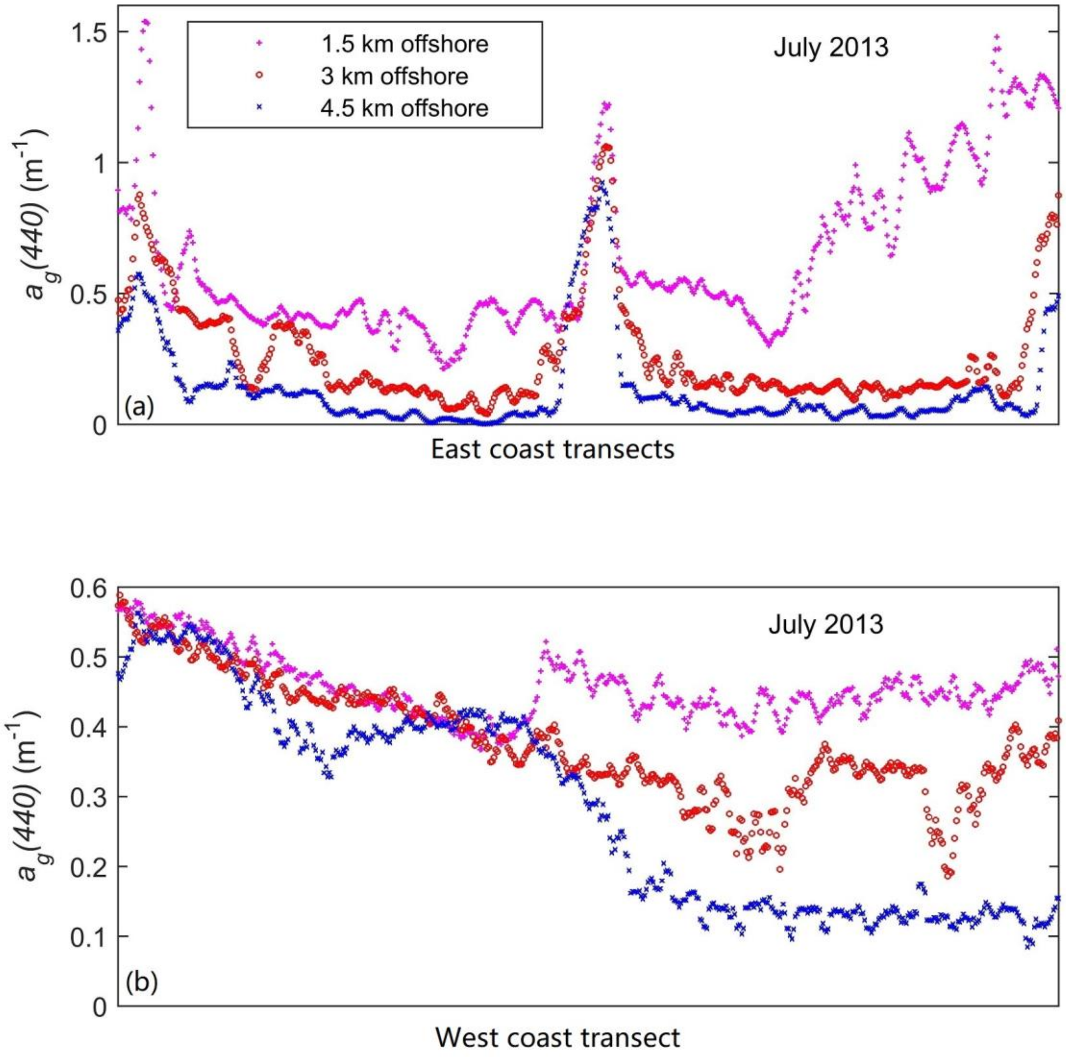

Figure 3-10: CDOM spatial dynamics in east coast regions and west coast regions. CDOM decreased 1 - 2 times in the distance of 5 km from nearshore regions to inner Bay regions.

CDOM spatial patterns derived from satellite images suggested that CDOM in the lake waters is significantly affected by terrestrial CDOM input via the Saginaw River. As the elevated CDOM levels associated with the discharge plume of the Saginaw River indicates, allochthonous CDOM from terrestrial sources is an important CDOM source for lakes (Kelly et al. 2014; Kritzberg et al. 2004). Often, the major allochthonous CDOM source originates from watershed soil carbon leaching and its subsequent transport to the aquatic environment (Kalbitz et al. 2000b; Kindler et al. 2011; Major et al. 2010). Inland river systems provide the network for this transport of terrestrial CDOM to lakes and coastal ocean waters (Findlay et al. 2001). Similar as in Saginaw Bay, terrigenous CDOM was observed to be one or two magnitudes higher than the autochthonous carbon sources which had a high ratio of allochthonous to autochthonous DOM (Michalzik et al. 2001; Neff and Asner 2001). The allochthonous CDOM in the Saginaw River was almost two times higher than the CDOM in inner Bay region. The successful monitoring of CDOM spatial distribution using high spatial resolution remote sensing is significant in that it helps understand the mechanisms of how terrestrially derived CDOM modulates the lake water environment through land-water carbon cycling (Palmer et al. 2015; Toming et al. 2016).

3.4.3 Lake water CDOM spatial variations affected by the terrestrial environment

CDOM levels within aquatic ecosystems are significantly affected by the terrestrial sources of organic matter. To further analyze how terrestrial CDOM migrates to Saginaw Bay waters, we compared water CDOM levels in areas influenced by different landcover types. In Figure 3-11, one high CDOM concentration area was found along the north coast of Saginaw Bay; this was also visible in Figure 3-8a & Figure 3-8b. This area of elevated CDOM was associated with the Wigwam Bay State Wildlife Area, which is dominated by coastal marsh plant species (Burton et al. 2002; Uzarski et al. 2004). Figure 3-11 shows how significantly carbon associated with these coastal wetlands influences CDOM in the nearshore environment. The average CDOM absorption in the wetland influenced areas was 1.70 m^{-1} while the average of waters bordered by mixed agri-forest regions was 0.85 m^{-1}. Moreover, the results in Figure 3-7 and 3-9 showed the east coast of Saginaw Bay had relatively higher CDOM levels than the west coast. The east Bay shore had a higher percentage of agricultural farmland. However, the west Bay shore was dominated by mixed agriculture and forest. Another large wetland area along the shoreline of the Saginaw River is the Shiawassee National Wildlife Refuge (Figure 3-12). Similar to Saginaw Bay, river CDOM levels near the Shiawassee wetland region were significantly higher than surrounding regions.

To further explore how biogeography influences CDOM in aquatic ecosystems, mean CDOM levels along the east coast (predominantly agriculture), west coast (agri-forest mixed), Wigman Bay (wetland), Shiawassee wetlands (upstream Saginaw River) and Saginaw River plume regions were plotted (Figure 3-13). As outlined above, waters associated with coastal wetlands had the highest CDOM levels compared to that found in the agriculture and mixed agri-forest regions. The Shiawassee region had higher CDOM levels than that of Wigwam Bay, as might be expected due to the much larger size of the Shiawassee wetland area (Wigman = 3.64 km^2, Shiawassee = 40 km^2) and dilution of CDOM levels by Lake Huron. Lakes in the agricultural cropland regions had higher CDOM levels compare to the lakes in the mixed agri-forest regions. The highest CDOM levels were again associated with the Saginaw River plume which receives contributions from a wide variety of landcover types including wetlands and agricultural croplands.

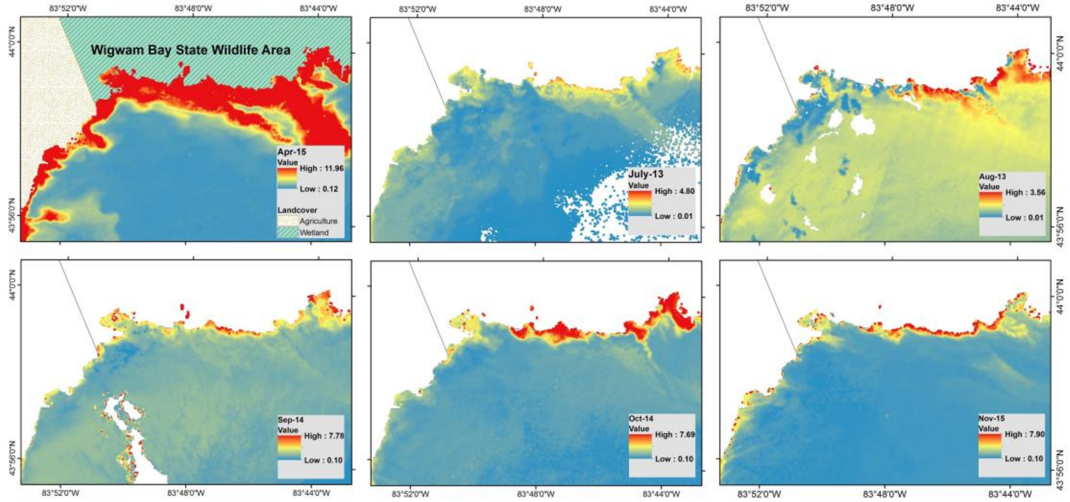

Figure 3-11: CDOM seasonal dynamics in six different months in the north coast of Saginaw Bay. CDOM had higher values in the wetland habit affected waters than that was affected by agriculture.

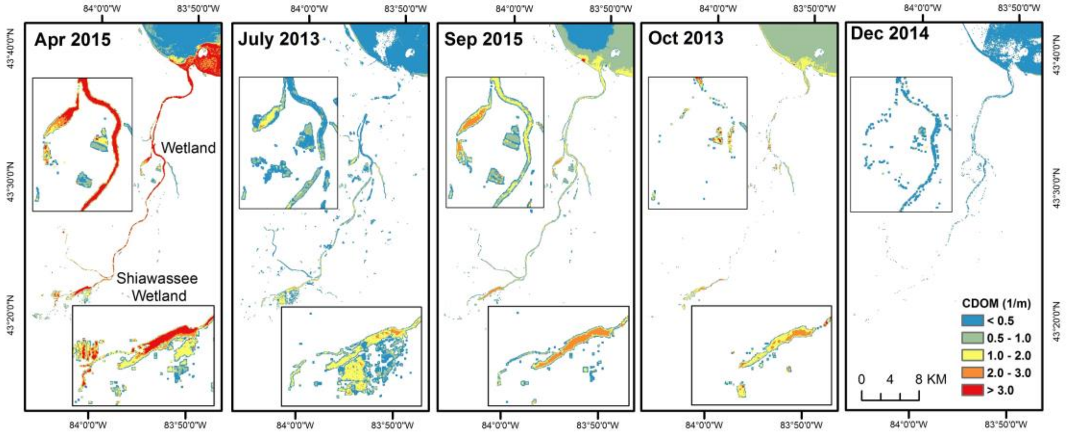

Figure 3-12: Comparision of CDOM associated with adjacent landcover types and seasonality in the Saginaw River region. Spring had higher CDOM than the other seasons.

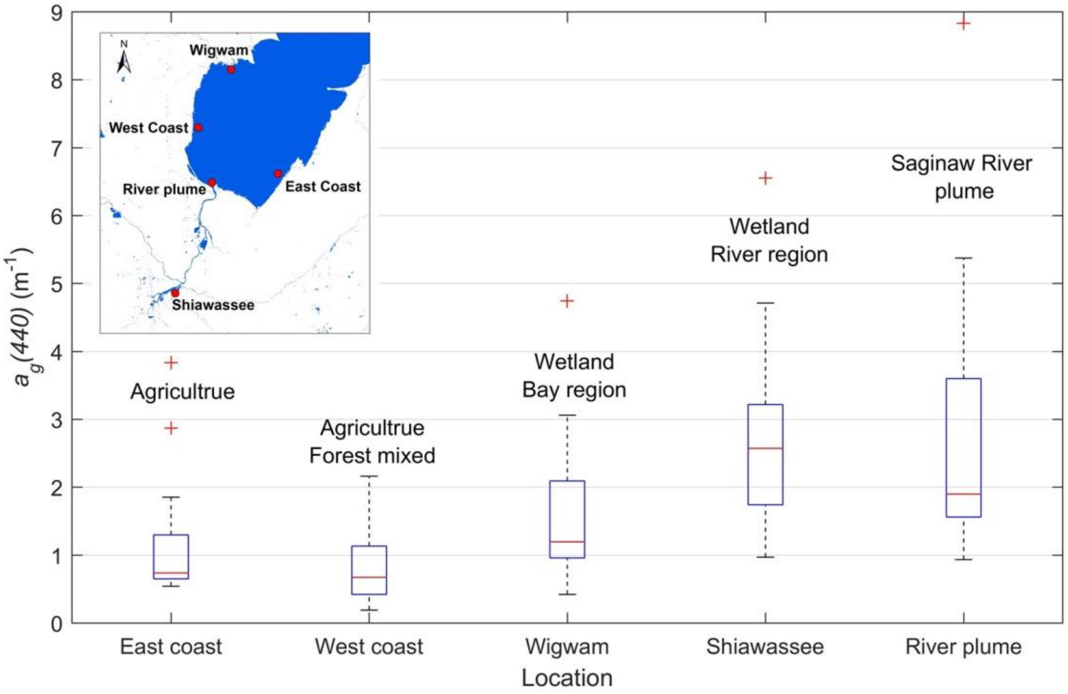

Figure 3-13: CDOM values calculated from ArcGIS zonal statistics in different landcover effects regions. Boxplot diagrams show the 75th, median and 25th percentile of mean CDOM associated with five different landcover types regions.

Our results indicate the Landsat-8 images is indeed applicable to the examination of the influence of biogeography on CDOM spatial variations. Previous studies confirmed the surrounding carbon sources from processes like plant material decay and soil carbon leaching contribute greatly to CDOM levels in river and lake environments (Boyle et al. 2009; Williams et al. 2010). Different landcover types play an important role in determining CDOM transportation from land to water (Butman and Raymond 2011). The lake CDOM levels in our studies showed the areas influenced by wetlands had the highest levels compared to the agricultural and mixed agri-forest regions across all seasons. The organic matter leached from persistent senescent wetland plant biomass was observed as an important CDOM source in the lake water in a previous study (Maie et al. 2006). Both the high density of wetland plants and their near water habitat contributed to the leaching of CDOM to the lake aquatic environment (Burton et al. 2002).

However, in the water regions receiving carbon from inland agriculture and forest, CDOM is routed through longer paths, and often CDOM concentrations are reduced via degradation and dilution. In the Saginaw Bay regions, our results indicated $a_g(440)$ were slightly higher in agricultural dominated regions than that in mixed agri-forest regions. One possible reason for the phenomenon in Saginaw Bay might because the crop residues remaining after harvest in agricultural fields supply more abundant biomass in the topsoil than that of forest in the Saginaw Bay regions (Boyer and Groffman 1996; Laudon et al. 2011). Also, microbial activity in agricultural fields has a higher rate, making higher levels of CDOM available for transport, leading to higher CDOM levels than forest soils (Anderson and Domsch 1975; Dominy and Haynes 2002). In all, CDOM spatial distribution is modulated by both landcover type and human land use practices, such as farming. The CDOM monitored via Landsat 8 could provide insightful information that helps improve our understanding of effects of land use practices and land management on the terrestrial carbon input to the lakes and rivers (Yallop and Clutterbuck 2009).

3.4.4 CDOM seasonal dynamics in the lake water environment

The path/row designation and associated dates for all processed Landsat-8 images of the Saginaw Bay (< 20% cloud coverage) were plotted in Figure 3-14a. These images spread well over time to monitor CDOM from March to the November. As discussed above, high levels of cloud coverage and ice coverage limit the derivation of CDOM in late fall through winter. The CDOM levels in the Saginaw Bay derived from satellite images showed clearly seasonal dynamics. For instance, the CDOM values were illustrated in five different months had different CDOM levels (Figure 3-12).

Figure 3-14b provides boxplot diagrams showing the 75th, median and 25th percentile of mean CDOM levels associated with different seasons. These mean CDOM values were derived in three different regions of Saginaw Bay through the ArcGIS zonal statistics for all the available CDOM results. Peak CDOM levels occurred in the spring associated with snowmelt and associated spring runoff (e.g., April 2015) and were two times higher than that of the other three seasons. This product coincides with the recently reported riverine CDOM dynamics in Michigan, particularly high spring CDOM fluxes, due to decomposition of agricultural residues and transport processes driven by snow melting (Tian et al., 2017). A secondary peak of CDOM level is evident in early fall and is associated with litterfall and the availability of crop residues on the landscape (e.g., September 2015, October 2013). The summer had the lower CDOM levels compared to the spring and fall (e.g., July 2013). Meanwhile, the winter months displayed the lowest CDOM values of the year. CDOM seasonal dynamics is related to the terrestrial CDOM supplies linked to seasonal changes to landcover and agricultural phenological cycles.

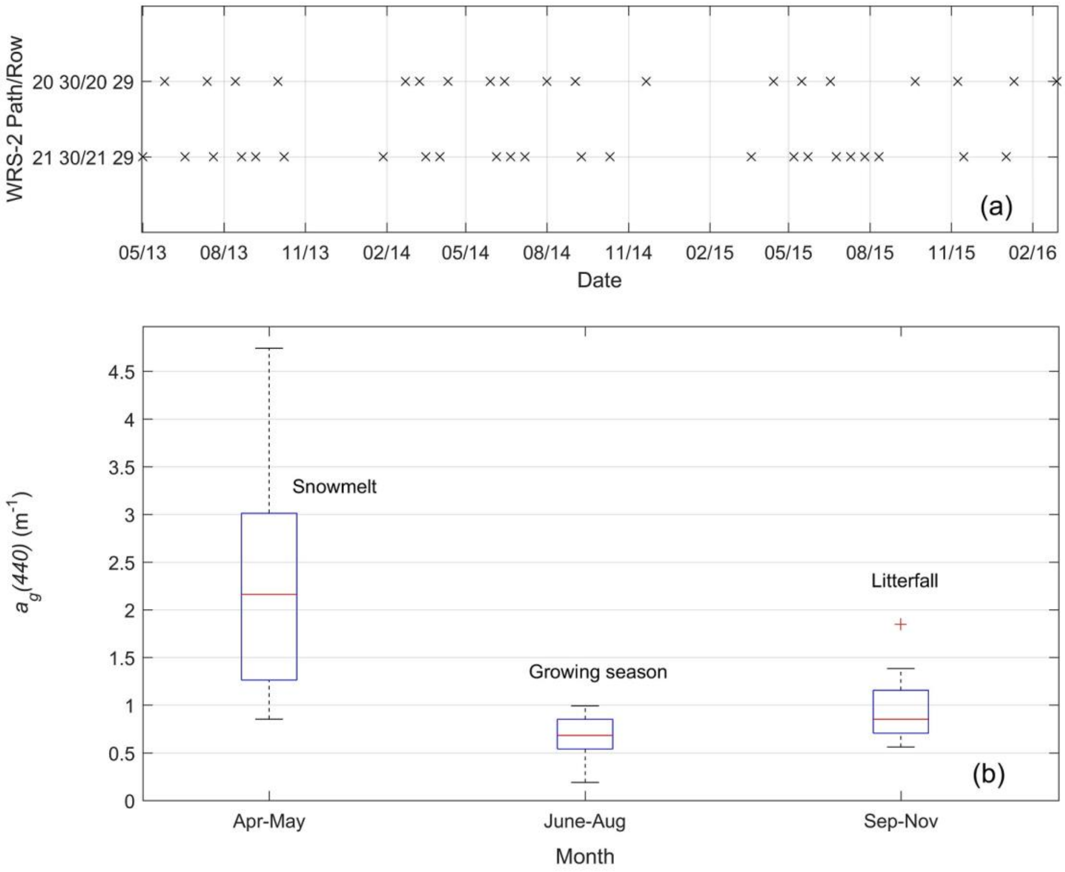

Figure 3-14: (a) The path/row designation and associated dates for all available Landsat-8 images of Saginaw Bay study area with cloud coverage less than 20% from 2013 to 2016. (b) Boxplot draws the 75th, median and 25th percentile of CDOM across three seasons.

To further explore CDOM dynamics associated with the Saginaw River, CDOM levels in Saginaw River mouth were compared with its discharge volume (Figure 3-15). The comparison aims to investigate the effect of hydrology to further explain the seasonal dynamics of terrestrial CDOM export to Saginaw Bay. As one might expect, Figure 3-15 illustrates that CDOM levels were positively correlated to river discharge throughout the seasons. Large amounts of CDOM were exported from the land (allochthonous) to the river as the channel gathered runoff from watershed during periods of high discharge (Figure 3-15). The highest riverine CDOM value shown in

Figure 3-15 occurred in April 2013, the highest discharge across the four year period shown. Similarly, field observations by others link periods of high discharge to relatively elevated CDOM levels (Battin et al. 2008; Evans et al. 2005; Hornberger et al. 1994). The highest relative river discharges occurred in the spring (Apr 2013, Apr 2014, March 2015 and Apr 2015). Snowmelt in combination with elevated precipitation leads to the high river discharge in spring (Ågren et al. 2010). Moreover, during winter months, leaf litters and agricultural residues slowly decay and leach into the soil carbon reservoir. When snowmelt occurs, large amounts of soil carbon are mobilized and are finally exported to the aquatic ecosystem (Haei et al. 2010; Qiao et al. 2017). All these reasons lead to the highest water CDOM in the spring. During the fall, the breakdown of fresh litterfall would cause relatively high soil carbon levels (Kalbitz and Kaiser 2008). These new carbon sources result in elevated CDOM in the fall (Oct 2013, Oct 2014 and Nov 2015).

Interestingly, an anomaly occurred during the winter of 2015, for its CDOM levels were elevated compared to other winters shown. This pattern was likely caused by historically warm winter temperatures in 2015, leading to both the Saginaw River and Saginaw Bay being ice-free for an abnormally long period. We assume that an unfrozen river and watershed acts as a better conduit for CDOM (Jan 2016) than what is typically expected during winter months. The river systems could more effectively transport the terrestrial CDOM to Saginaw Bay. Our CDOM absorption derived from the satellite images illustrates that land-water carbon exchange was significantly affected by the hydrology.

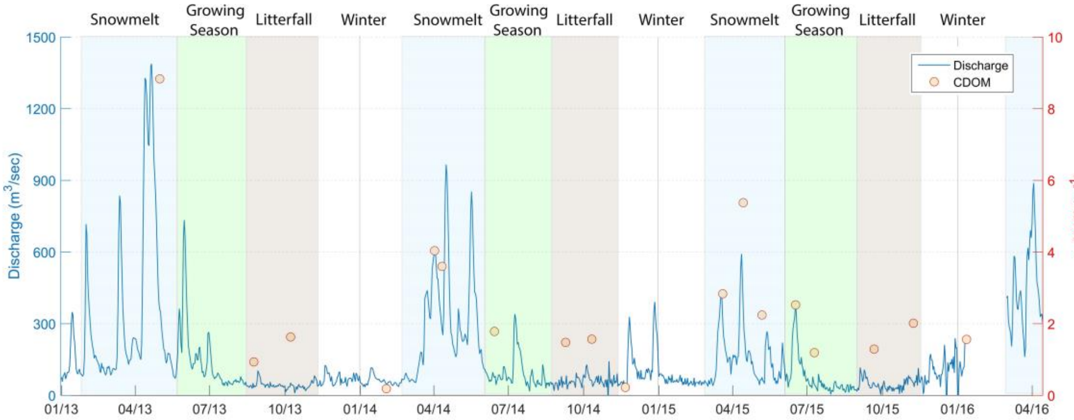

Figure 3-15: Landsat image CDOM absorption versus discharge at the Saginaw River mouth from January 2013 to April 2016.

3.4.5 CDOM spatial and temporal dynamics in the NE lakes

A similar analysis of CDOM spatial patterns was performed on 14 northeastern lakes and the Great Bay estuary complex across the diverse landscapes in which they reside (Figure 3-16). Like Saginaw Bay, CDOM spatial distributions across the northeastern region were highly affected by the terrestrial biogeography. In Lake Champlain, several Bay regions (Missisquoi Bay, Saint Albans Bay, Malletts Bay and South Bay) and Richelieu River plume region had relatively high CDOM levels than their inner lake regions (Figure 3-17). In general, CDOM absorption was highest in the northern regions of Lake Champlain, an area associated with a large zone of agricultural along this coastline. Similarly, the southern New Hampshire lakes (Baxter Lake, Swains Lake, Northwood Lake and Brindle Lake) had much higher CDOM absorption than the northern New Hampshire lakes (Lake Winnipesaukee, Newfound Lake, Webster Lake, Pleasant Lake and Sunapee Lake). This trend was attributed to the high proportions of agricultural farmland in Southern New Hampshire, which provide transportable carbon across the landscape.

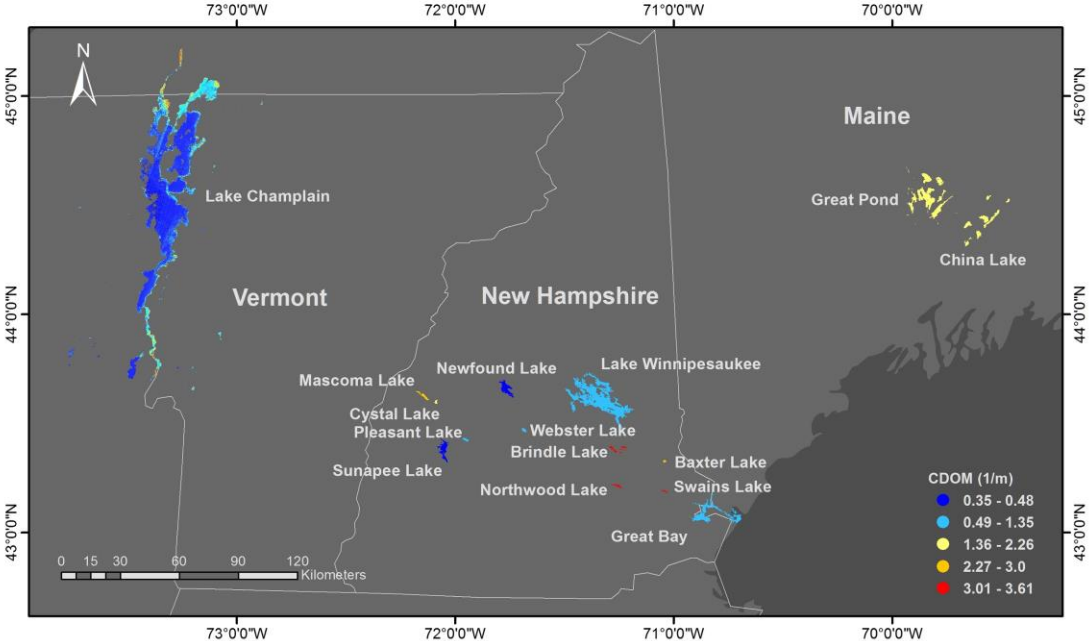

Figure 3-16: CDOM levels in 14 northeastern USA lakes and Great Bay estuary complex. Note that Lake Champlain was color displayed with derived CDOM absorption from a single image of Sep 2014. All other smaller lakes display their average CDOM levels derived from August 2014-15 or September 2014-15.

The data associated with the northeastern freshwater lakes and Great Bay estuary complex were also processed to further investigate the seasonal dynamics of waterbody CDOM and the transferability of the SBOP algorithm from region to region. We found that CDOM levels followed similar seasonal patterns as in Saginaw Bay/Lake Huron (Figure 3-17). As these images of Lake Champlain illustrate, CDOM levels were lowest in the summer months (Jun 2016) than in the spring (May 2014) and fall (Sep 2014). Similar patterns were observed for the Great Bay estuary complex (Figure 3-18). Analogous to the trends shown in Saginaw Bay, CDOM absorption was lowest in the summer (July 2015, Aug 2015) and elevated in the spring (Apr 2015) and fall (Oct 2014, Nov 2015). Just as in the Saginaw Bay region, CDOM released from the fresh autumn leaf litters, and agricultural residues were transported into the lakes and estuary, influencing elevated CDOM levels. Also, snowmelt in the spring would transport relatively large amounts of soil originated CDOM into the aquatic environment. Similar patterns across all of the data presented illustrate that the methodology presented can indeed be applied in different ecoregions and that inland waterbody are highly affected by the seasonal CDOM variations.

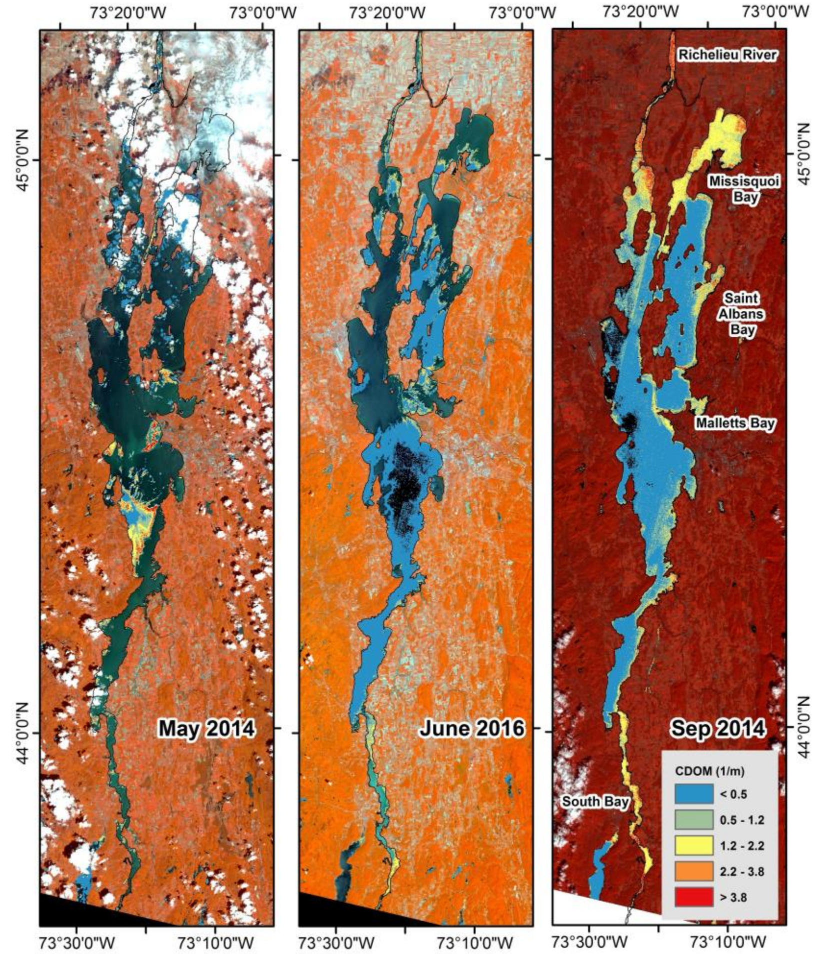

Figure 3-17: CDOM absorption of Lake Champlain across three different seasons. The Bay regions and Richelieu River plume region had higher CDOM absorption than inner Lake.

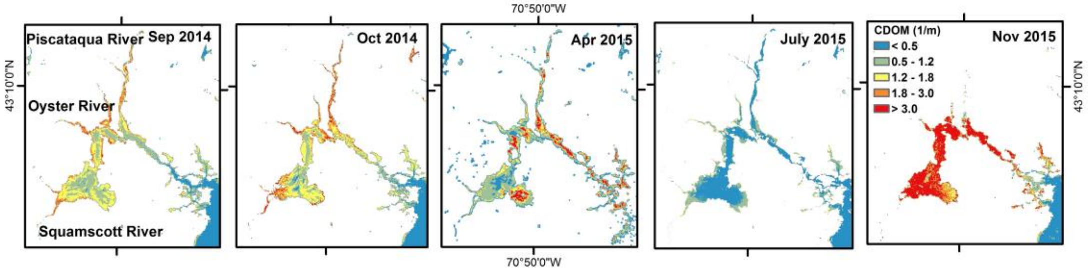

Figure 3-18: CDOM seasonal dynamics in the Great Bay estuary complex and surrounding rivers.

3.5 Conclusions

This study presented an application of a new semi-analytical algorithm, previously validated with field spectroradiometer data, to Landsat-8 OLI imagery for improving CDOM retrieval in optically shallow inland waters with relatively homogenous bottom sediment. The investigation was supported with sufficient satellite images and *in situ* field measurements collected over varying seasons across multiple years from a broad range of lake and estuary ecosystems. Our research achievements include:

1) Improved CDOM estimation accuracies for optically shallow waters via the SBOP algorithm benchmarked against an algorithm not considering of bottom reflectance. Separating bottom reflectance from other radiance pathways in the SBOP algorithm improved the estimation of CDOM for inland optically shallow waters.

2) The CDOM estimation algorithm was robust and consistent across a broad range and varied sizes of freshwater ecosystems and the Great Bay estuary complex. The results validation highlighted the transferability and scalability of our methodology. The extensive validation convinced that the algorithm is proficient in adapting to a broad range of aquatic environment.

3) Landsat-8 OLI imagery provides sufficient spatial (30 m), spectral (i.e., 443 nm, 482 nm, 561 nm, and 654 nm) and radiometric resolution required for retrieving CDOM levels for both optical shallow and deep inland waters. It enables high spatial resolution mapping of CDOM gradient from lower reaches of a river, shoreline, to open water. Consequently, monitoring the allochthonous CDOM transportation from terrestrial to aquatic ecosystems will improve our understanding of land-water carbon cycles.

4) Examination of CDOM seasonal variation coupled with terrestrial biogeography and related hydrology has great potential to help improve our understanding of aquatic ecology and land-water carbon cycle dynamics. CDOM spatial distribution and loading at the land-water interface is found coupling with the type and abundance of the terrestrial plant sources in the adjacent ecosystem. Moreover, the CDOM temporal variation correlated well to the river hydrographs for spring, summer, and fall. This conclusion is encouraging to study to what extent upland hydrology can influence the CDOM loading from land to water.

CHAPTER 4

RIVERINE CDOM DYNAMICS REMOTE SENSING ESTIMATION IN SIX LARGE ARCTIC RIVERS

4.1 Abstract

Terrestrially derived CDOM export to the Arctic Ocean is impacted by the global environmental change. This CDOM transport also had important effects on the carbon exchange at the land-water interface of Arctic regions. Previous monitoring of CDOM in the remote regions relied on the field samplings which was limited by both the temporal frequency and the spatial coverage. Using satellite remote sensing to estimate CDOM in the Arctic rivers provides an efficient approach for studying the CDOM transport from land to the Arctic Ocean. Exports of CDOM to the Arctic Ocean through six Arctic Rivers (Kolyma, Lena, Mackenzie, Ob', Yenisey and Yukon) were derived from 2013 to 2016 based on the satellite image derived results. Satellite-derived CDOM levels were at high accuracy ($RMSE$ = 0.10 and R^2 = 0.87) in the large Arctic rivers. We found that the input of terrestrially derived CDOM to the Arctic Ocean was significantly dominated by the river discharge. We discovered the changing of landcover types, temperature, precipitation, and changing of permafrost in Arctic regions would impact the riverine CDOM dynamics.

4.2 Introduction

The arctic environment has been greatly impacted by the recent global climate change (Schuur and Abbott 2011). The air temperature increasing rate in the pan-arctic regions is almost two times higher than the global mean value (Screen and Simmonds 2010). If we focus on the temperature increasing rate in the Alaska region, we could find the annual mean air temperature has increased by 0.29 °C during the last decade (Romanovsky et al. 2007). Along with the rising temperature, River discharge of the Arctic Rivers had increased in the past century (McClelland et al. 2006). Previous studies had revealed that in the 2000s, total riverine freshwater discharge had increased by 128 km^3/year (7%) compared the 1950s (Peterson et al. 2002). Meanwhile, the global river discharge studies also suggested that the Arctic rivers had the world highest discharge rate than the other global regions (McClelland et al. 2012; Milliman et al. 2008). A large quantity of freshwater was transported through the Arctic rivers to the Arctic Ocean. This increase of river discharge was thought to be contributed by multiple changing environmental factors, like the global warming, decrease of the snow cover in the Pan-Arctic regions, landcover change in the arctic terrestrial environment, and permafrost degradation (Kicklighter et al. 2013). Under these multiple changes, both the models and field observations suggested that the Arctic is becoming warmer and wetter in the future (McClelland et al. 2004; Nohara et al. 2006; Rawlins et al. 2010; Wu et al. 2005). All these environment changes would lead to the change of terrestrially derived CDOM export to the Arctic Ocean through the Arctic river systems (Schuur et al. 2008).

CDOM in the Arctic rivers systems could be applied as one indicator to trace the terrestrial DOC input from land to the Arctic Ocean. The previous study confirmed that a substantial amount of organic carbon in the higher latitude was stored in the soils and peatlands (Raymond et al. 2007). This large amount of soil carbon storage accounted nearly half of the global soil carbon (Zhulidov 1997). Furthermore, over 80 percentages of the soil carbon were thought to store in the permafrost soils (Tarnocai et al. 2009). Therefore, both the warming weather and increasing discharge raised the concerns of soil-stored carbon input to the Arctic Ocean (Holmes et al. 2008). The large Arctic Rivers would play a significant role in altering the carbon cycle by transporting this terrestrial carbon from land to the Arctic Ocean (Mann et al. 2017). Arctic Rivers almost account for more than 10% percentages of freshwater discharge globally (Raymond et al. 2008). And the Arctic Ocean also received more than 10 percent of the terrestrial DOC delivery to the global oceans within only 1 percent of global ocean volume (Stein and Macdonald 2004). The DOC loading to the Arctic Ocean was thought higher than all the other global ocean basins (Cooper et al. 2005). Specifically, six major Arctic Rivers account for the majority of both freshwater and terrestrial carbon inputs to the Arctic Ocean, so more attentions have been attracted to study the large Arctic Rivers.

Riverine CDOM input to the Arctic Ocean also had multiple effects on the physical, biology and chemistry environment conditions (Arrigo and van Dijken 2015; Fichot et al. 2013; Matsuoka et al. 2015). CDOM was the photoactive portions of DOM, and it had strong absorption at ultraviolet and blue bands. The increase of terrestrially derived CDOM input to the Arctic Ocean would affect the water optical depth in the Arctic shelf regions (Stedmon et al. 2011). Both phytoplankton and seagrass in the benthic would be affected by the change of the underwater light field (Larkum and Wood 1993). Serving at the important organic sources, increasing supply of CDOM to the Arctic Ocean would impact the primary productivity in the regions, particularly phytoplankton biomass (Thingstad et al. 2008). Moreover, the change of the underwater light field would lead to the change of the heat budget at the Arctic coastal waters (Granskog et al. 2007). High CDOM in the coastal waters would lead to strong absorption of solar energy in the Arctic surface waters. In summary, riverine CDOM estimation in the Pan-Arctic regions had significant implications to the Arctic terrestrial-aquatic environments.

Terrestrially derived CDOM input to Arctic Rivers need to be monitored at high spatial and temporal resolutions for offering supportive information for the carbon cycle, biogeochemical cycle and ecological processes studies. Previous studies in the Arctic Rivers largely relied on the field sampling to measure the water conditions Due to the accessibility challenge in the Arctic regions, data were also very limited in terms of spatial coverage and temporal frequency. Therefore, remote sensing technology provides large potentials for studying the CDOM spatial-temporal dynamics. However, there were no comprehensive studies to derive CDOM information in the Arctic Rivers based on satellite images. In this chapter, I applied the new Shallow water Bio-optical Properties algorithm (SBOP in chapter 2) and high-resolution satellite images (Landsat-8 CDOM estimation approach in chapter 3) to retrieve the CDOM spatial-temporal dynamics in six major Arctic rivers. All the available Landsat-8 images from 2013 to 2016 covering the river mouth regions were processed. Multiple environmental and landscape factors of their watersheds were investigated to infer their association to CDOM loading.

4.3 Method

4.3.1 Study sites

Six large Arctic Rivers in the Pan-arctic regions were selected as study sites, i.e., Lena, Mackenzie, Kolyma, Ob’, Yenisey and Yukon Rivers (Figure 4-1, Table 4-1). The Lena river located from mid-latitudes to the Arctic Ocean (Yang et al. 2002). Almost 15% of the freshwater discharged to the Arctic Ocean were contributed by the Lena River (Peterson et al. 2002). Major part of the watershed were underlined by permafrost (Boike et al. 2013). Mackenzie river had the longest length in Canada, and it has the second largest watershed area in North America (Aziz and Burn 2006). The majority watershed regions of Mackenzie river were underlined by discontinuous and continuous permafrost. Kolyma rivers located in the northeastern Siberia (Mann et al. 2012). The watershed of Kolyma River is completely underlined by the permafrost. Ob’ river is in the western Siberia (Biancamaria et al. 2009). It had lower permafrost compared to other large Arctic Rivers in Siberia. Yenisey river is in the center of Siberia. The Yenisey River is one of the largest river systems which are discharged to the Arctic Ocean (Melnikov et al. 2003). Nearly half of the watershed were coved by permafrost (Yang et al. 2004). Yukon River is a major river in North America. More than half of the watershed was the discontinuous and continuous permafrost (Spencer et al. 2008).

Multiple datasets were gathered in Arctic rivers to study the CDOM dynamics. The field sampling CDOM absorption and river daily discharge are obtained from Arctic Great Rivers Observatory project (Holmes et al. 2015; Mann et al. 2016). Landsat-8 satellite images are downloaded from USGS earth explorer website. Both mean surface temperature and mean precipitation are from University of Delaware Air Temperature & Precipitation v4.01 dataset (Willmott 2000). Permafrost coverage data are downloaded from National Snow & Ice Data Center (Brown et al. 2002). At last, landcover data are generated by Global Land Cover Facility (Friedl et al. 2010).

Table 4-1: Parameters for the major Arctic Rivers

River	Length (km)	Watershed Area (km^2)
Lena	4,400	2,400,000
Mackenzie	1,700	1,800,000
Kolyma	2,100	650,000
Ob’	3,650	2,970,000
Yenisey	3,438	2,580,000
Yukon	3,190	850,000

Figure 4-1: Six large Arctic rivers, of this chapter.

4.3.2 CDOM estimation from satellite images

Landsat-8 satellite images were selected in this chapter to derive the CDOM dynamics in six Arctic Rivers. The relative high spatial resolution of 30 m ensured the large Arctic rivers could be detected from the satellite images. In this chapter, all the available Landsat-8 images for covering the field sampling sites (Artic-GRO project) were downloaded to derive the CDOM absorption. The locations of the field sampling sites in Arctic-GRO were plotted in Figure 4-1. From 2013 to 2016, a total of 120 Landsat-8 images were acquired for processing. CDOM retrieval consists of the following steps: 1) atmospheric correction for water region, 2) water extent derivation based on NDWI (Normalized Difference Water Index), 3) interpolation of SBOP required remote sensing reflectance bands, and 4) SBOP algorithm processing (Figure 4-2). The details of the satellite processing and SBOP algorithm were described in previous two chapters

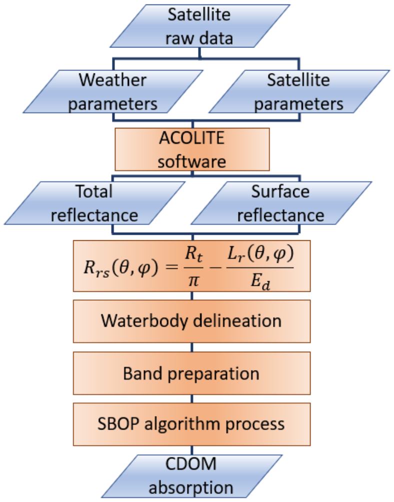

Figure 4-2: The processing flow of CDOM estimation based on Landsat-8 satellite images, mainly including atmospheric correction, water body identification, and SBOP algorithm processing.

4.4 Results and Discussions

4.4.1 CDOM satellite estimation validation across Pan-Arctic Rivers

CDOM absorption derived from Landsat-8 satellite images were validatd with ground-truth data collected by the Arctic-GRO project. Total of 13 satellite images were selected to compare with the field measures. The selected images were in July 2013 for the Lena River, in June 2013 and June 2014 for the Mackenzie River, in May 2013 and August 2014 for the Ob' river, in May 2013, July 2013 and August 2014 for the Kolyma river, in September 2013 and June 2014 for the Yenisey River and in May 2013 and June 2013 for the Yukon River. The selection of satellite images was based on the smallest temporal gap between sampling date and satellite image acquisition date.

Figure 4-3 illustrated the comparisons between the satellite image derived CDOM absorption at 440 nm and field measured values. SBOP algorithm successfully derived the CDOM absorption at broad ranges of CDOM levels and spatial locations, from low CDOM absorption rivers (e.g., Kolyma river) to medium (e.g., Yukon river), and high CDOM absorption rivers (e.g., Lena river and Ob' river). Almost all the dots are near the 1:1 line in the Figure 4-3. Both R^2 and RSME demonstrated CDOM absorptions were estimated with high accuracy (R^2 = 0.87 and RSME = 0.10). Only one image derived at Ob' river site appears to significantly underestimate the CDOM. Overall performances of our method could ensure the solid CDOM absorption results for the analysis.

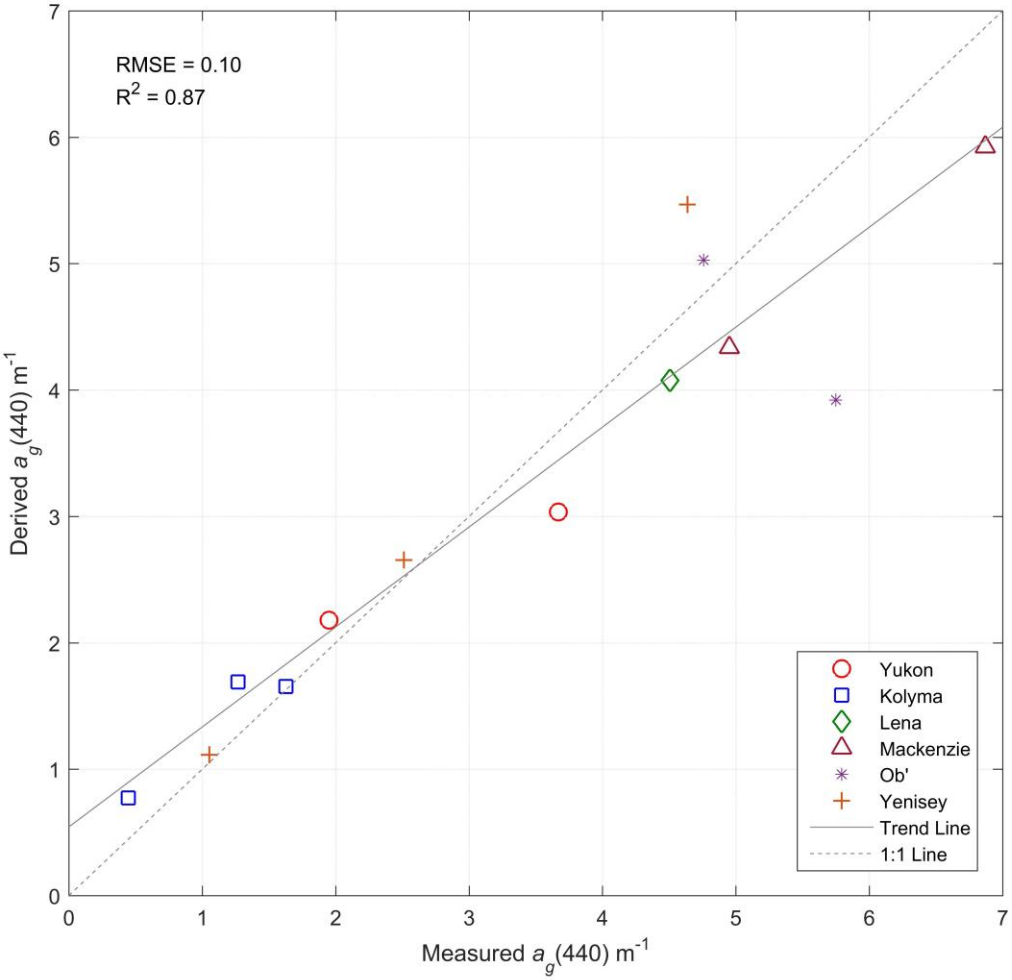

Figure 4-3: The results validation in six large Arctic Rivers.

4.4.2 CDOM spatial patterns in different Arctic rivers

CDOM spatial and temporal dynamics were derived from Landsat-8 satellite images. The high spatial resolution allows to capture the shape and extent of Arctic Rivers. Figure 4-4 showed spatial patterns of CDOM in six different Arctic rivers. In contrast to CDOM gradient observed at lower latitude rivers, CDOM levels are shown near constant and homogeneous patterns. High CDOM concentrated in the mainstream of the rivers for all rivers, much higher than the sub-stream. For instance, CDOM in the mainstream of Lena river was almost two times higher than substream. High CDOM were also observed in Yukon river’s wide mainstream, opposed to low in narrow tributaries. A large amount of terrestrial CDOM from upland watershed was delivered to the ocean through the mainstreams of the large rivers.

All the six Arctic rivers had relatively high CDOM absorption as illustrated; mostly higher than 2.0 m^{-1}. The highest CDOM (~ 5 m^{-1}) was showed in the Lena river. For all the six Arctic Rivers, CDOM absorption was estimated near the estuary regions. These regions locate close to the Arctic Ocean. Therefore, the satellite derived CDOM could represent the riverine CDOM input to the Arctic Ocean.

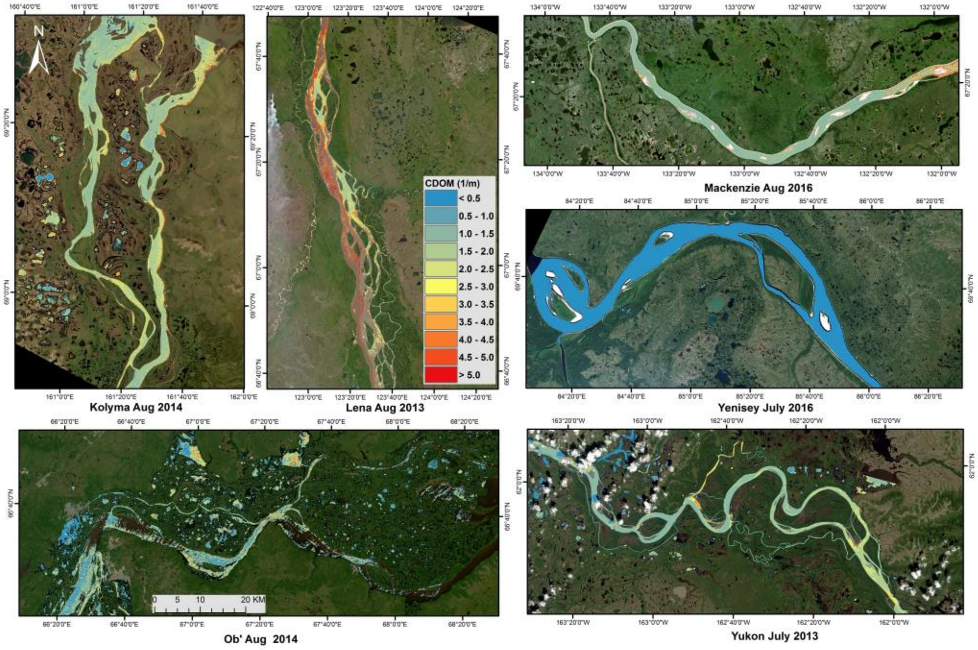

Figure 4-4: Spatial patterns of CDOM in six different Arctic rivers. Both the mainstream and tributaries were captured by the high spatial resolution of Landsat-8 images (30 m). CDOM absorption in the mainstreams of rivers had obviously higher value than tributaries.

CDOM information in Figure 4-4 was selected in late July or early August in different rivers. At the close time period, individual Arctic rivers showed different CDOM levels. High CDOM rivers were Lena, Ob' and Mackenzie rivers, and relatively low CDOM rivers were Kolyma and Yenisey rivers. These satellite-derived results were consistent with previous field studies (Amon et al. 2012; Holmes et al. 2012; Mann et al. 2016).

Boxplot of both field sampling data (from 2012 to 2014) and satellite image derived results (from 2013 to 2016) were plotted in Figure 4-5. Top of the box represents 25% percentiles of the CDOM values and bottom of the box represents 75% percentiles of the CDOM values. The red line in the middle represents the median values of CDOM. We found the extreme high CDOM absorption value was in Lena river with the values of ~11 m^{-1}. This CDOM value is nearly 3 m^{-1} higher than the other rivers' highest values. All the other rivers had the highest values around 7 m^{-1} to 7.5 m^{-1}. However, these abnormally CDOM peak values didn't frequently occur in the Arctic Rivers, especially in Kolyma and Yenisey rivers. Lena, Ob' and Mackenzie rivers had higher median values than the other rivers. Most of the CDOM values in these three rivers were higher than other Arctic rivers. Yukon and Yenisey were the second group in CDOM absorption. Kolyma river had lowest CDOM both in median values and total ranges of CDOM values. In summary, CDOM absorption at different Arctic rivers could be ranked as high CDOM group (Lena, Ob' and Mackenzie), medium CDOM group (Yukon and Yenisey) and low CDOM group (Kolyma) as shown by both satellite image derived and field measured results. Moreover, all the Arctic rivers had similar CDOM range between 25 to 75 percentile, about 3 m^{-1} to 5 m^{-1}. Six different Arctic rivers showed distinct patterns of CDOM absorption.

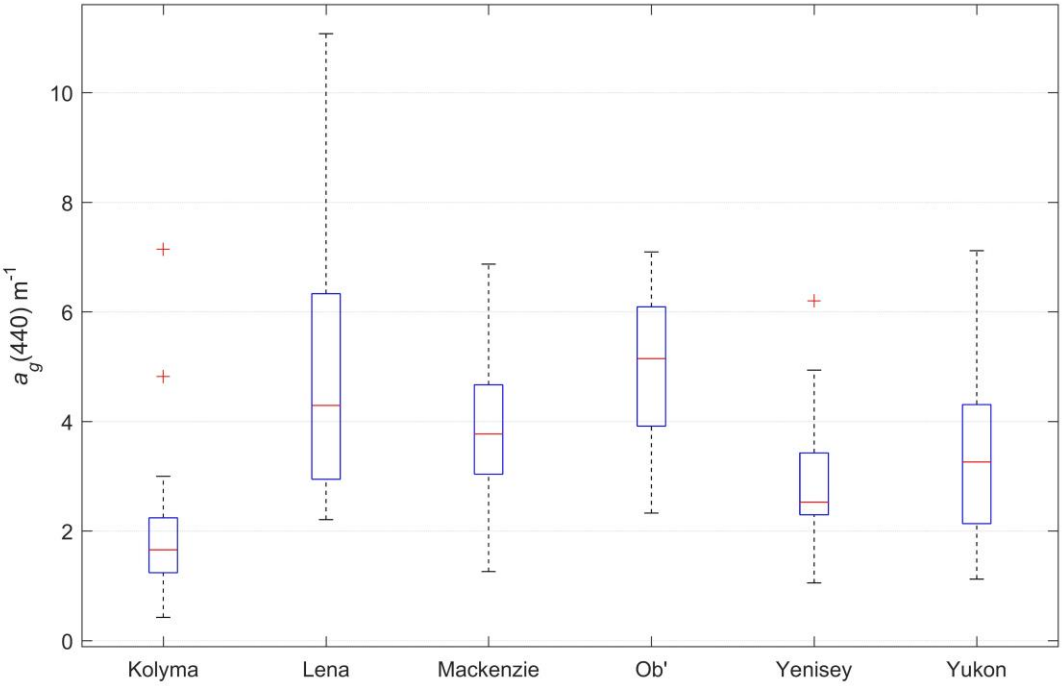

Figure 4-5: Box plots of six different Arctic rivers CDOM absorption at 440 nm. Both satellite images derived values and field measurement values were aggregated for a bigger sample size for comparison.

4.4.3 Seasonal dynamics of Arctic riverine CDOM absorption

CDOM seasonal dynamics derived from satellite images for six different Arctic rivers were illustrated from Figure 4-6 to Figure 4-11. The CDOM information was selected to show in different months with low cloud coverage. All CDOM peak values in individual Arctic rivers appeared in spring season (June). CDOM absorption in spring showed much higher values than all other seasons. For instance, for the Kolyma river in Figure 4-6, CDOM absorption in June was two times higher than May. It was 1.5 times higher than August. In Mackenzie river, high CDOM absorption in June had almost four times higher values than October. The similar CDOM seasonal patterns were also observed in Yukon river. Similar, The Ob' rivers showed highest CDOM values and widest river width in the spring season. All the CDOM absorption in Arctic river had highest values in spring season (Kicklighter et al. 2013). These annual high CDOM peak happened within the snowmelt (or ice break) in June of the Arctic rivers.

After the spring, the CDOM decreased to relatively constant levels in the summer season. For instance, in Kolyma river, CDOM had similar levels both in July and August. CDOM absorption in Yenisey river had constant values in Yukon river after the high peak in spring. During the summer season, with relatively constant hydrology and watershed environment, CDOM absorption in different Arctic rivers often didn't exhibit distinct variations. After the summer, several rivers had shown second CDOM peak in the fall. For instance, in Lena river, the CDOM absorption in late September had high values. These might be caused by the contribution of fresh leaf litters in the watersheds (Qiao et al. 2017). This high CDOM in the fall season was most notable in Lena river, because large portions of landcover were the forest with high leaf litters biomass (Amon et al. 2012). All the CDOM absorption decreased to the lowest values in late fall and winter (from October to April). Generally during the winter, the river freeze and high cloud conditions obstructed a frequent monitoring. We could still find that CDOM absorption in Mackenzie river had obviously lower values in October under partial freezing conditions (Figure 4-8). In the Yenisey river, the lowest values were also found in November where half of the river was frozen. All the riverine CDOM in large Arctic rivers had similar seasonal dynamics, i.e., peak values in spring and the lowest values in winter. Especially, high riverine CDOM in spring contributes the major CDOM delivery to the Arctic Ocean

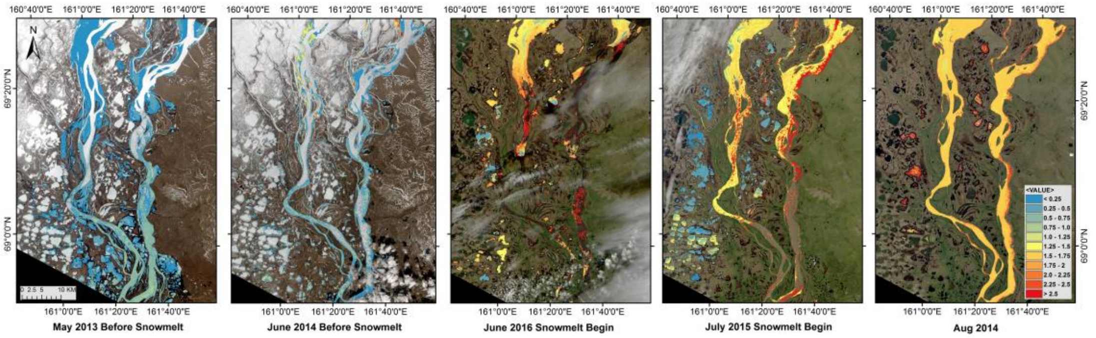
May 2013 Before Snowmelt
June 2014 Before Snowmelt
June 2016 Snowmelt Begin
July 2015 Snowmelt Begin
Aug 2014

Figure 4-6: CDOM absorption at Kolyma River in five different months. CDOM transport peak was in spring.

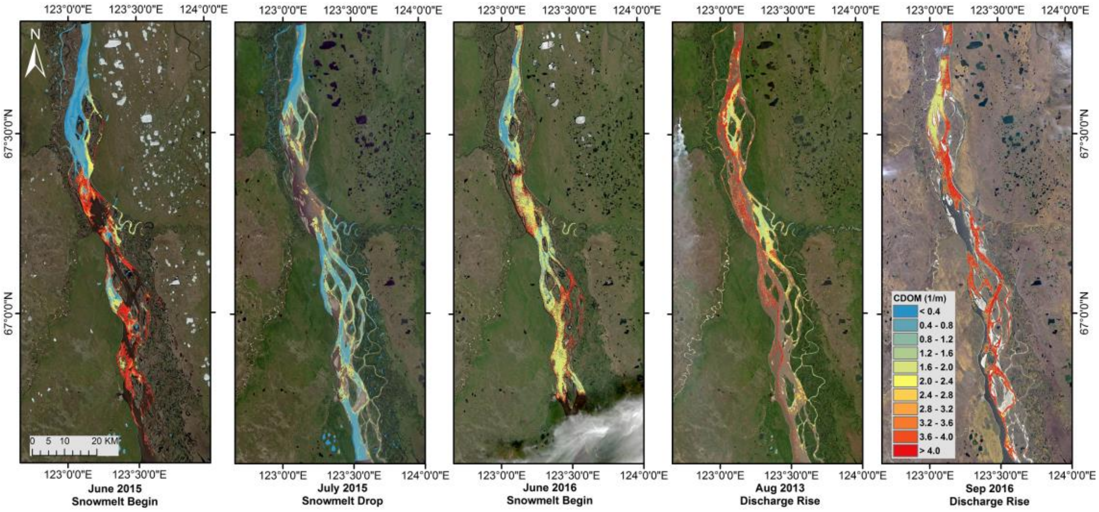
June 2015 Snowmelt Begin
July 2015 Snowmelt Drop
June 2016 Snowmelt Begin
Aug 2013 Discharge Rise
Sep 2016 Discharge Rise

Figure 4-7: CDOM absorption in Lena river in five different months. A large amount of terrestrial CDOM was carried through the mainstream of the Lena River.

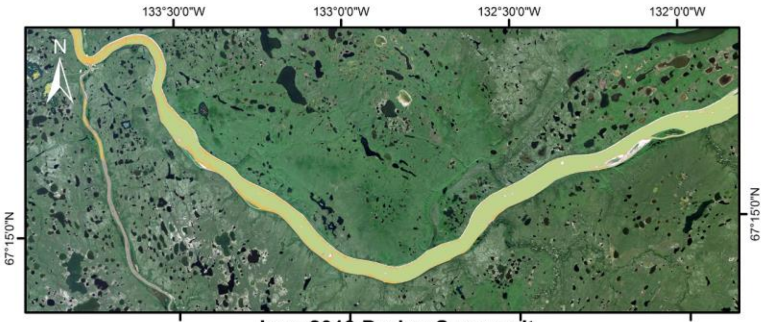

June 2013 During Snowmelt

June 2014 Snowmelt Begin

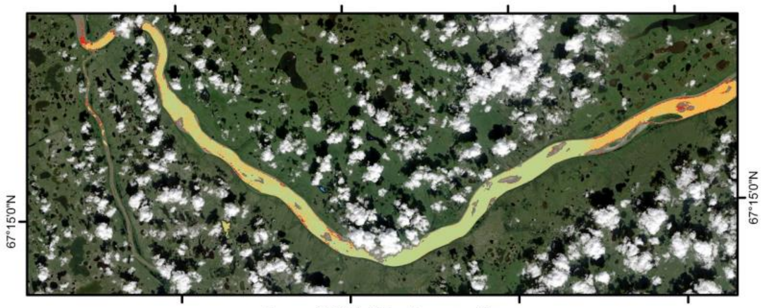

June 2014 Discharge Drop

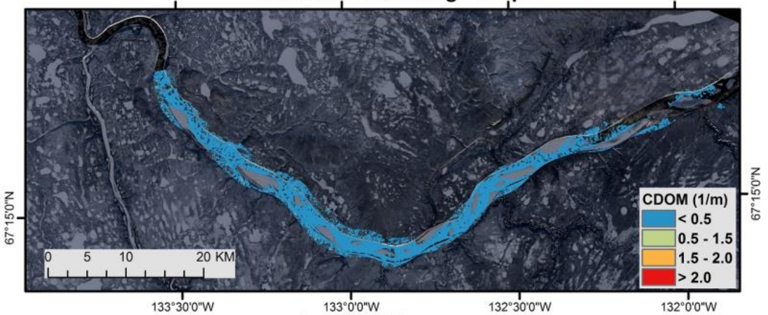

Oct 2014 Freeze

Figure 4-8: CDOM absorption in the Mackenzie River. The frozen condition in late fall significantly decreased the CDOM input to the Arctic Ocean through the river system.

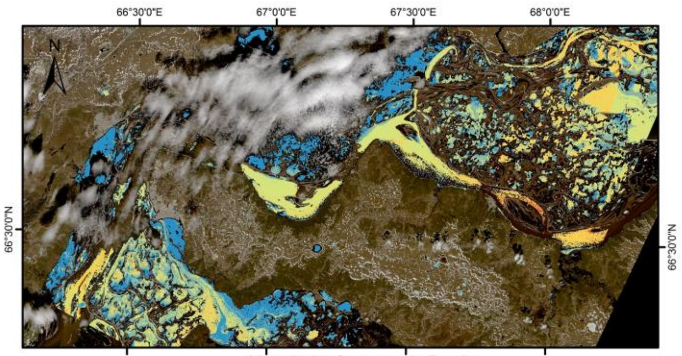

May 2015 Snowmelt Begin

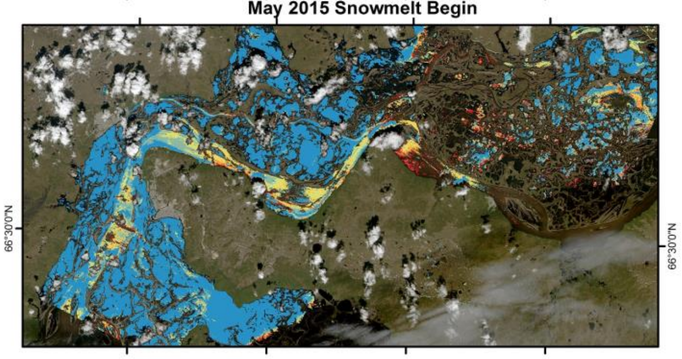

June 2015 During Snowmelt

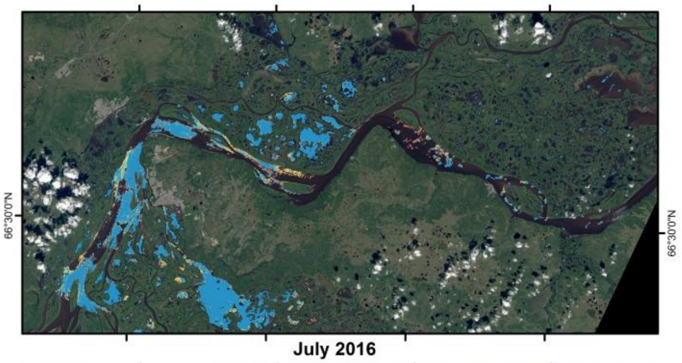

July 2016

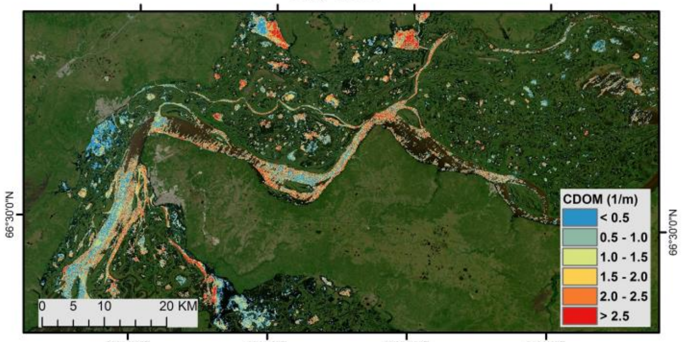

Aug 2014

Figure 4-9: CDOM absorption values in the Ob' River. The spring flood of the river would largely increase both the CDOM and freshwater input.

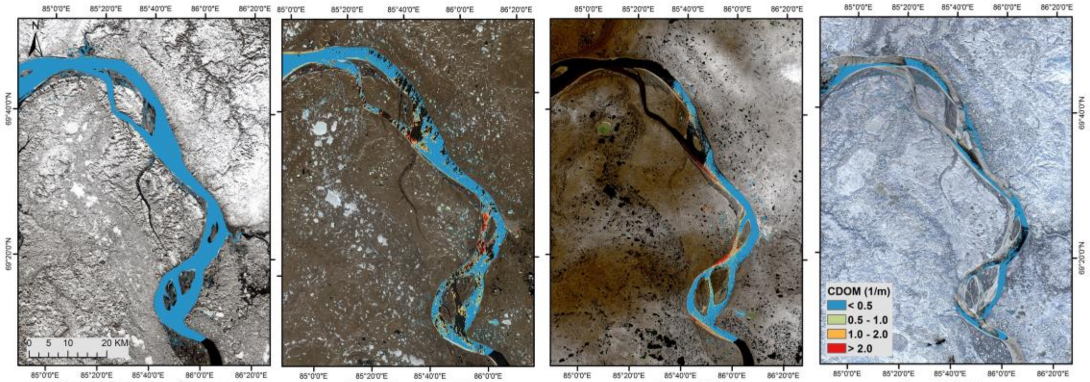

May 2015 Before Snowmelt
May 2013 Snowmelt Begin
Sep 2014
Nov 2016 Freeze

Figure 4-10: CDOM absorption in four months of Yenisey River. The Yenisey River had relatively low CDOM absorption comparing with other Arctic Rivers. However, it still transported a large quantity of CDOM due to its high river discharge.

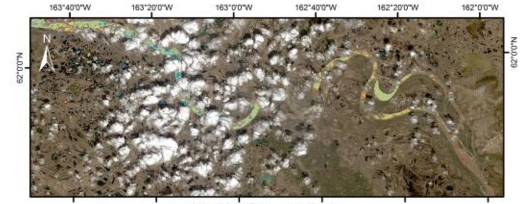

May 2014 Snowmelt Begin

June 2014 During Snowmelt

July 2014 After Snowmelt

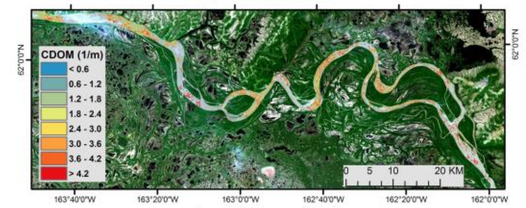

June 2015 Snowmelt Begin

Figure 4-11: CDOM absorption in four different months of Yukon River. CDOM in the Yukon River also showed obviously peak in snowmelt season.

4.4.4 River discharge controlling on CDOM input from land to the Arctic Ocean

CDOM seasonal dynamics are highly impacted by the river discharge in six Arctic rivers. All the CDOM levels from field sampling measurements and satellite image derived results were compared with daily discharge data in Figure 4-12. We found most of the Arctic riverine CDOM were positively related to the river discharge. High river discharge is associated to high CDOM in all the six rivers. For instance, the highest CDOM values were in the Lena river (10 - 11 m^{-1}). At the same time, it obtains highest discharge values (80,000 - 150,000 m^3/second) among with the Arctic rivers. The medium riverine CDOM river was the Mackenzie river with CDOM absorption ranging between 4 m^{-1} and 6 m^{-1} and discharge ranging between 20,000 and 40,000 m^3/second. Meanwhile, the Kolyma river had the lowest CDOM absorption of 0.5 m^{-1} and the lowest discharge less than 20,000 m^3/second in the pan-Arctic regions. By comparing across these rivers, we found the mean CDOM levels were ~2.5 times higher in high discharge rivers (Lena = 5.16 m^{-1}, Ob' Rivers = 5.05 m^{-1}) than low discharge river (Kolyma = 1.96 m^{-1}).

In addition to the ordinal rank, CDOM and discharge relationship follows a positive linear correlation at each river from the high discharge river (Lena, Yenisey) to the low discharger rivers (Kolyma). For instance, some high CDOM absorption values in Lena river were 3-4 times higher than the low CDOM one. Meanwhile, these high CDOM events also had nearly three times higher discharge rate than others. Although the CDOM absorption Kolyma river was much lower than the other rivers. The positive relationship between CDOM absorption and river discharge was also observed. In

Kolyma River, the high CDOM absorption (~ 1.5 m^{-1}) was related to the high river discharge (20,000 m^3/second). Other rivers (Yukon, Mackenzie, Ob' rivers) also showed similar relationship between CDOM and river discharge. Overall, the high river discharge leads to the high riverine CDOM. Moreover, the total CDOM flux transported by the Arctic rivers is determined by both concentration/level and river discharge. Ultimately, high discharge river would have dominated impact on the terrestrial CDOM input to the Arctic Ocean.

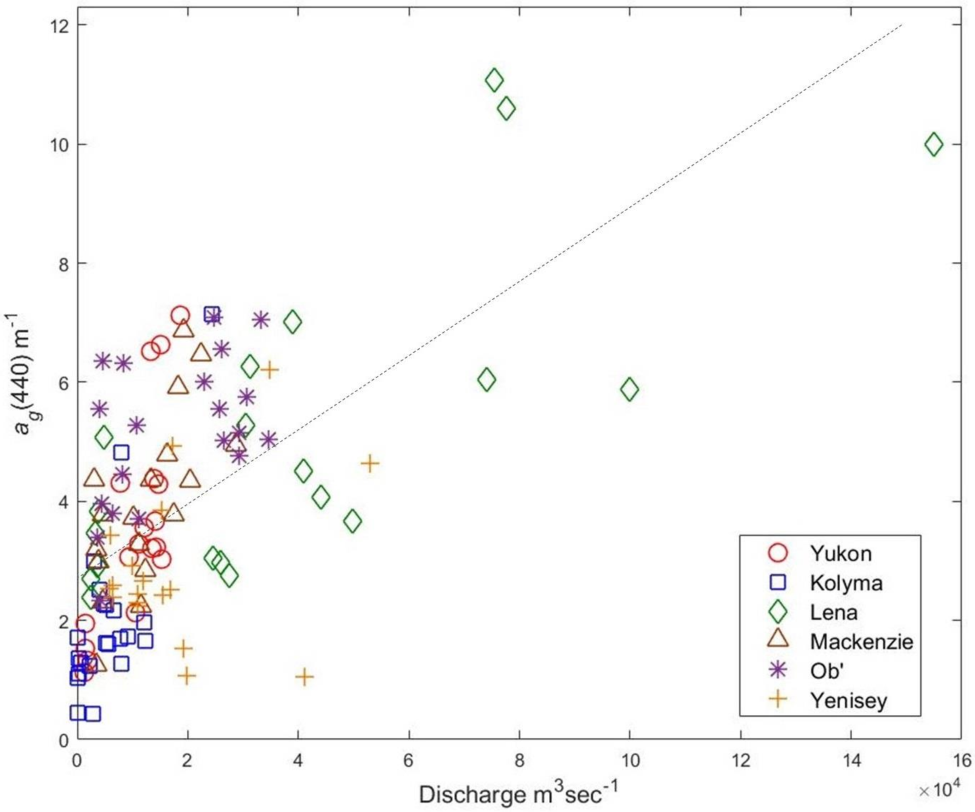

Figure 4-12: CDOM absorption versus river discharge in six large Arctic Rivers. High discharge values lead to the high CDOM absorption in the river waters.

CDOM absorption and daily river discharge data were compared in Figure 4-13 to analyze how riverine CDOM responds to high frequency river flow. First, one notable phenomenon is that all the rivers had much higher CDOM levels during the spring than all the other seasons. For instance, in Lena river, all the annual CDOM peak concentrated at the beginning of the ice-out spring season. Several high CDOM values were above 9 m^{-1}. In Kolyma river, all the obviously high CDOM values were in the high discharge spring season. Also, all the other large Arctic rivers showed a similar pattern that high riverine CDOM was carried during the snowmelt spring. This phenomenon reveals that the majority terrestrial CDOM was transported through the significant high river flow of snowmelt waters during a short period (Qiao et al. 2017). These results were consistent with the previous studies that almost 60% of terrestrial DOM were transported in spring in the Arctic regions (Raymond et al. 2007; Stedmon et al. 2011). During the snow and ice melt spring, the snowmelt water carried a large amount of terrestrial-derived CDOM to the rivers (Perdrial et al. 2014). This terrestrial derived CDOM included both annual new litter contributed DOM and soil storage DOM (Feng et al. 2013; Matsuoka et al. 2017; Yang et al. 2015). Moreover, the relatively high precipitation to the Arctic river watershed during the spring led to high leaching of soil DOM (Sinha et al. 2017).

Future projected temperature rise and discharge increase would enhance both CDOM and freshwater input to the Arctic Ocean (Bintanja and Selten 2014). This increase of CDOM input based on both ice-out water in spring and constant water transport in the other seasons. For the spring ice-out water, global increasing temperature and rising precipitation would lead to the increasing of snowmelt water (Wu et al. 2005). The increase of spring discharge would lead to significantly high CDOM input to the Arctic Ocean, especially for the high discharge dominated river like Lena river and Ob’ river. The increase of CDOM input would also be attributed to the constant river discharge rising in the other season. The previous study showed a large portion of discharge increase were contributed by the increase of daily discharge (Kurylyk et al. 2014; Smith et al. 2007). Increase of CDOM input would be specifically notable in Yenisey river which had relatively constant CDOM levels during the whole year (Figure 4-13). Along with its high discharge rate, the Yenisey river could obviously elevate its CDOM loading to coast with the future increasing discharge. Overall, this projected increase of freshwater CDOM will change Arctic environment through impacting of underwater light penetration, changing photochemistry to affect primary productivity, and altering carbon cycle at Arctic regions (Matsuoka et al. 2017; Stedmon et al. 2011).

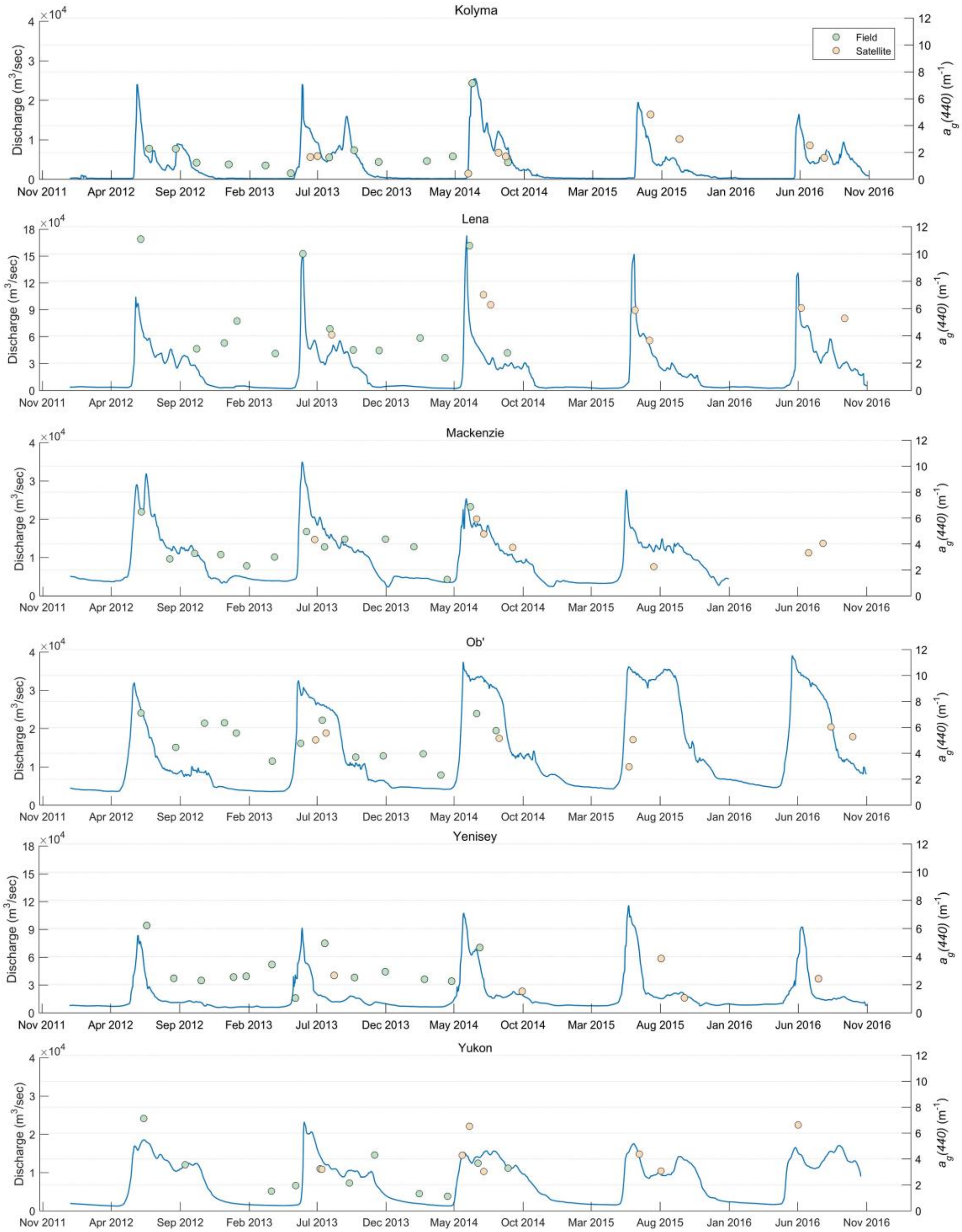

Figure 4-13: Daily river discharge values and CDOM absorption in the Arctic river waters. CDOM showed seasonal dynamics which is controlled by the river discharge.

4.4.5 Multiple environmental impact factors on Arctic riverine CDOM

Terrestrial derived CDOM accounts for large portion of riverine CDOM in Arctic Rivers (Walker et al. 2009). Multiple terrestrial environment factors affected the CDOM input from land to water through different ways. These terrestrial environmental factors could be landcover types, changing of permafrost soils, temperature, and precipitation. First, for the landcover types, the previous studies have proved that the decomposition of vegetation litters was important sources for the CDOM in the river systems (Spencer et al. 2009; Vodacek et al. 1997). Different landcover types in the watershed would contribute to the CDOM in the large Arctic rivers (Figure 4-14). For instances, the Kolyma river has the a major landcover type of shrub tundra which obviously lowers biomass as terrestrial DOM sources compared to forest and agriculture. Meanwhile, the Ob' river has high CDOM with the medium river discharge rate because of multiple terrestrial CDOM sources. These multiple sources were wetland, forest, and agriculture. The wetland landcover particularly contributes a large amount of CDOM to the waters (Chen and Jaffé 2014).

Studies had shown the dramatic landcover changes in the Pan-Arctic regions because of the rise of global temperature and decreasing of snow cover (Pearson et al. 2013). These change of landcover was represented as the change from the low biomass shrub tundra to the high biomass woody cover in the Pan-Arctic. We also found increase of forest landscape in the major Arctic river watersheds (e.g., Kolyma +4%, Mackenzie +8.76, Yenisey +3.4%) from the analysis of the MODIS landcover from 2004 to 2012. The future projected increase of forest landcover type in the Arctic regions would contribute to the rise of CDOM input from land to the Arctic Rivers. This increase of woody cover will contribute a large amount of litter biomass originated CDOM (Verstraeten et al. 2014).

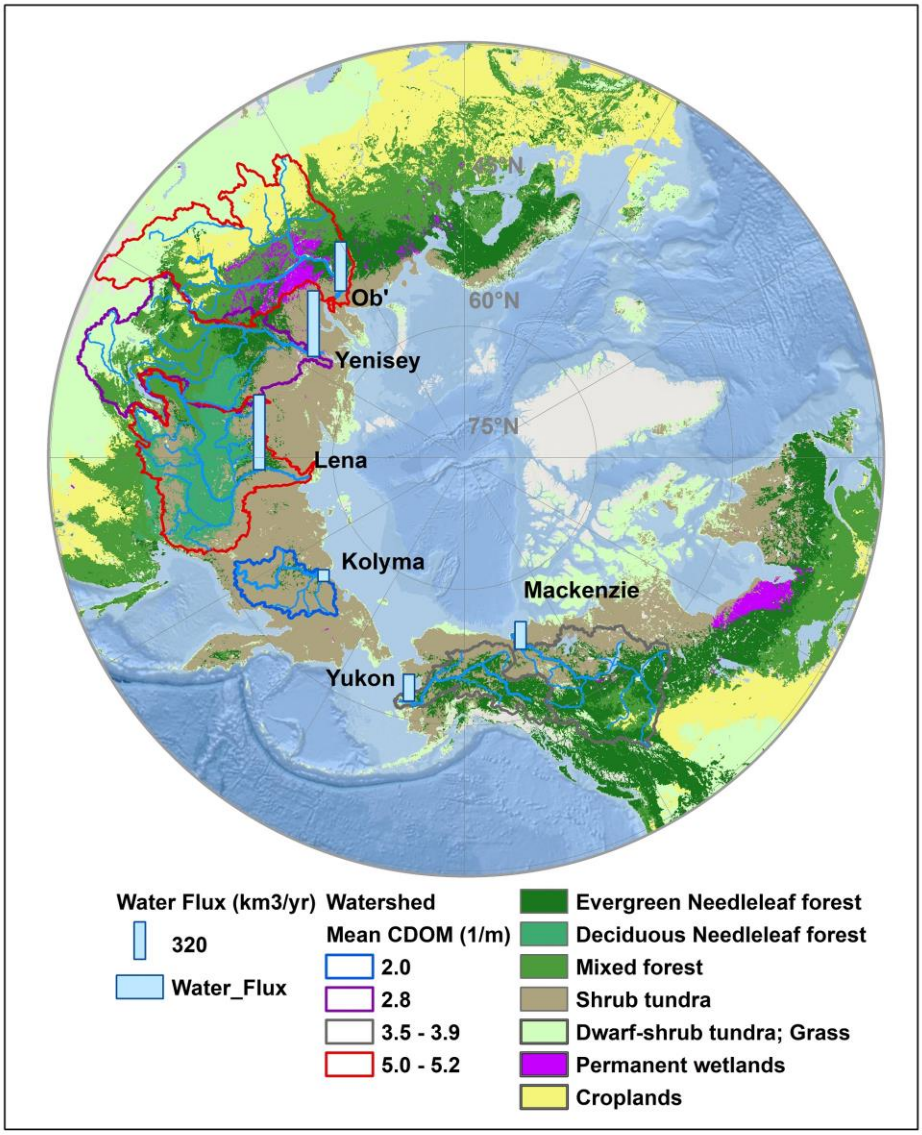

Figure 4-14: Mean riverine CDOM versus watershed landcovers. Forest landcover types contributed a higher amount of CDOM to the river systems than the shrub tundra landcover.

Precipitation was also an important factor on the terrestrial CDOM input to the Arctic Rivers. River discharge is highly associated with the precipitation. The river water was contributed by both the surface runoff and groundwater input. One important source of groundwater input was caused by the precipitation penetrating through the soil. Therefore, both the surface runoff and groundwater input would be accelerated by the precipitation (Stedmon et al. 2011). Meanwhile, the rainwater would carry the CDOM from vegetation and soil through the surface runoff and water penetrating. This phenomenon is most obviously seen in the watershed regions of Lena and Ob' rivers watershed (Figure 4-15). The higher precipitation in these two watersheds might be one of the reasons for high CDOM in the rivers. To the contrary, both the precipitation and CDOM in Kolyma river had lowest values comparing to other Arctic rivers. Moreover, the future projected global rising precipitation might further increase the terrestrial derived CDOM input to the Arctic Ocean (Sinha et al. 2017).

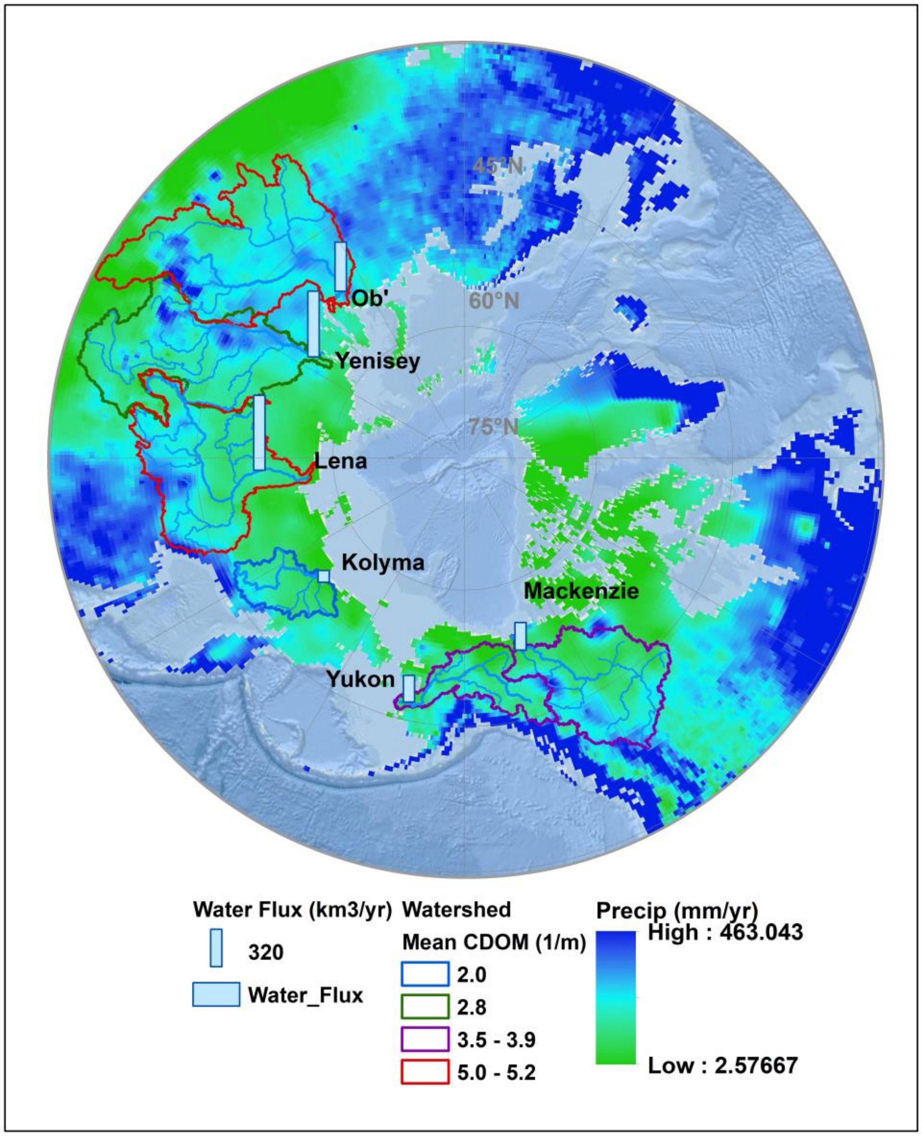

Figure 4-15: Mean riverine CDOM versus mean precipitation of the watersheds. Higher precipitation leads to higher CDOM absorption in the rivers.

Global rising temperature had an important effect on the CDOM input through the river systems. Rising temperature could contribute to CDOM input through its impacts on multiple changings, like rising river discharge contributed by snowmelt, changing landcover types in watersheds. Meanwhile, temperature also directly impacted the leaching of terrestrial CDOM to the water. For instance, temperature is important for controlling the degradation of vegetation litters for producing CDOM. The high temperature could lead to high microbiology productivity for accelerating the vegetation degradation (Dainard and Guéguen 2013; Watras et al. 2011). For instance, the lowest mean temperature in Kolyma river also had low CDOM (Figure 4-16). Again, both the high CDOM rivers (Lena and Ob') showed the relatively higher temperature comparing to the other rivers. At last, one urgent terrestrial environmental changing caused by increasing global temperature in Pan-Arctic regions was the thawing of permafrost soils (MacDougall et al. 2012). Thawing of permafrost soils would cause the leaching of aged carbon from soil to the rivers (Butman et al. 2015). We found most watershed regions were covered by different levels of permafrost. The thawing of permafrost would lead to the significantly rising of terrestrial carbon from land to the Arctic ocean.

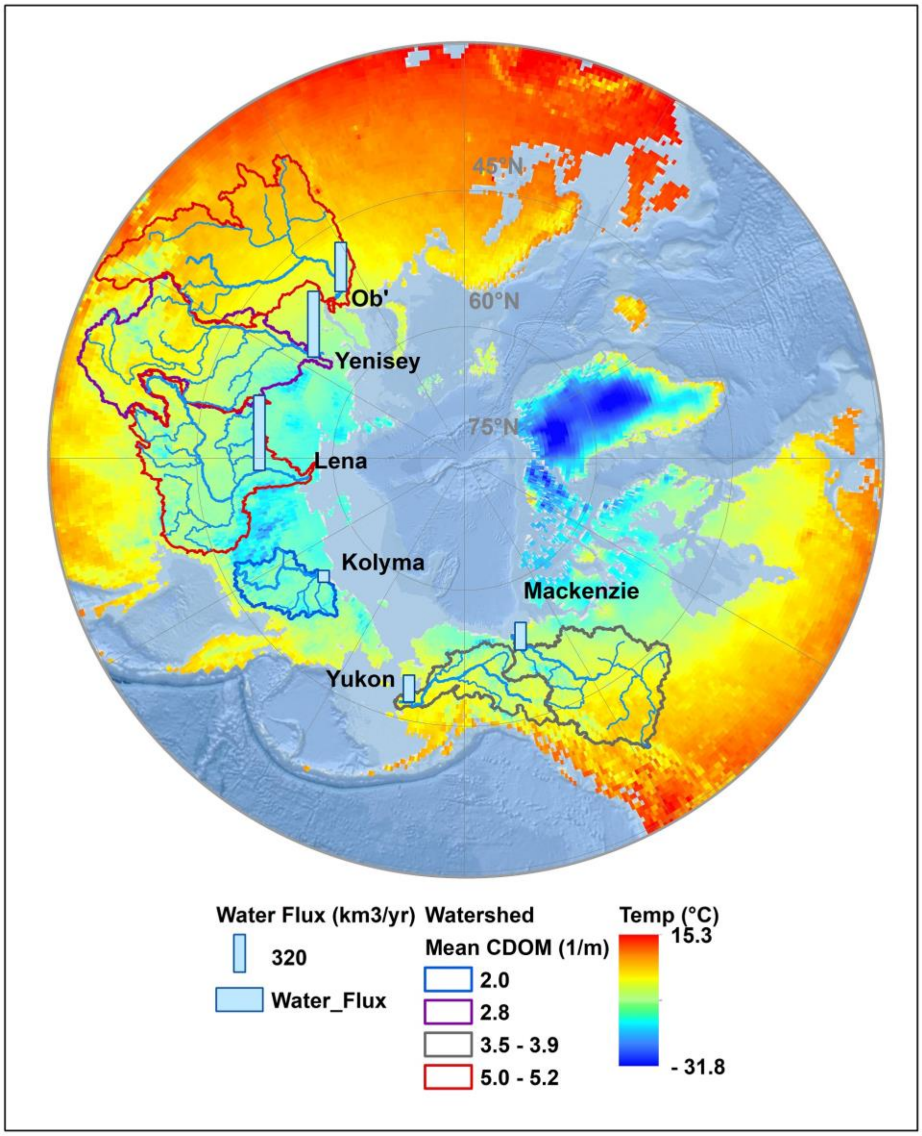

Figure 4-16: Mean air temperature and mean riverine CDOM in six Arctic rivers. Temperature affected the terrestrial CDOM input to the rivers through its multiple impacts on both terrestrial and aquatic environment.

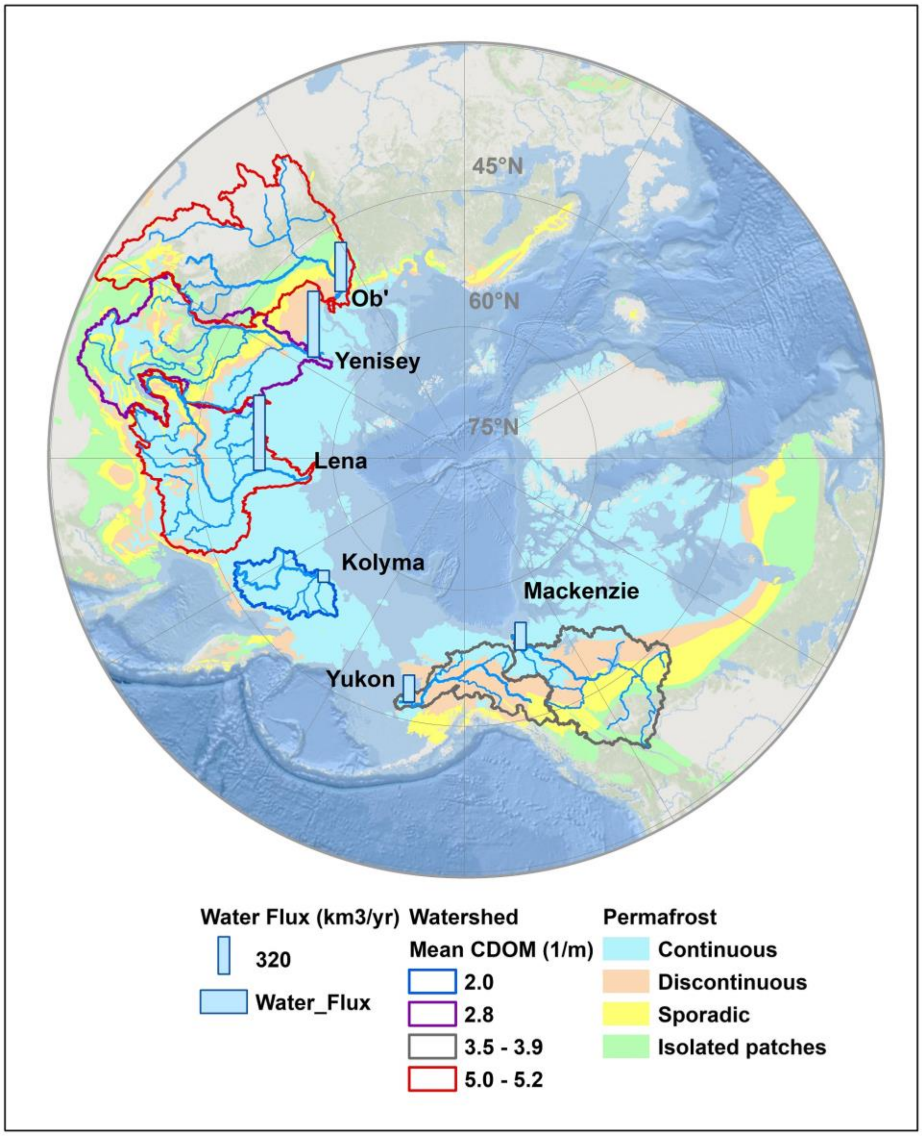

Figure 4-17: Permafrost extent and mean riverine CDOM in the Arctic regions. Continuous permafrost regions had the low CDOM in the rivers.

4.5 Conclusion

CDOM was transported from terrestrial environment to the Arctic Ocean through large Arctic rivers. CDOM spatial and temporal dynamics monitoring via Landsat 8 has significant meaning in carbon cycle assessments in Arctic Region. This chapter applied SBOP on Landsat-8 OLI images to derive CDOM absorption in the six large Arctic rivers. The performance evaluations (RMSE = 0.10 and R^2 = 0.87) demonstrated that this approach could be successfully applied to the large Arctic Rivers. SBOP algorithm was designed to accurately derive CDOM absorption levels by separating bottom reflectance from total water-leaving radiance. It significantly improved the performance of CDOM estimation in optically shallow waters. And Landsat-8 OLI imagery is well suited for CDOM monitoring at the land-water interface.

CDOM absorption derived from satellite images via the SBOP algorithm exhibited clear spatial patterns across space and time. These results illustrate that our algorithm can indeed be applied to monitoring the allochthonous CDOM transportation from land to the Arctic Ocean. The identify of this allochthonous CDOM input via satellite images will ultimately contribute to our better understanding of land-water carbon cycle in Arctic Regions.

Our results illustrate the watershed landcover types have a very important influence on the riverine CDOM variations. Watershed landcover characteristics are important factors associated with the riverine CDOM. Moreover, Landsat-8 OLI imagery also provides the relatively high temporal coverage for the estimation of seasonal dynamics. Our results show the terrestrial CDOM transport into the Arctic Ocean displayed clearly seasonal dynamics. Moreover, CDOM input was highly controlled by the river discharge. Both snowmelt and precipitation contributed to terrestrial CDOM transport to the Arctic Ocean.

In summary, our study confirms that the remote sensing can be used to monitor CDOM at the land-water interface of Arctic Ocean. The results had both high spatial and temporal resolutions. The combination of SBOP algorithm and widely available Landsat-8 OLI imagery present the opportunity to better understand CDOM dynamics in Arctic rivers.

APPENDICES

APPENDIX A

MAJOR MATLAB CODE FOR SBOP

The Keycode for the SBOP algorithm

```
%input filename and header here
envifile = 'Image.dat';
enviheader = 'Image.hdr';

%read samples,lines,etc from header file
[samples, lines, bands, dataType, interleave, byteOrder] =
...
      read_envi_header(enviheader);

%read the image with multibandread as
image = multibandread ...
(envifile, [lines,samples,bands], 'single', 0, interleave,
'ieee-le');

image = double ( image );

%processing begin here:
band1 = image (:, :, 2); %442nm
band2 = image (:, :, 3); %482nm
band3 = image (:, :, 4); %561nm
band4 = image (:, :, 5); %654nm

%set three bands to record the information
band6 = zeros(lines,samples); %bottomref555
band7 = zeros(lines,samples); %cdom
band8 = zeros(lines,samples); %depth

% set water aw and bbw in exp value
% aw xdata1
aw = [0.00635 0.0127 0.0619 0.37];

% bbw xdata2
bbw = [0.002517 0.001729 0.000888 0.000457];

% set bottom relfectance on air Reflectance of Sand (ros)
xdata3
ros = [0.696065 0.81031 1.028484 1.201533];

% set other parameters
s = 0.015;
```

```
y0 = 2;
y1 = 1.2;
y2 = -0.9;
q = 0.75;
g0 = 0.089;
g1 = 0.125;

% 1/cos0
costhew = 1.2;

% set wavelength xdata4
wave = [442 482 561 654];


           % set Y=y_0 (1-y_1 exp(y_2  (r_rs (440))/(r_rs
(555) )))
           y = y0*(1-
y1*exp(y2*(band1(i,j)*0.983)/(band3(i,j)*0.965)));

           % set four unkonw parameters
           % set initial value for these parameters
           phot = 0.05*(image(i,j,1)/image(i,j,3))^(-1.7);
           bott = 0.1;
           part = 0.5*phot;
           cdom = 1.5*phot;
           high = 0.5;

           % set R and Rmod
           R = [0 0 0 0];


           x0 = [bott cdom part high];


           func = @(x)[(0.52*((0.3183*(x(1)*ros(1))*exp(-
(costhew+...

(1.05*(1+5.5*(((x(3)*((440/wave(1))^y))+bbw(1))/...
               (((x(2)*exp(s*(440-
wave(1))))+(q*x(3)*exp(s*(440-wave(1))))+...
               aw(1))+((x(3)*((440/wave(1))^y))+
bbw(1)))))^2))*...
               (((x(2)*exp(s*(440-
wave(1))))+(q*x(3)*exp(s*(440-wave(1))))+...
               aw(1))+((x(3)*((440/wave(1))^y))+
bbw(1)))*x(4)))...
```

```
               +((g0+g1*(((x(3)*((440/wave(1))^y))+
bbw(1))/(((x(2)*...
               exp(s*(440-wave(1))))+(q*x(3)*exp(s*(440-
wave(1))))+aw(1))+...
               ((x(3)*((440/wave(1))^y))+ bbw(1)))))*...
               (((x(3)*((440/wave(1))^y))+bbw(1))/...
               (((x(2)*exp(s*(440-
wave(1))))+(q*x(3)*exp(s*(440-wave(1))))+aw(1))+...
               ((x(3)*((440/wave(1))^y))+ bbw(1))))*...
               (1-exp(-
(costhew+(1.03*(1+2.4*(((x(3)*((440/wave(1))^y))+...
               bbw(1))/(((x(2)*exp(s*(440-wave(1))))+...
               (q*x(3)*exp(s*(440-wave(1))))+aw(1))+...
               ((x(3)*((440/wave(1))^y))+bbw(1)))))^2))*...
               (((x(2)*exp(s*(440-
wave(1))))+(q*x(3)*exp(s*(440-wave(1))))+aw(1))+...
               ((x(3)*((440/wave(1))^y))+
bbw(1)))*x(4)))))/...
               (1-1.7*((0.3183*(x(1)*ros(1))*exp(-
(costhew+(1.05*...
               (1+5.5*(((x(3)*((440/wave(1))^y))+
bbw(1))/...
               (((x(2)*exp(s*(440-
wave(1))))+(q*x(3)*exp(s*(440-wave(1))))+aw(1))+...
               ((x(3)*((440/wave(1))^y))+
bbw(1)))))^2))*...
               (((x(2)*exp(s*(440-
wave(1))))+(q*x(3)*exp(s*(440-wave(1))))+aw(1))+...
               ((x(3)*((440/wave(1))^y))+
bbw(1)))*x(4)))...
               +((g0+g1*(((x(3)*((440/wave(1))^y))+
bbw(1))/...
               (((x(2)*exp(s*(440-
wave(1))))+(q*x(3)*exp(s*(440-wave(1))))+aw(1))+...
               ((x(3)*((440/wave(1))^y))+ bbw(1)))))*...
               (((x(3)*((440/wave(1))^y))+ bbw(1))/...
               (((x(2)*exp(s*(440-
wave(1))))+(q*x(3)*exp(s*(440-wave(1))))+aw(1))...
               +((x(3)*((440/wave(1))^y))+ bbw(1))))*...
               (1-exp(-
(costhew+(1.03*(1+2.4*(((x(3)*((440/wave(1))^y))+...
               bbw(1))/(((x(2)*exp(s*(440-wave(1))))+...
               (q*x(3)*exp(s*(440-wave(1))))+aw(1))+...
               ((x(3)*((440/wave(1))^y))+
bbw(1)))))^2))*...
               (((x(2)*exp(s*(440-
wave(1))))+(q*x(3)*exp(s*(440-wave(1))))+...
```

```
               aw(1))+((x(3)*((440/wave(1))^y))+
bbw(1)))*x(4))))))) - R(1);
               (0.52*((0.3183*(x(1)*ros(2))*exp(-
(costhew+...

(1.05*(1+5.5*(((x(3)*((440/wave(2))^y))+bbw(2))/...
               (((x(2)*exp(s*(440-
wave(2))))+(q*x(3)*exp(s*(440-wave(2))))+...
               aw(2))+((x(3)*((440/wave(2))^y))+
bbw(2)))))^2))*...
               (((x(2)*exp(s*(440-
wave(2))))+(q*x(3)*exp(s*(440-wave(2))))+...
               aw(2))+((x(3)*((440/wave(2))^y))+
bbw(2)))*x(4)))...
               +((g0+g1*(((x(3)*((440/wave(2))^y))+
bbw(2))/(((x(2)*...
               exp(s*(440-wave(2))))+(q*x(3)*exp(s*(440-
wave(2))))+aw(2))+...
               ((x(3)*((440/wave(2))^y))+ bbw(2)))))*...
               (((x(3)*((440/wave(2))^y))+bbw(2))/...
               (((x(2)*exp(s*(440-
wave(2))))+(q*x(3)*exp(s*(440-wave(2))))+aw(2))+...
               ((x(3)*((440/wave(2))^y))+ bbw(2))))*...
               (1-exp(-
(costhew+(1.03*(1+2.4*(((x(3)*((440/wave(2))^y))+...
               bbw(2))/(((x(2)*exp(s*(440-wave(2))))+...
               (q*x(3)*exp(s*(440-wave(2))))+aw(2))+...
               ((x(3)*((440/wave(2))^y))+bbw(2)))))^2))*...
               (((x(2)*exp(s*(440-
wave(2))))+(q*x(3)*exp(s*(440-wave(2))))+aw(2))+...
               ((x(3)*((440/wave(2))^y))+
bbw(2)))*x(4)))))/...
               (1-1.7*((0.3183*(x(1)*ros(2))*exp(-
(costhew+(1.05*...
               (1+5.5*(((x(3)*((440/wave(2))^y))+
bbw(2))/...
               (((x(2)*exp(s*(440-
wave(2))))+(q*x(3)*exp(s*(440-wave(2))))+aw(2))+...
               ((x(3)*((440/wave(2))^y))+
bbw(2)))))^2))*...
               (((x(2)*exp(s*(440-
wave(2))))+(q*x(3)*exp(s*(440-wave(2))))+aw(2))+...
               ((x(3)*((440/wave(2))^y))+
bbw(2)))*x(4)))...
               +((g0+g1*(((x(3)*((440/wave(2))^y))+
bbw(2))/...
```

```
                (((x(2)*exp(s*(440-
wave(2))))+(q*x(3)*exp(s*(440-wave(2))))+aw(2))+...
                ((x(3)*((440/wave(2))^y))+ bbw(2)))))*...
                (((x(3)*((440/wave(2))^y))+ bbw(2))/...
                (((x(2)*exp(s*(440-
wave(2))))+(q*x(3)*exp(s*(440-wave(2))))+aw(2))...
                +((x(3)*((440/wave(2))^y))+ bbw(2))))*...
                (1-exp(-
(costhew+(1.03*(1+2.4*(((x(3)*((440/wave(2))^y))+...
                bbw(2))/(((x(2)*exp(s*(440-wave(2))))+...
                (q*x(3)*exp(s*(440-wave(2))))+aw(2))+...
                ((x(3)*((440/wave(2))^y))+
bbw(2)))))^2))*...
                (((x(2)*exp(s*(440-
wave(2))))+(q*x(3)*exp(s*(440-wave(2))))+...
                aw(2))+((x(3)*((440/wave(2))^y))+
bbw(2)))*x(4))))))) - R(2);
                (0.52*((0.3183*(x(1)*ros(3))*exp(-
(costhew+...

(1.05*(1+5.5*(((x(3)*((440/wave(3))^y))+bbw(3))/...
                (((x(2)*exp(s*(440-
wave(3))))+(q*x(3)*exp(s*(440-wave(3))))+...
                aw(3))+((x(3)*((440/wave(3))^y))+
bbw(3)))))^2))*...
                (((x(2)*exp(s*(440-
wave(3))))+(q*x(3)*exp(s*(440-wave(3))))+...
                aw(3))+((x(3)*((440/wave(3))^y))+
bbw(3)))*x(4)))...
                +((g0+g1*(((x(3)*((440/wave(3))^y))+
bbw(3))/(((x(2)*...
                exp(s*(440-wave(3))))+(q*x(3)*exp(s*(440-
wave(3))))+aw(3))+...
                ((x(3)*((440/wave(3))^y))+ bbw(3)))))*...
                (((x(3)*((440/wave(3))^y))+bbw(3))/...
                (((x(2)*exp(s*(440-
wave(3))))+(q*x(3)*exp(s*(440-wave(3))))+aw(3))+...
                ((x(3)*((440/wave(3))^y))+ bbw(3))))*...
                (1-exp(-
(costhew+(1.03*(1+2.4*(((x(3)*((440/wave(3))^y))+...
                bbw(3))/(((x(2)*exp(s*(440-wave(3))))+...
                (q*x(3)*exp(s*(440-wave(3))))+aw(3))+...
                ((x(3)*((440/wave(3))^y))+bbw(3)))))^2))*...
                (((x(2)*exp(s*(440-
wave(3))))+(q*x(3)*exp(s*(440-wave(3))))+aw(3))+...
                ((x(3)*((440/wave(3))^y))+
bbw(3)))*x(4)))))/...
```

```
                    (1-1.7*((0.3183*(x(1)*ros(3))*exp(-
 (costhew+(1.05*...
                    (1+5.5*(((x(3)*((440/wave(3))^y))+
bbw(3))/...
                    (((x(2)*exp(s*(440-
wave(3))))+(q*x(3)*exp(s*(440-wave(3))))+aw(3))+...
                    ((x(3)*((440/wave(3))^y))+
bbw(3)))))^2))*...
                    (((x(2)*exp(s*(440-
wave(3))))+(q*x(3)*exp(s*(440-wave(3))))+aw(3))+...
                    ((x(3)*((440/wave(3))^y))+
bbw(3)))*x(4)))...
                   +((g0+g1*(((x(3)*((440/wave(3))^y))+
bbw(3))/...
                    (((x(2)*exp(s*(440-
wave(3))))+(q*x(3)*exp(s*(440-wave(3))))+aw(3))+...
                    ((x(3)*((440/wave(3))^y))+ bbw(3)))))*...
                    (((x(3)*((440/wave(3))^y))+ bbw(3))/...
                    (((x(2)*exp(s*(440-
wave(3))))+(q*x(3)*exp(s*(440-wave(3))))+aw(3))...
                   +((x(3)*((440/wave(3))^y))+ bbw(3))))*...
                    (1-exp(-
 (costhew+(1.03*(1+2.4*(((x(3)*((440/wave(3))^y))+...
                   bbw(3))/(((x(2)*exp(s*(440-wave(3))))+...
                    (q*x(3)*exp(s*(440-wave(3))))+aw(3))+...
                    ((x(3)*((440/wave(3))^y))+
bbw(3)))))^2))*...
                    (((x(2)*exp(s*(440-
wave(3))))+(q*x(3)*exp(s*(440-wave(3))))+...
                   aw(3))+((x(3)*((440/wave(3))^y))+
bbw(3)))*x(4))))))) - R(3);
                    (0.52*((0.3183*(x(1)*ros(4))*exp(-
 (costhew+...

 (1.05*(1+5.5*(((x(3)*((440/wave(4))^y))+bbw(4))/...
                    (((x(2)*exp(s*(440-
wave(4))))+(q*x(3)*exp(s*(440-wave(4))))+...
                   aw(4))+((x(3)*((440/wave(4))^y))+
bbw(4)))))^2))*...
                    (((x(2)*exp(s*(440-
wave(4))))+(q*x(3)*exp(s*(440-wave(4))))+...
                   aw(4))+((x(3)*((440/wave(4))^y))+
bbw(4)))*x(4)))...
                   +((g0+g1*(((x(3)*((440/wave(4))^y))+
bbw(4))/(((x(2)*...
                   exp(s*(440-wave(4))))+(q*x(3)*exp(s*(440-
wave(4))))+aw(4))+...
```

```
                ((x(3)*((440/wave(4))^y))+ bbw(4)))))*...
                (((x(3)*((440/wave(4))^y))+bbw(4))/...
                (((x(2)*exp(s*(440-
wave(4))))+(q*x(3)*exp(s*(440-wave(4))))+aw(4))+...
                ((x(3)*((440/wave(4))^y))+ bbw(4))))*...
                (1-exp(-
(costhew+(1.03*(1+2.4*(((x(3)*((440/wave(4))^y))+...
                bbw(4))/(((x(2)*exp(s*(440-wave(4))))+...
                (q*x(3)*exp(s*(440-wave(4))))+aw(4))+...
                ((x(3)*((440/wave(4))^y))+bbw(4)))))^2))*...
                (((x(2)*exp(s*(440-
wave(4))))+(q*x(3)*exp(s*(440-wave(4))))+aw(4))+...
                ((x(3)*((440/wave(4))^y))+
bbw(4)))*x(4))))))/...
                (1-1.7*((0.3183*(x(1)*ros(4))*exp(-
(costhew+(1.05*...
                (1+5.5*(((x(3)*((440/wave(4))^y))+
bbw(4))/...
                (((x(2)*exp(s*(440-
wave(4))))+(q*x(3)*exp(s*(440-wave(4))))+aw(4))+...
                ((x(3)*((440/wave(4))^y))+
bbw(4)))))^2))*...
                (((x(2)*exp(s*(440-
wave(4))))+(q*x(3)*exp(s*(440-wave(4))))+aw(4))+...
                ((x(3)*((440/wave(4))^y))+
bbw(4)))*x(4)))...
                +((g0+g1*(((x(3)*((440/wave(4))^y))+
bbw(4))/...
                (((x(2)*exp(s*(440-
wave(4))))+(q*x(3)*exp(s*(440-wave(4))))+aw(4))+...
                ((x(3)*((440/wave(4))^y))+ bbw(4)))))*...
                (((x(3)*((440/wave(4))^y))+ bbw(4))/...
                (((x(2)*exp(s*(440-
wave(4))))+(q*x(3)*exp(s*(440-wave(4))))+aw(4))...
                +((x(3)*((440/wave(4))^y))+ bbw(4))))*...
                (1-exp(-
(costhew+(1.03*(1+2.4*(((x(3)*((440/wave(4))^y))+...
                bbw(4))/(((x(2)*exp(s*(440-wave(4))))+...
                (q*x(3)*exp(s*(440-wave(4))))+aw(4))+...
                ((x(3)*((440/wave(4))^y))+
bbw(4)))))^2))*...
                (((x(2)*exp(s*(440-
wave(4))))+(q*x(3)*exp(s*(440-wave(4))))+...
                aw(4))+((x(3)*((440/wave(4))^y))+
bbw(4)))*x(4))))))) - R(4)];

            options = optimset();
```

```
            result = fsolve(func,x0);

            band6(i,j) = result(1);
            band7(i,j) = result(2)*exp(s*(440-wave(1)));


       end
   end
end



image (:, :, 6) = band6;%bottom555
image (:, :, 7) = band7;%cdom


 multibandwrite ...
     (image,'Image', 'bsq', 'machfmt','ieee-le','precision','single');
```

APPENDIX B

MAJOR IDL CODE FOR SBOP REQUIRED IMAGE CALCULATE

```
 ;Select the image file
 envi_select, title='Please select a landsat8 Rrs image with 8
bands', fid=hypdata_fid, dims=dims, pos=pos
 if (hypdata_fid eq -1) then return
 envi_file_query, hypdata_fid, data_type=data_type,
fname=hypdata_fname, $
  interleave=interleave, ns=ns, nl=nl, nb=nb, $
  xstart=xstart, ystart=ystart
 map_info=envi_get_map_info(fid=hypdata_fid)

 ;Set the output file
 out_name = envi_pickfile(title='Save the image file as...',
filter='*.img')
 if (n_elements(out_name) eq 0) then return
 openw, unit, out_name, /get_lun

 BandNumber = size(pos, /n_elements)
 Rrs = FLTARR(5,ns,nl)
 Rrs443 = envi_get_data(fid=hypdata_fid, dims=dims, pos=0);
443nm
 Rrs483 = envi_get_data(fid=hypdata_fid, dims=dims, pos=1);
483nm
 Rrs561 = envi_get_data(fid=hypdata_fid, dims=dims, pos=2);
561nm
 Rrs665 = envi_get_data(fid=hypdata_fid, dims=dims, pos=3);
665nm
 Rrs865 = envi_get_data(fid=hypdata_fid, dims=dims, pos=4);
865nm



 Rrs[1,*,*] = Rrs443 * factor1 ;440nm
 Rrs[2,*,*] = Rrs483 * factor2 ;490nm
 Rrs[3,*,*] = Rrs561 * factor3 ;555nm
 Rrs[4,*,*] = Rrs665 * factor4 ;640nm

 for i=0L,4 do begin
  writeu, unit, Rrs[i,*,*]
 endfor
 free_lun, unit
```

```
;Writing new header file
envi_setup_head, fname=out_name, ns=ns, nl=nl, nb=5, $
  data_type=data_type, offset=0, interleave=0, $
  xstart=xstart, ystart=ystart, map_info=map_info, $
  descrip='Test routine output', /write, /open

         End
```

APPENDIX C

SCREEN CAPTURE OF THE DEVELOPED SOFTWARE

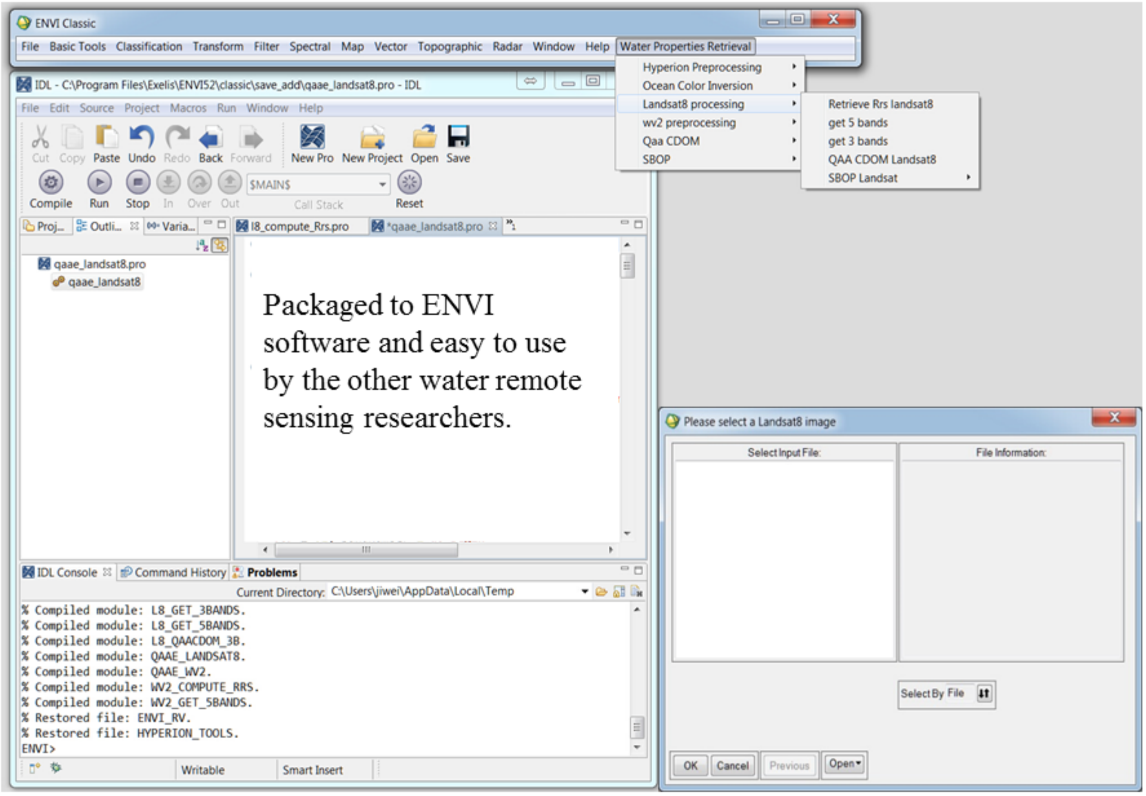

Packaged to ENVI software and easy to use by the other water remote sensing researchers.

```
% Compiled module: L8_GET_3BANDS.
% Compiled module: L8_GET_5BANDS.
% Compiled module: L8_QAACDOM_3B.
% Compiled module: QAAE_LANDSAT8.
% Compiled module: QAAE_WV2.
% Compiled module: WV2_COMPUTE_RRS.
% Compiled module: WV2_GET_5BANDS.
% Restored file: ENVI_RV.
% Restored file: HYPERION_TOOLS.
ENVI>
```

APPENDIX D

ACOLITE PROCESSING

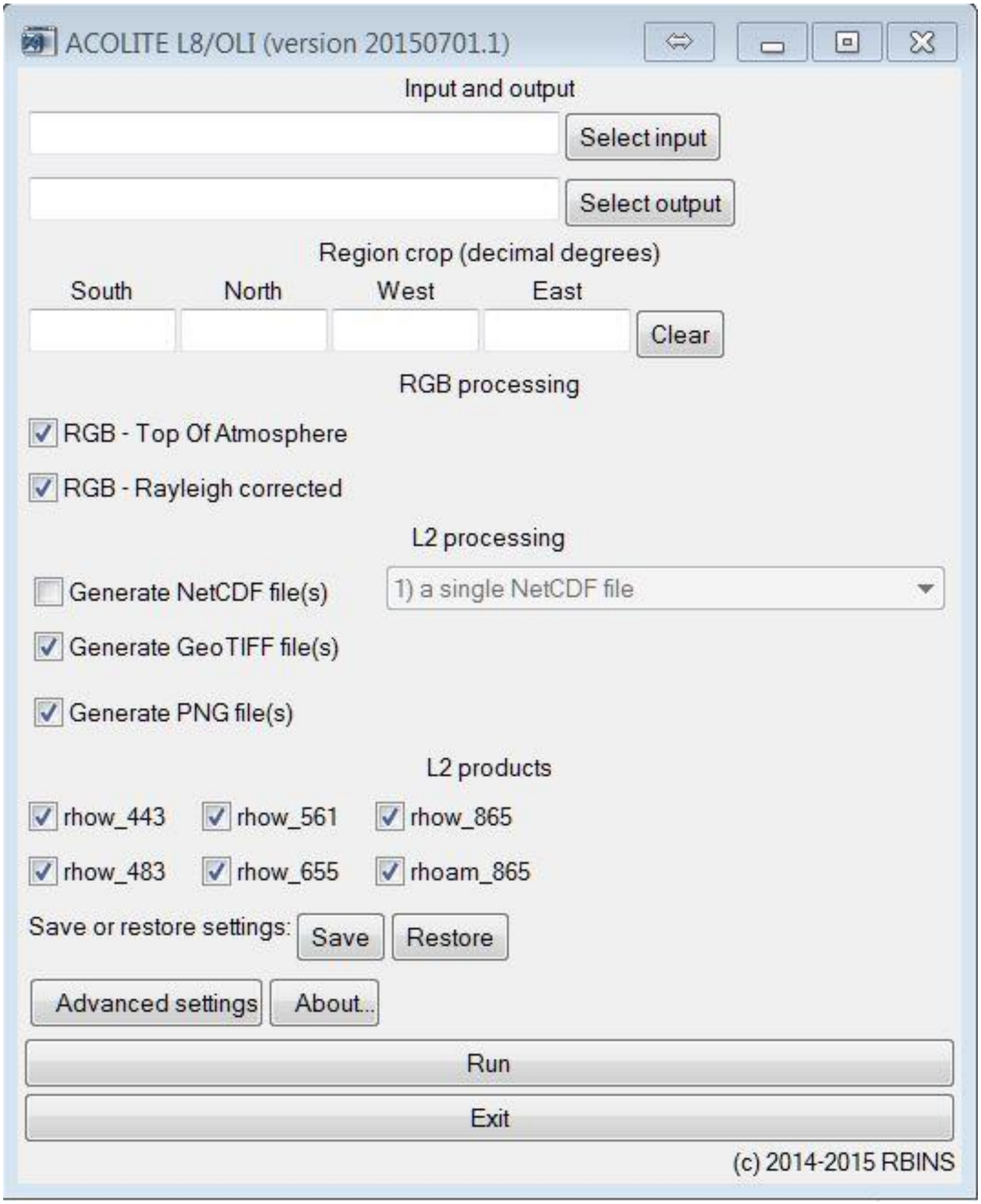

ACOLITE L8/OLI (version 20150701.1)

Input and output

Region crop (decimal degrees)

South North West East

RGB processing

☑ RGB - Top Of Atmosphere

☑ RGB - Rayleigh corrected

L2 processing

☐ Generate NetCDF file(s) 1) a single NetCDF file

☑ Generate GeoTIFF file(s)

☑ Generate PNG file(s)

L2 products

☑ rhow_443 ☑ rhow_561 ☑ rhow_865

☑ rhow_483 ☑ rhow_655 ☑ rhoam_865

Save or restore settings:

(c) 2014-2015 RBINS

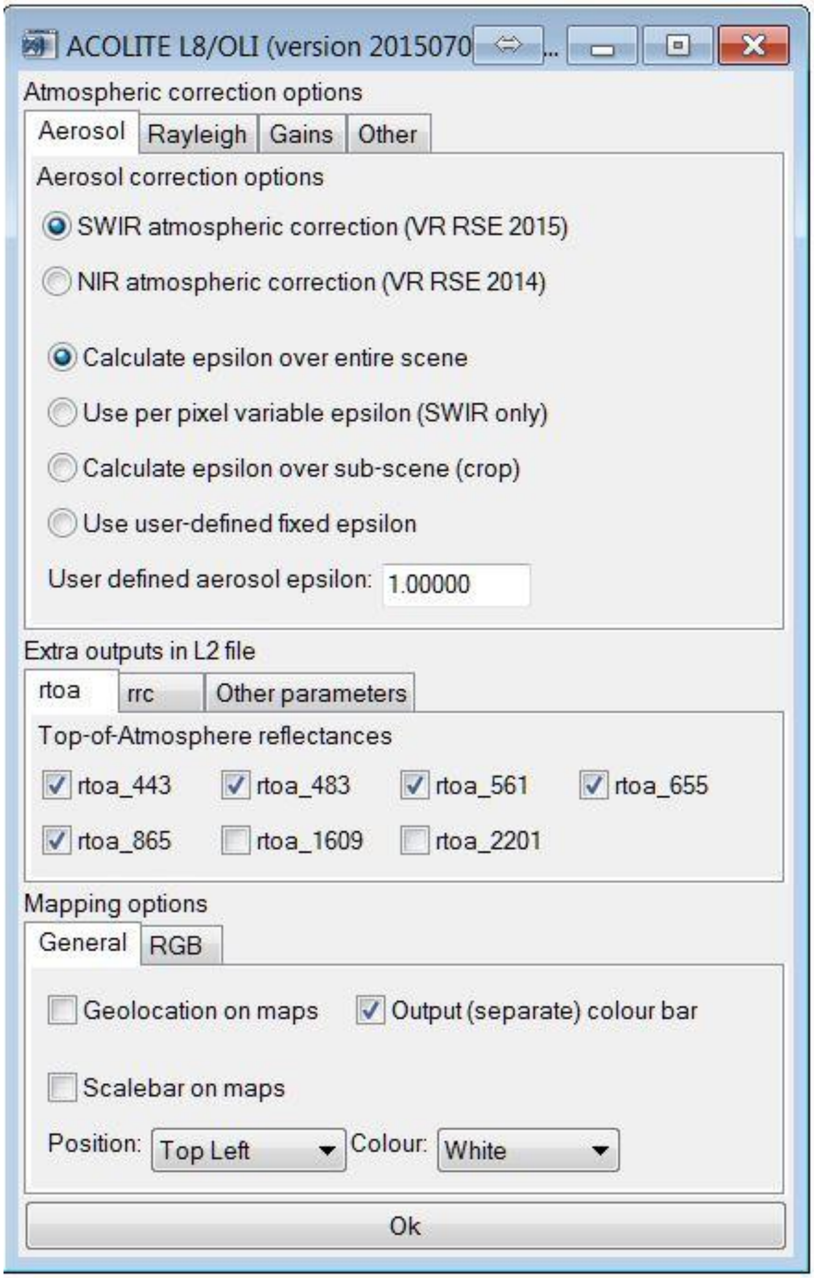

Atmospheric correction options

Aerosol correction options

● SWIR atmospheric correction (VR RSE 2015)

○ NIR atmospheric correction (VR RSE 2014)

● Calculate epsilon over entire scene

○ Use per pixel variable epsilon (SWIR only)

○ Calculate epsilon over sub-scene (crop)

○ Use user-defined fixed epsilon

User defined aerosol epsilon: 1.00000

Extra outputs in L2 file

Top-of-Atmosphere reflectances

☑ rtoa_443 ☑ rtoa_483 ☑ rtoa_561 ☑ rtoa_655

☑ rtoa_865 ☐ rtoa_1609 ☐ rtoa_2201

Mapping options

☐ Geolocation on maps ☑ Output (separate) colour bar

☐ Scalebar on maps

Position: Top Left Colour: White

APPENDIX E

ILLUSTRATION OF UNDERWATER LIGHT TRANSFER

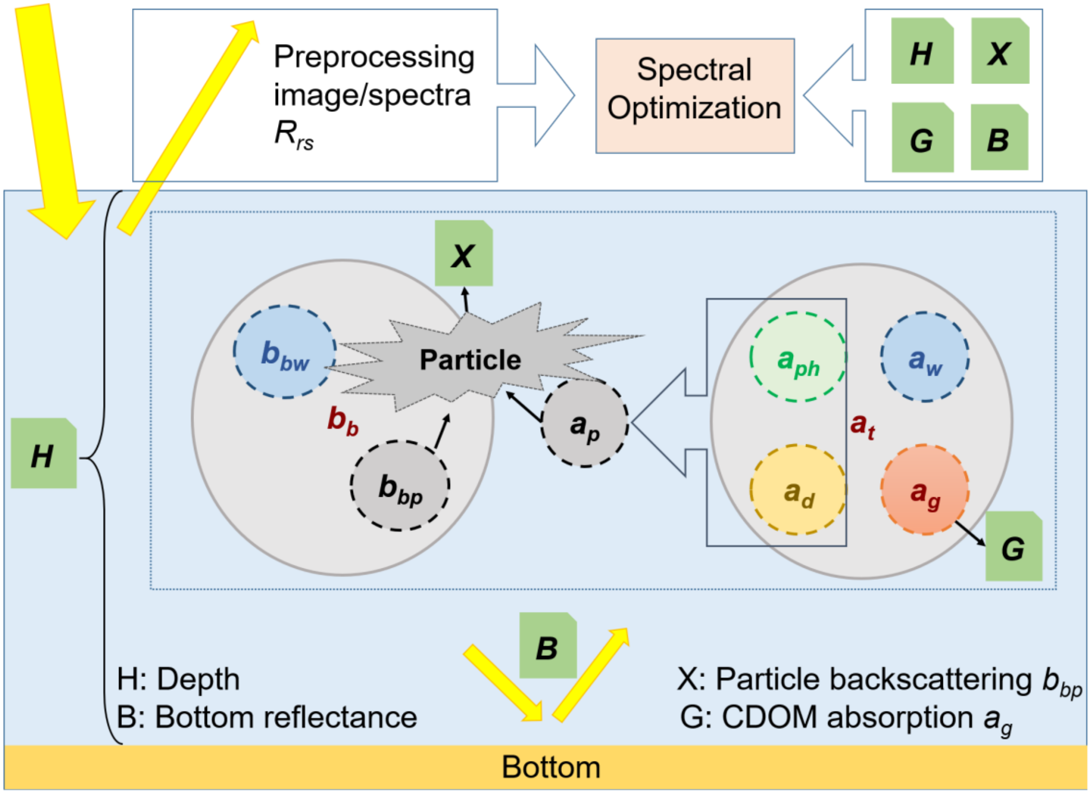

BIBLIOGRAPHY

Ågren, A., Haei, M., Kohler, S., Bishop, K., & Laudon, H. (2010). Regulation of stream water dissolved organic carbon (DOC) concentrations during snowmelt: The role of discharge, winter climate and memory effects. *Biogeosciences, 7*, 2901-2913

Aitkenhead-Peterson, J., McDowell, W., Neff, J., Stuart, E., & Robert, L. (2003a). Sources, production, and regulation of allochthonous dissolved organic matter inputs to surface waters. *Aquatic Ecosystems: Interactivity of Dissolved Organic Matter; Findlay, SEG, Sinsabaugh, RL, Eds*, 25-70

Aitkenhead-Peterson, J., McDowell, W., Neff, J., Stuart, E., & Robert, L. (2003b). *Sources, production, and regulation of allochthonous dissolved organic matter inputs to surface waters*: Academic Press San Diego

Allen, G.H., & Pavelsky, T.M. (2015). Patterns of river width and surface area revealed by the satellite-derived North American River Width data set. *Geophysical research letters, 42*, 395-402

Amon, R., Rinehart, A., Duan, S., Louchouarn, P., Prokushkin, A., Guggenberger, G., Bauch, D., Stedmon, C., Raymond, P., & Holmes, R. (2012). Dissolved organic matter sources in large Arctic rivers. *Geochimica et Cosmochimica Acta, 94*, 217-237

Anderson, J., & Domsch, K. (1975). Measurement of bacterial and fungal contributions to respiration of selected agricultural and forest soils. *Canadian Journal of Microbiology, 21*, 314-322

Arrigo, K.R., & van Dijken, G.L. (2015). Continued increases in Arctic Ocean primary production. *Progress in oceanography, 136*, 60-70

Aziz, O.I.A., & Burn, D.H. (2006). Trends and variability in the hydrological regime of the Mackenzie River Basin. *Journal of Hydrology, 319*, 282-294

Babin, M., Morel, A., Fournier-Sicre, V., Fell, F., & Stramski, D. (2003a). Light scattering properties of marine particles in coastal and open ocean waters as related to the particle mass concentration. *Limnology and Oceanography, 48*, 843-859

Babin, M., Stramski, D., Ferrari, G.M., Claustre, H., Bricaud, A., Obolensky, G., & Hoepffner, N. (2003b). Variations in the light absorption coefficients of phytoplankton, nonalgal particles, and dissolved organic matter in coastal waters around Europe. *Journal of Geophysical Research, 108*, 3211

Baghoth, S., Sharma, S., & Amy, G. (2011). Tracking natural organic matter (NOM) in a drinking water treatment plant using fluorescence excitation–emission matrices and PARAFAC. *water research, 45*, 797-809

Barnes, B.B., Hu, C., Cannizzaro, J.P., Craig, S.E., Hallock, P., Jones, D.L., Lehrter, J.C., Melo, N., Schaeffer, B.A., & Zepp, R. (2014). Estimation of diffuse attenuation of ultraviolet light in optically shallow Florida Keys waters from MODIS measurements. *Remote sensing of Environment, 140*, 519-532

Barnes, B.B., Hu, C., Schaeffer, B.A., Lee, Z., Palandro, D.A., & Lehrter, J.C. (2013). MODIS-derived spatiotemporal water clarity patterns in optically shallow Florida Keys waters: A new approach to remove bottom contamination. *Remote sensing of Environment, 134*, 377-391

Barsi, J.A., Lee, K., Kvaran, G., Markham, B.L., & Pedelty, J.A. (2014). The spectral response of the Landsat-8 operational land imager. *Remote Sensing, 6*, 10232-10251

Battin, T.J., Kaplan, L.A., Findlay, S., Hopkinson, C.S., Marti, E., Packman, A.I., Newbold, J.D., & Sabater, F. (2008). Biophysical controls on organic carbon fluxes in fluvial networks. *Nature Geoscience, 1*, 95-100

Battin, T.J., Luyssaert, S., Kaplan, L.A., Aufdenkampe, A.K., Richter, A., & Tranvik, L.J. (2009). The boundless carbon cycle. *Nature Geoscience, 2*, 598-600

Berto, D., Giani, M., Savelli, F., Centanni, E., Ferrari, C., & Pavoni, B. (2010). Winter to spring variations of chromophoric dissolved organic matter in a temperate estuary (Po River, northern Adriatic Sea). *Marine environmental research, 70*, 73-81

Biancamaria, S., Bates, P.D., Boone, A., & Mognard, N.M. (2009). Large-scale coupled hydrologic and hydraulic modelling of the Ob river in Siberia. *Journal of Hydrology, 379*, 136-150

Bintanja, R., & Selten, F. (2014). Future increases in Arctic precipitation linked to local evaporation and sea-ice retreat. *Nature, 509*, 479-482

Blough, N.V., & Del Vecchio, R. (2002). Chromophoric DOM in the coastal environment. *Biogeochemistry of marine dissolved organic matter*, 509-546

Boike, J., Kattenstroth, B., Abramova, E., Bornemann, N., Chetverova, A., Fedorova, I., Fröb, K., Grigoriev, M., Grüber, M., & Kutzbach, L. (2013). Baseline characteristics of climate, permafrost and land cover from a new permafrost observatory in the Lena River Delta, Siberia (1998-2011). *Biogeosciences (BG), 10*, 2105-2128

Boyer, J., & Groffman, P. (1996). Bioavailability of water extractable organic carbon fractions in forest and agricultural soil profiles. *Soil Biology and Biochemistry, 28*, 783-790

Boyle, E.S., Guerriero, N., Thiallet, A., Vecchio, R.D., & Blough, N.V. (2009). Optical properties of humic substances and CDOM: relation to structure. *Environmental science & technology, 43*, 2262-2268

Brando, V.E., Anstee, J.M., Wettle, M., Dekker, A.G., Phinn, S.R., & Roelfsema, C. (2009). A physics based retrieval and quality assessment of bathymetry from suboptimal hyperspectral data. *Remote sensing of Environment, 113*, 755-770

Brando, V.E., & Dekker, A.G. (2003). Satellite hyperspectral remote sensing for estimating estuarine and coastal water quality. *Geoscience and Remote Sensing, IEEE Transactions on, 41*, 1378-1387

Brezonik, P.L., Olmanson, L.G., Finlay, J.C., & Bauer, M.E. (2015). Factors affecting the measurement of CDOM by remote sensing of optically complex inland waters. *Remote sensing of Environment, 157*, 199-215

Bricaud, A., Morel, A., Babin, M., Allali, K., & Claustre, H. (1998). Variations of light absorption by suspended particles with chlorophyll a concentration in oceanic (case 1) waters: Analysis and implications for bio-optical models. *Journal of Geophysical Research, 103*, 31033-31031,31044

Brown, J., Ferrians Jr, O., Heginbottom, J., & Melnikov, E. (2002). *Circum-Arctic map of permafrost and ground-ice conditions, version 2*: US Geological Survey Reston

Budhiman, S., Salama, M.S., Vekerdy, Z., & Verhoef, W. (2012). Deriving optical properties of Mahakam Delta coastal waters, Indonesia using in situ measurements and ocean color model inversion. *ISPRS Journal of Photogrammetry and Remote Sensing, 68*, 157-169

Burton, T.M., Stricker, C.A., & Uzarski, D.G. (2002). Effects of plant community composition and exposure to wave action on invertebrate habitat use of Lake Huron coastal wetlands. *Lakes & Reservoirs: Research & Management, 7*, 255-269

Butman, D., & Raymond, P.A. (2011). Significant efflux of carbon dioxide from streams and rivers in the United States. *Nature Geoscience, 4*, 839-842

Butman, D.E., Wilson, H.F., Barnes, R.T., Xenopoulos, M.A., & Raymond, P.A. (2015). Increased mobilization of aged carbon to rivers by human disturbance. *Nature Geoscience, 8*, 112-116

Campbell, G., Phinn, S.R., Dekker, A.G., & Brando, V.E. (2011). Remote sensing of water quality in an Australian tropical freshwater impoundment using matrix inversion and MERIS images. *Remote sensing of Environment, 115*, 2402-2414

Cao, F., Tzortziou, M., Hu, C., Mannino, A., Fichot, C.G., Del Vecchio, R., Najjar, R.G., & Novak, M. (2018). Remote sensing retrievals of colored dissolved organic matter and dissolved organic carbon dynamics in North American estuaries and their margins. *Remote sensing of Environment, 205*, 151-165

Carder, K., Chen, F., Cannizzaro, J., Campbell, J., & Mitchell, B. (2004). Performance of the MODIS semi-analytical ocean color algorithm for chlorophyll-< i> a</i>. *Advances in Space Research, 33*, 1152-1159

Carder, K.L., Chen, F., Lee, Z., Hawes, S., & Kamykowski, D. (1999). Semianalytic Moderate-Resolution Imaging Spectrometer algorithms for chlorophyll a and absorption with bio-optical domains based on nitrate-depletion temperatures. *Journal of Geophysical Research: Oceans (1978–2012), 104*, 5403-5421

Chen, J., Zhu, W.-N., Tian, Y.Q., & Yu, Q. (2017). Estimation of Colored Dissolved Organic Matter From Landsat-8 Imagery for Complex Inland Water: Case Study of Lake Huron. *IEEE Transactions on Geoscience and Remote Sensing, 55*, 2201-2212

Chen, M., & Jaffé, R. (2014). Photo-and bio-reactivity patterns of dissolved organic matter from biomass and soil leachates and surface waters in a subtropical wetland. *water research, 61*, 181-190

Cherukuru, N., Ford, P.W., Matear, R.J., Oubelkheir, K., Clementson, L.A., Suber, K., & Steven, A.D. (2016). Estimating dissolved organic carbon concentration in turbid coastal waters using optical remote sensing observations. *International Journal of Applied Earth Observation and Geoinformation, 52*, 149-154

Cole, J.J., Carpenter, S.R., Pace, M.L., Van de Bogert, M.C., Kitchell, J.L., & Hodgson, J.R. (2006). Differential support of lake food webs by three types of terrestrial organic carbon. *Ecology Letters, 9*, 558-568

Cole, J.J., Prairie, Y.T., Caraco, N.F., McDowell, W.H., Tranvik, L.J., Striegl, R.G., Duarte, C.M., Kortelainen, P., Downing, J.A., & Middelburg, J.J. (2007). Plumbing the global carbon cycle: integrating inland waters into the terrestrial carbon budget. *Ecosystems, 10*, 172-185

Cooper, L.W., Benner, R., McClelland, J.W., Peterson, B.J., Holmes, R.M., Raymond, P.A., Hansell, D.A., Grebmeier, J.M., & Codispoti, L.A. (2005). Linkages among runoff, dissolved organic carbon, and the stable oxygen isotope composition of seawater and other water mass indicators in the Arctic Ocean. *Journal of Geophysical Research: Biogeosciences, 110*

Cory, R.M., Ward, C.P., Crump, B.C., & Kling, G.W. (2014). Sunlight controls water column processing of carbon in arctic fresh waters. *science, 345*, 925-928

Cui, T., Zhang, J., Tang, J., Sathyendranath, S., Groom, S., Ma, Y., Zhao, W., & Song, Q. (2014). Assessment of satellite ocean color products of MERIS, MODIS and SeaWiFS along the East China Coast (in the Yellow Sea and East China Sea). *ISPRS Journal of Photogrammetry and Remote Sensing, 87*, 137-151

D'Sa, E.J., & Miller, R.L. (2003). Bio-optical properties in waters influenced by the Mississippi River during low flow conditions. *Remote sensing of Environment, 84*, 538-549

Dainard, P.G., & Guéguen, C. (2013). Distribution of PARAFAC modeled CDOM components in the North Pacific ocean, Bering, Chukchi and Beaufort seas. *Marine Chemistry, 157*, 216-223

Dall'Olmo, G., Gitelson, A.A., Rundquist, D.C., Leavitt, B., Barrow, T., & Holz, J.C. (2005). Assessing the potential of SeaWiFS and MODIS for estimating chlorophyll concentration in turbid productive waters using red and near-infrared bands. *Remote sensing of Environment, 96*, 176-187

Darecki, M., & Stramski, D. (2004). An evaluation of MODIS and SeaWiFS bio-optical algorithms in the Baltic Sea. *Remote sensing of Environment, 89*, 326-350

Davidson, E.A., Figueiredo, R.O., Markewitz, D., & Aufdenkampe, A.K. (2010). Dissolved CO2 in small catchment streams of eastern Amazonia: A minor pathway of terrestrial carbon loss. *Journal of Geophysical Research: Biogeosciences, 115*

Dekker, A.G., Phinn, S.R., Anstee, J., Bissett, P., Brando, V.E., Casey, B., Fearns, P., Hedley, J., Klonowski, W., & Lee, Z.P. (2011). Intercomparison of shallow water bathymetry, hydro-optics, and benthos mapping techniques in Australian and Caribbean coastal environments. *Limnology and Oceanography: Methods, 9*, 396-425

Del Castillo, C.E., Coble, P.G., Morell, J.M., López, J.M., & Corredor, J.E. (1999). Analysis of the optical properties of the Orinoco River plume by absorption and fluorescence spectroscopy. *Marine Chemistry, 66*, 35-51

Del Castillo, C.E., & Miller, R.L. (2008). On the use of ocean color remote sensing to measure the transport of dissolved organic carbon by the Mississippi River Plume. *Remote sensing of Environment, 112*, 836-844

Del Vecchio, R., & Blough, N.V. (2002). Photobleaching of chromophoric dissolved organic matter in natural waters: kinetics and modeling. *Marine Chemistry, 78*, 231-253

Del Vecchio, R., & Blough, N.V. (2004). Spatial and seasonal distribution of chromophoric dissolved organic matter and dissolved organic carbon in the Middle Atlantic Bight. *Marine Chemistry, 89*, 169-187

Diehl, S. (2002). Phytoplankton, light, and nutrients in a gradient of mixing depths: theory. *Ecology, 83*, 386-398

Dierssen, H.M. (2010). Perspectives on empirical approaches for ocean color remote sensing of chlorophyll in a changing climate. *Proceedings of the National Academy of Sciences, 107*, 17073-17078

Dogliotti, A., Ruddick, K., Nechad, B., Doxaran, D., & Knaeps, E. (2015). A single algorithm to retrieve turbidity from remotely-sensed data in all coastal and estuarine waters. *Remote sensing of Environment, 156*, 157-168

Dominy, C., & Haynes, R. (2002). Influence of agricultural land management on organic matter content, microbial activity and aggregate stability in the profiles of two Oxisols. *Biology and Fertility of Soils, 36*, 298-305

Doxaran, D., Cherukuru, R., & Lavender, S. (2005). Use of reflectance band ratios to estimate suspended and dissolved matter concentrations in estuarine waters. *International Journal of Remote Sensing, 26*, 1763-1769

Doxaran, D., Ehn, J., Bélanger, S., Matsuoka, A., Hooker, S., & Babin, M. (2012). Optical characterisation of suspended particles in the Mackenzie River plume (Canadian Arctic Ocean) and implications for ocean colour remote sensing. *Biogeosciences, 9*, 3213-3229

Doxaran, D., Froidefond, J.-M., & Castaing, P. (2002). A reflectance band ratio used to estimate suspended matter concentrations in sediment-dominated coastal waters. *International Journal of Remote Sensing, 23*, 5079-5085

EPA (2008). Factoids: drinking water and ground water statistics for 2007

Evans, C., Monteith, D., & Cooper, D. (2005). Long-term increases in surface water dissolved organic carbon: observations, possible causes and environmental impacts. *Environmental Pollution, 137*, 55-71

Falkowski, P.G., & Raven, J.A. (2013). *Aquatic photosynthesis*: Princeton University Press

Feng, X., Vonk, J.E., van Dongen, B.E., Gustafsson, Ö., Semiletov, I.P., Dudarev, O.V., Wang, Z., Montluçon, D.B., Wacker, L., & Eglinton, T.I. (2013). Differential mobilization of terrestrial carbon pools in Eurasian Arctic river basins. *Proceedings of the National Academy of Sciences, 110*, 14168-14173

Ferrari, G.M., Dowell, M.D., Grossi, S., & Targa, C. (1996). Relationship between the optical properties of chromophoric dissolved organic matter and total concentration of dissolved organic carbon in the southern Baltic Sea region. *Marine Chemistry, 55*, 299-316

Fichot, C.G., Kaiser, K., Hooker, S.B., Amon, R.M., Babin, M., Bélanger, S., Walker, S.A., & Benner, R. (2013). Pan-Arctic distributions of continental runoff in the Arctic Ocean. *Scientific reports, 3*, 1053

Findlay, S., Quinn, J.M., Hickey, C.W., Burrell, G., & Downes, M. (2001). Effects of land use and riparian flowpath on delivery of dissolved organic carbon to streams. *Limnology and Oceanography, 46*, 345-355

Frey, K.E., Sobczak, W.V., Mann, P.J., & Holmes, R.M. (2016). Optical properties and bioavailability of dissolved organic matter along a flow-path continuum from soil pore waters to the Kolyma River mainstem, East Siberia. *Biogeosciences, 13*, 2279

Friedl, M.A., Sulla-Menashe, D., Tan, B., Schneider, A., Ramankutty, N., Sibley, A., & Huang, X. (2010). MODIS Collection 5 global land cover: Algorithm refinements and characterization of new datasets. *Remote sensing of Environment, 114*, 168-182

Giardino, C., Bresciani, M., Valentini, E., Gasperini, L., Bolpagni, R., & Brando, V.E. (2015). Airborne hyperspectral data to assess suspended particulate matter and aquatic vegetation in a shallow and turbid lake. *Remote sensing of Environment, 157*, 48-57

Gons, H.J., Auer, M.T., & Effler, S.W. (2008). MERIS satellite chlorophyll mapping of oligotrophic and eutrophic waters in the Laurentian Great Lakes. *Remote sensing of Environment, 112*, 4098-4106

Gordon, H.R. (1997). Atmospheric correction of ocean color imagery in the Earth Observing System era. *Journal of Geophysical Research: Atmospheres (1984–2012), 102*, 17081-17106

Gordon, H.R., & Wang, M. (1992). Surface-roughness considerations for atmospheric correction of ocean color sensors. I: The Rayleigh-scattering component. *Applied Optics, 31*, 4247-4260

Gordon, H.R., & Wang, M. (1994). Retrieval of water-leaving radiance and aerosol optical thickness over the oceans with SeaWiFS: a preliminary algorithm. *Applied Optics, 33*, 443-452

Granskog, M.A., Macdonald, R.W., Mundy, C.-J., & Barber, D.G. (2007). Distribution, characteristics and potential impacts of chromophoric dissolved organic matter (CDOM) in Hudson Strait and Hudson Bay, Canada. *Continental Shelf Research, 27*, 2032-2050

Gregg, W.W., Casey, N.W., & McClain, C.R. (2005). Recent trends in global ocean chlorophyll. *Geophysical research letters, 32*

Haei, M., Öquist, M.G., Buffam, I., Ågren, A., Blomkvist, P., Bishop, K., Ottosson Löfvenius, M., & Laudon, H. (2010). Cold winter soils enhance dissolved organic carbon concentrations in soil and stream water. *Geophysical research letters, 37*

Hestir, E.L., Brando, V., Campbell, G., Dekker, A., & Malthus, T. (2015). The relationship between dissolved organic matter absorption and dissolved organic carbon in reservoirs along a temperate to tropical gradient. *Remote sensing of Environment, 156*, 395-402

Hoge, F.E., & Lyon, P.E. (1996). Satellite retrieval of inherent optical properties by linear matrix inversion of oceanic radiance models: an analysis of model and radiance measurement errors. *Journal of Geophysical Research, 101*, 16631-16616,16648

Holmes, R., Shiklomanov, A., Tank, S., McClelland, J., & Tretiakov, M. (2015). River discharge, Arctic report card: update for 2015. In

Holmes, R.M., McClelland, J.W., Peterson, B.J., Tank, S.E., Bulygina, E., Eglinton, T.I., Gordeev, V.V., Gurtovaya, T.Y., Raymond, P.A., & Repeta, D.J. (2012). Seasonal and annual fluxes of nutrients and organic matter from large rivers to the Arctic Ocean and surrounding seas. *Estuaries and Coasts, 35*, 369-382

Holmes, R.M., McClelland, J.W., Raymond, P.A., Frazer, B.B., Peterson, B.J., & Stieglitz, M. (2008). Lability of DOC transported by Alaskan rivers to the Arctic Ocean. *Geophysical research letters, 35*

Hornberger, G., Bencala, K., & McKnight, D. (1994). Hydrological controls on dissolved organic carbon during snowmelt in the Snake River near Montezuma, Colorado. *Biogeochemistry, 25*, 147-165

Hu, C., Carder, K.L., & Muller-Karger, F.E. (2000). Atmospheric correction of SeaWiFS imagery over turbid coastal waters: a practical method. *Remote sensing of Environment, 74*, 195-206

IPCC (2007). *Climate Change 2007: Impacts, Adaptation and Vulnerability: Working Group II Contribution to the Fourth Assessment Report of the IPCC Intergovernmental Panel on Climate Change*: Cambridge University Press

Jamet, C., Loisel, H., Kuchinke, C.P., Ruddick, K., Zibordi, G., & Feng, H. (2011). Comparison of three SeaWiFS atmospheric correction algorithms for turbid waters using AERONET-OC measurements. *Remote sensing of Environment, 115*, 1955-1965

Jansson, M., Bergström, A.-K., Blomqvist, P., & Drakare, S. (2000). Allochthonous organic carbon and phytoplankton/bacterioplankton production relationships in lakes. *Ecology, 81*, 3250-3255

Jonsson, A., Karlsson, J., & Jansson, M. (2003). Sources of carbon dioxide supersaturation in clearwater and humic lakes in northern Sweden. *Ecosystems, 6*, 224-235

Kahru, M., & Mitchell, B.G. (2001). Seasonal and nonseasonal variability of satellite-derived chlorophyll and colored dissolved organic matter concentration in the California Current. *Journal of Geophysical Research: Oceans (1978–2012), 106*, 2517-2529

Kalbitz, K., & Kaiser, K. (2008). Contribution of dissolved organic matter to carbon storage in forest mineral soils. *Journal of Plant Nutrition and Soil Science, 171*, 52-60

Kalbitz, K., Solinger, S., Park, J.-H., Michalzik, B., & Matzner, E. (2000a). Controls on the dynamics of dissolved organic matter in soils: a review. *Soil science, 165*, 277-304

Kalbitz, K., Solinger, S., Park, J.H., Michalzik, B., & Matzner, E. (2000b). Controls on the dynamics of dissolved organic matter in soils: A review. *Soil Science, 165*, 277-304

Kelly, P.T., Solomon, C.T., Weidel, B.C., & Jones, S.E. (2014). Terrestrial carbon is a resource, but not a subsidy, for lake zooplankton. *Ecology, 95*, 1236-1242

Kicklighter, D.W., Hayes, D.J., McClelland, J.W., Peterson, B.J., McGuire, A.D., & Melillo, J.M. (2013). Insights and issues with simulating terrestrial DOC loading of Arctic river networks. *Ecological applications, 23*, 1817-1836

Kindler, R., Siemens, J., Kaiser, K., Walmsley, D.C., Bernhofer, C., Buchmann, N., Cellier, P., Eugster, W., Gleixner, G., & GRŨNWALD, T. (2011). Dissolved carbon leaching from soil is a crucial component of the net ecosystem carbon balance. *Global Change Biology, 17*, 1167-1185

Klonowski, W.M., Fearns, P.R., & Lynch, M.J. (2007). Retrieving key benthic cover types and bathymetry from hyperspectral imagery. *Journal of Applied Remote Sensing, 1*, 011505-011505-011521

Kowalczuk, P., Cooper, W.J., Whitehead, R.F., Durako, M.J., & Sheldon, W. (2003). Characterization of CDOM in an organic-rich river and surrounding coastal ocean in the South Atlantic Bight. *Aquatic sciences, 65*, 384-401

Kowalczuk, P., Stedmon, C.A., & Markager, S. (2006). Modeling absorption by CDOM in the Baltic Sea from season, salinity and chlorophyll. *Marine Chemistry, 101*, 1-11

Kritzberg, E.S., Cole, J.J., Pace, M.L., Granéli, W., & Bade, D.L. (2004). Autochthonous versus allochthonous carbon sources of bacteria: Results from whole-lake 13C addition experiments. *Limnology and Oceanography, 49*, 588-596

Kurylyk, B.L., MacQuarrie, K.T., & McKenzie, J.M. (2014). Climate change impacts on groundwater and soil temperatures in cold and temperate regions: Implications, mathematical theory, and emerging simulation tools. *Earth-Science Reviews, 138*, 313-334

Kutser, T., Casal Pascual, G., Barbosa, C., Paavel, B., Ferreira, R., Carvalho, L., & Toming, K. (2016a). Mapping inland water carbon content with Landsat 8 data. *International Journal of Remote Sensing, 37*, 2950-2961

Kutser, T., Paavel, B., Verpoorter, C., Ligi, M., Soomets, T., Toming, K., & Casal, G. (2016b). Remote sensing of black lakes and using 810 nm reflectance peak for retrieving water quality parameters of optically complex waters. *Remote Sensing, 8*, 497

Kutser, T., Pierson, D.C., Kallio, K.Y., Reinart, A., & Sobek, S. (2005). Mapping lake CDOM by satellite remote sensing. *Remote sensing of Environment, 94*, 535-540

Kutser, T., Verpoorter, C., Paavel, B., & Tranvik, L.J. (2015). Estimating lake carbon fractions from remote sensing data. *Remote sensing of Environment, 157*, 138-146

Larkum, A., & Wood, W. (1993). The effect of UV-B radiation on photosynthesis and respiration of phytoplankton, benthic macroalgae and seagrasses. *Photosynthesis Research, 36*, 17-23

Laudon, H., Berggren, M., Ågren, A., Buffam, I., Bishop, K., Grabs, T., Jansson, M., & Köhler, S. (2011). Patterns and dynamics of dissolved organic carbon (DOC) in boreal streams: the role of processes, connectivity, and scaling. *Ecosystems, 14*, 880-893

Le, C., Hu, C., Cannizzaro, J., English, D., Muller-Karger, F., & Lee, Z. (2013). Evaluation of chlorophyll-a remote sensing algorithms for an optically complex estuary. *Remote sensing of Environment, 129*, 75-89

Lee, Z. (2006). Reports of the International Ocean-Colour Coordinating Group

Lee, Z., Carder, K.L., & Arnone, R.A. (2002). Deriving inherent optical properties from water color: a multiband quasi-analytical algorithm for optically deep waters. *Applied Optics, 41*, 5755-5772

Lee, Z., Carder, K.L., Mobley, C.D., Steward, R.G., & Patch, J.S. (1998). Hyperspectral remote sensing for shallow waters. I. A semianalytical model. *Applied Optics, 37*, 6329-6338

Lee, Z., Carder, K.L., Mobley, C.D., Steward, R.G., & Patch, J.S. (1999). Hyperspectral remote sensing for shallow waters. 2. Deriving bottom depths and water properties by optimization. *Applied Optics, 38*, 3831-3843

Lee, Z., Casey, B., Arnone, R., Weidemann, A., Parsons, R., Montes, M.J., Gao, B.-C., Goode, W., Davis, C., & Dye, J. (2007). Water and bottom properties of a coastal environment derived from Hyperion data measured from the EO-1 spacecraft platform. *Journal of Applied Remote Sensing, 1*, 011502-011502-011516

Lee, Z., Lubac, B., Werdell, J., & Arnone, R. An update of the quasi-analytical algorithm (QAA_v5)

Lee, Z., Weidemann, A., & Arnone, R. (2013). Combined Effect of Reduced Band Number and Increased Bandwidth on Shallow Water Remote Sensing: The Case of WorldView 2

Li, J., Yu, Q., Tian, Y.Q., & Becker, B.L. (2017). Remote sensing estimation of colored dissolved organic matter (CDOM) in optically shallow waters. *ISPRS Journal of Photogrammetry and Remote Sensing, 128*, 98-110

MacDougall, A.H., Avis, C.A., & Weaver, A.J. (2012). Significant contribution to climate warming from the permafrost carbon feedback. *Nature Geoscience, 5*, 719-721

Maie, N., Jaffé, R., Miyoshi, T., & Childers, D.L. (2006). Quantitative and qualitative aspects of dissolved organic carbon leached from senescent plants in an oligotrophic wetland. *Biogeochemistry, 78*, 285-314

Major, J., Lehmann, J., Rondon, M., & Goodale, C. (2010). Fate of soil-applied black carbon: downward migration, leaching and soil respiration. *Global Change Biology, 16*, 1366-1379

Majozi, N.P., Salama, M.S., Bernard, S., Harper, D.M., & Habte, M.G. (2014). Remote sensing of euphotic depth in shallow tropical inland waters of Lake Naivasha using MERIS data. *Remote sensing of Environment, 148*, 178-189

Mann, P., Davydova, A., Zimov, N., Spencer, R., Davydov, S., Bulygina, E., Zimov, S., & Holmes, R. (2012). Controls on the composition and lability of dissolved organic matter in Siberia's Kolyma River basin. *Journal of Geophysical Research: Biogeosciences, 117*

Mann, P.J., Spencer, R.G., Hernes, P.J., Six, J., Aiken, G.R., Tank, S.E., McClelland, J.W., Butler, K.D., Dyda, R.Y., & Holmes, R.M. (2016). Pan-arctic trends in terrestrial dissolved organic matter from optical measurements. *Frontiers in Earth Science, 4*, 25

Mann, P.J., Spencer, R.G., Hernes, P.J., Six, J., Aiken, G.R., Tank, S.E., McClelland, J.W., Butler, K.D., Dyda, R.Y., & Holmes, R.M. (2017). Pan-arctic trends in terrestrial dissolved organic matter from optical measurements. *Linking Optical and Chemical Properties of Dissolved Organic Matter in Natural Waters*, 60

Mannino, A., Russ, M.E., & Hooker, S.B. (2008). Algorithm development and validation for satellite-derived distributions of DOC and CDOM in the US Middle Atlantic Bight. *Journal of Geophysical Research: Oceans (1978–2012), 113*

Maritorena, S., d'Andon, O.H.F., Mangin, A., & Siegel, D.A. (2010). Merged satellite ocean color data products using a bio-optical model: Characteristics, benefits and issues. *Remote sensing of Environment, 114*, 1791-1804

Maritorena, S., Morel, A., & Gentili, B. (1994). Diffuse reflectance of oceanic shallow waters: Influence of water depth and bottom albedo. *Limnology and Oceanography, 39*, 1689-1703

Maritorena, S., Siegel, D.A., & Peterson, A.R. (2002). Optimization of a semianalytical ocean color model for global-scale applications. *Applied Optics, 41*, 2705-2714

Markager, S., & Vincent, W.F. (2000). Spectral light attenuation and the absorption of UV and blue light in natural waters. *Limnology and Oceanography, 45*, 642-650

Matilainen, A., Vepsäläinen, M., & Sillanpää, M. (2010). Natural organic matter removal by coagulation during drinking water treatment: A review. *Advances in colloid and interface science, 159*, 189-197

Matsuoka, A., Boss, E., Babin, M., Karp-Boss, L., Hafez, M., Chekalyuk, A., Proctor, C.W., Werdell, P.J., & Bricaud, A. (2017). Pan-Arctic optical characteristics of colored dissolved organic matter: Tracing dissolved organic carbon in changing Arctic waters using satellite ocean color data. *Remote sensing of Environment, 200*, 89-101

Matsuoka, A., Hooker, S., Bricaud, A., Gentili, B., & Babin, M. (2013). Estimating absorption coefficients of colored dissolved organic matter (CDOM) using a semi-analytical algorithm for southern Beaufort Sea waters: application to deriving concentrations of dissolved organic carbon from space. *Biogeosciences, 10*, 917-927

Matsuoka, A., Ortega-Retuerta, E., Bricaud, A., Arrigo, K.R., & Babin, M. (2015). Characteristics of colored dissolved organic matter (CDOM) in the Western Arctic Ocean: relationships with microbial activities. *Deep Sea Research Part II: Topical Studies in Oceanography, 118*, 44-52

Matthews, M.W. (2011). A current review of empirical procedures of remote sensing in inland and near-coastal transitional waters. *International Journal of Remote Sensing, 32*, 6855-6899

McClelland, J.W., Déry, S.J., Peterson, B.J., Holmes, R.M., & Wood, E.F. (2006). A pan-arctic evaluation of changes in river discharge during the latter half of the 20th century. *Geophysical research letters, 33*

McClelland, J.W., Holmes, R., Dunton, K., & Macdonald, R. (2012). The Arctic ocean estuary. *Estuaries and Coasts, 35*, 353-368

McClelland, J.W., Holmes, R.M., Peterson, B.J., & Stieglitz, M. (2004). Increasing river discharge in the Eurasian Arctic: Consideration of dams, permafrost thaw, and fires as potential agents of change. *Journal of Geophysical Research: Atmospheres, 109*

Melnikov, S., Carroll, J., Gorshkov, A., Vlasov, S., & Dahle, S. (2003). Snow and ice concentrations of selected persistent pollutants in the Ob–Yenisey River watershed. *Science of the Total Environment, 306*, 27-37

Menon, H.B., Sangekar, N.P., Lotliker, A.A., & Vethamony, P. (2011). Dynamics of chromophoric dissolved organic matter in Mandovi and Zuari estuaries—A study through in situ and satellite data. *ISPRS Journal of Photogrammetry and Remote Sensing, 66*, 545-552

Meon, B., & Kirchman, D.L. (2001). Dynamics and molecular composition of dissolved organic material during experimental phytoplankton blooms. *Marine Chemistry, 75*, 185-199

Michalzik, B., Kalbitz, K., Park, J.H., Solinger, S., & Matzner, E. (2001). Fluxes and concentrations of dissolved organic carbon and nitrogen - a synthesis for temperate forests. *Biogeochemistry, 52*, 173-205

Miller, R.L., & McKee, B.A. (2004). Using MODIS Terra 250 m imagery to map concentrations of total suspended matter in coastal waters. *Remote sensing of Environment, 93*, 259-266

Milliman, J.D., Farnsworth, K., Jones, P., Xu, K., & Smith, L. (2008). Climatic and anthropogenic factors affecting river discharge to the global ocean, 1951–2000. *Global and Planetary Change, 62*, 187-194

Mobley, C.D. (1994). *Light and water: Radiative transfer in natural waters*: Academic press San Diego

Mobley, C.D. (1995). The optical properties of water. *Handbook of optics, 2*

Mobley, C.D. (1999). Estimation of the remote-sensing reflectance from above-surface measurements. *Applied Optics, 38*, 7442-7455

Mobley, C.D., Gentili, B., Gordon, H.R., Jin, Z., Kattawar, G.W., Morel, A., Reinersman, P., Stamnes, K., & Stavn, R.H. (1993). Comparison of numerical models for computing underwater light fields. *Applied Optics, 32*, 7484-7504

Morel, A. (1974). Optical properties of pure water and pure sea water. *Optical aspects of oceanography, 1*, 1-24

Morel, A., & Gentili, B. (2009). A simple band ratio technique to quantify the colored dissolved and detrital organic material from ocean color remotely sensed data. *Remote sensing of Environment, 113*, 998-1011

Neff, J.C., & Asner, G.P. (2001). Dissolved organic carbon in terrestrial ecosystems: Synthesis and a model. *Ecosystems, 4*, 29-48

Nohara, D., Kitoh, A., Hosaka, M., & Oki, T. (2006). Impact of climate change on river discharge projected by multimodel ensemble. *Journal of Hydrometeorology, 7*, 1076-1089

O'Reilly, J.E., Maritorena, S., Mitchell, B.G., Siegel, D.A., Carder, K.L., Garver, S.A., Kahru, M., & McClain, C. (1998). Ocean color chlorophyll algorithms for SeaWiFS. *Journal of Geophysical Research: Oceans (1978–2012), 103*, 24937-24953

O’Reilly, J.E., Maritorena, S., Siegel, D.A., O’Brien, M.C., Toole, D., Mitchell, B.G., Kahru, M., Chavez, F.P., Strutton, P., & Cota, G.F. (2000). Ocean color chlorophyll a algorithms for SeaWiFS, OC2, and OC4: Version 4. *SeaWiFS postlaunch calibration and validation analyses, Part, 3*, 9-23

Odermatt, D., Gitelson, A., Brando, V.E., & Schaepman, M. (2012). Review of constituent retrieval in optically deep and complex waters from satellite imagery. *Remote sensing of Environment, 118*, 116-126

Olmanson, L.G., Brezonik, P.L., Finlay, J.C., & Bauer, M.E. (2016). Comparison of Landsat 8 and Landsat 7 for regional measurements of CDOM and water clarity in lakes. *Remote sensing of Environment*

Pahlevan, N., Lee, Z., Wei, J., Schaaf, C.B., Schott, J.R., & Berk, A. (2014). On-orbit radiometric characterization of OLI (Landsat-8) for applications in aquatic remote sensing. *Remote sensing of Environment, 154*, 272-284

Palmer, S.C., Kutser, T., & Hunter, P.D. (2015). Remote sensing of inland waters: Challenges, progress and future directions. *Remote sensing of Environment, 157*, 1-8

Pearson, R.G., Phillips, S.J., Loranty, M.M., Beck, P.S., Damoulas, T., Knight, S.J., & Goetz, S.J. (2013). Shifts in Arctic vegetation and associated feedbacks under climate change. *Nature Climate Change, 3*, 673-677

Perdrial, J.N., McIntosh, J., Harpold, A., Brooks, P.D., Zapata-Rios, X., Ray, J., Meixner, T., Kanduc, T., Litvak, M., & Troch, P.A. (2014). Stream water carbon controls in seasonally snow-covered mountain catchments: impact of inter-annual variability of water fluxes, catchment aspect and seasonal processes. *Biogeochemistry, 118*, 273-290

Peterson, B.J., Holmes, R.M., McClelland, J.W., Vörösmarty, C.J., Lammers, R.B., Shiklomanov, A.I., Shiklomanov, I.A., & Rahmstorf, S. (2002). Increasing river discharge to the Arctic Ocean. *science, 298*, 2171-2173

Pope, R.M., & Fry, E.S. (1997). Absorption spectrum (380–700 nm) of pure water. II. Integrating cavity measurements. *Applied Optics, 36*, 8710-8723

Powell, M.J. (1968). A FORTRAN subroutine for solving systems of nonlinear algebraic equations. In: Atomic Energy Research Establishment, Harwell (England)

Qiao, H., Tian, Y.Q., Yu, Q., Carrick, H.J., Francek, M., & Li, J. (2017). Snowpack enhanced dissolved organic carbon export during a variety of hydrologic of events in an agricultural landscape, Midwestern USA. *Agricultural and Forest Meteorology, 246*, 31-41

Rawlins, M.A., Steele, M., Holland, M.M., Adam, J.C., Cherry, J.E., Francis, J.A., Groisman, P.Y., Hinzman, L.D., Huntington, T.G., & Kane, D.L. (2010). Analysis of the Arctic system for freshwater cycle intensification: Observations and expectations. *Journal of Climate, 23*, 5715-5737

Raymond, P.A., McClelland, J., Holmes, R., Zhulidov, A., Mull, K., Peterson, B., Striegl, R., Aiken, G., & Gurtovaya, T. (2007). Flux and age of dissolved organic carbon exported to the Arctic Ocean: A carbon isotopic study of the five largest arctic rivers. *Global Biogeochemical Cycles, 21*

Raymond, P.A., Oh, N.-H., Turner, R.E., & Broussard, W. (2008). Anthropogenically enhanced fluxes of water and carbon from the Mississippi River. *Nature, 451*, 449-452

Raymond, P.A., & Oh, N.H. (2007). An empirical study of climatic controls on riverine C export from three major US watersheds. *Global Biogeochemical Cycles, 21*

Rochelle-Newall, E., & Fisher, T. (2002). Chromophoric dissolved organic matter and dissolved organic carbon in Chesapeake Bay. *Marine Chemistry, 77*, 23-41

Romanovsky, V., Sazonova, T., Balobaev, V., Shender, N., & Sergueev, D. (2007). Past and recent changes in air and permafrost temperatures in eastern Siberia. *Global and Planetary Change, 56*, 399-413

Roulet, N., & Moore, T.R. (2006). Environmental chemistry: Browning the waters. *Nature, 444*, 283-284

Roy, D.P., Wulder, M., Loveland, T., Woodcock, C., Allen, R., Anderson, M., Helder, D., Irons, J., Johnson, D., & Kennedy, R. (2014). Landsat-8: Science and product vision for terrestrial global change research. *Remote sensing of Environment, 145*, 154-172

Ruddick, K.G., Gons, H.J., Rijkeboer, M., & Tilstone, G. (2001). Optical remote sensing of chlorophyll a in case 2 waters by use of an adaptive two-band algorithm with optimal error properties. *Applied Optics, 40*, 3575-3585

Ruddick, K.G., Ovidio, F., & Rijkeboer, M. (2000). Atmospheric correction of SeaWiFS imagery for turbid coastal and inland waters. *Applied Optics, 39*, 897-912

Sand-Jensen, K., & Staehr, P.A. (2009). Net heterotrophy in small Danish lakes: a widespread feature over gradients in trophic status and land cover. *Ecosystems, 12*, 336-348

Schuur, E.A., & Abbott, B. (2011). Climate change: High risk of permafrost thaw. *Nature, 480*, 32-33

Schuur, E.A., Bockheim, J., Canadell, J.G., Euskirchen, E., Field, C.B., Goryachkin, S.V., Hagemann, S., Kuhry, P., Lafleur, P.M., & Lee, H. (2008). Vulnerability of permafrost carbon to climate change: implications for the global carbon cycle. *BioScience, 58*, 701-714

Screen, J.A., & Simmonds, I. (2010). The central role of diminishing sea ice in recent Arctic temperature amplification. *Nature, 464*, 1334-1337

Shanmugam, P. (2011). New models for retrieving and partitioning the colored dissolved organic matter in the global ocean: Implications for remote sensing. *Remote sensing of Environment, 115*, 1501-1521

Shi, W., & Wang, M. (2014). Ocean reflectance spectra at the red, near-infrared, and shortwave infrared from highly turbid waters: A study in the Bohai Sea, Yellow Sea, and East China Sea. *Limnology and Oceanography, 59*, 427-444

Siegel, D., Maritorena, S., Nelson, N., Hansell, D., & Lorenzi-Kayser, M. (2002). Global distribution and dynamics of colored dissolved and detrital organic materials. *Journal of Geophysical Research: Oceans (1978–2012), 107*, 21-21-21-14

Siegel, D.A., Wang, M., Maritorena, S., & Robinson, W. (2000). Atmospheric correction of satellite ocean color imagery: the black pixel assumption. *Applied Optics, 39*, 3582-3591

Sinha, E., Michalak, A., & Balaji, V. (2017). Eutrophication will increase during the 21st century as a result of precipitation changes. *science, 357*, 405-408

Smith, L.C., Pavelsky, T.M., MacDonald, G.M., Shiklomanov, A.I., & Lammers, R.B. (2007). Rising minimum daily flows in northern Eurasian rivers: A growing influence of groundwater in the high-latitude hydrologic cycle. *Journal of Geophysical Research: Biogeosciences, 112*

Sobek, S., Tranvik, L.J., & Cole, J.J. (2005). Temperature independence of carbon dioxide supersaturation in global lakes. *Global Biogeochemical Cycles, 19*

Spedding, T., Hamel, C., Mehuys, G., & Madramootoo, C. (2004). Soil microbial dynamics in maize-growing soil under different tillage and residue management systems. *Soil Biology and Biochemistry, 36*, 499-512

Spencer, R.G., Aiken, G.R., Wickland, K.P., Striegl, R.G., & Hernes, P.J. (2008). Seasonal and spatial variability in dissolved organic matter quantity and composition from the Yukon River basin, Alaska. *Global Biogeochemical Cycles, 22*

Spencer, R.G., Stubbins, A., Hernes, P.J., Baker, A., Mopper, K., Aufdenkampe, A.K., Dyda, R.Y., Mwamba, V.L., Mangangu, A.M., & Wabakanghanzi, J.N. (2009). Photochemical degradation of dissolved organic matter and dissolved lignin phenols from the Congo River. *Journal of Geophysical Research: Biogeosciences (2005–2012), 114*

Stedmon, C., Amon, R., Rinehart, A., & Walker, S. (2011). The supply and characteristics of colored dissolved organic matter (CDOM) in the Arctic Ocean: Pan Arctic trends and differences. *Marine Chemistry, 124*, 108-118

Stedmon, C., Markager, S., & Kaas, H. (2000). Optical properties and signatures of chromophoric dissolved organic matter (CDOM) in Danish coastal waters. *Estuarine, Coastal and Shelf Science, 51*, 267-278

Stedmon, C.A., Markager, S., Søndergaard, M., Vang, T., Laubel, A., Borch, N.H., & Windelin, A. (2006). Dissolved organic matter (DOM) export to a temperate estuary: seasonal variations and implications of land use. *Estuaries and Coasts, 29*, 388-400

Stein, R., & Macdonald, R.W. (2004). The organic carbon cycle in the Arctic Ocean

Tarnocai, C., Canadell, J., Schuur, E., Kuhry, P., Mazhitova, G., & Zimov, S. (2009). Soil organic carbon pools in the northern circumpolar permafrost region. *Global Biogeochemical Cycles, 23*

Thingstad, T., Bellerby, R., Bratbak, G., Børsheim, K., Egge, J., Heldal, M., Larsen, A., Neill, C., Nejstgaard, J., & Norland, S. (2008). Counterintuitive carbon-to-nutrient coupling in an Arctic pelagic ecosystem. *Nature, 455*, 387-390

Thompson, D.R., Hochberg, E.J., Asner, G.P., Green, R.O., Knapp, D.E., Gao, B.-C., Garcia, R., Gierach, M., Lee, Z., & Maritorena, S. (2017). Airborne mapping of benthic reflectance spectra with Bayesian linear mixtures. *Remote sensing of Environment, 200*, 18-30

Tian, Y.Q., Yu, Q., Feig, A.D., Ye, C., & Blunden, A. (2013). Effects of climate and land-surface processes on terrestrial dissolved organic carbon export to major US coastal rivers. *Ecological Engineering, 54*, 192-201

Toming, K., Kutser, T., Laas, A., Sepp, M., Paavel, B., & Nõges, T. (2016). First experiences in mapping lake water quality parameters with Sentinel-2 MSI imagery. *Remote Sensing, 8*, 640

Tranvik, L. (2014). Carbon cycling in the Arctic. *science, 345*, 870-870

Uzarski, D., Burton, T., & Genet, J. (2004). Validation and performance of an invertebrate index of biotic integrity for Lakes Huron and Michigan fringing wetlands during a period of lake level decline. *Aquatic Ecosystem Health & Management, 7*, 269-288

Vanhellemont, Q., & Ruddick, K. (2014). Turbid wakes associated with offshore wind turbines observed with Landsat 8. *Remote sensing of Environment, 145*, 105-115

Vanhellemont, Q., & Ruddick, K. (2015). Advantages of high quality SWIR bands for ocean colour processing: Examples from Landsat-8. *Remote sensing of Environment, 161*, 89-106

Verstraeten, A., De Vos, B., Neirynck, J., Roskams, P., & Hens, M. (2014). Impact of air-borne or canopy-derived dissolved organic carbon (DOC) on forest soil solution DOC in Flanders, Belgium. *Atmospheric environment, 83*, 155-165

Vodacek, A., Blough, N.V., DeGrandpre, M.D., Peltzer, E.T., & Nelson, R.K. (1997). Seasonal variation of CDOM and DOC in the Middle Atlantic Bight: Terrestrial inputs and photooxidation. *Limnology and Oceanography, 42*, 674-686

Volpe, V., Silvestri, S., & Marani, M. (2011). Remote sensing retrieval of suspended sediment concentration in shallow waters. *Remote sensing of Environment, 115*, 44-54

Walker, S.A., Amon, R.M., Stedmon, C., Duan, S., & Louchouarn, P. (2009). The use of PARAFAC modeling to trace terrestrial dissolved organic matter and fingerprint water masses in coastal Canadian Arctic surface waters. *Journal of Geophysical Research: Biogeosciences, 114*

Wang, M. (2000). The SeaWiFS atmospheric correction algorithm updates. *SeaWiFS postlaunch calibration and validation analyses, Part, 1*, 57-63

Watanabe, F., Mishra, D.R., Astuti, I., Rodrigues, T., Alcântara, E., Imai, N.N., & Barbosa, C. (2016). Parametrization and calibration of a quasi-analytical algorithm for tropical eutrophic waters. *ISPRS Journal of Photogrammetry and Remote Sensing, 121*, 28-47

Watras, C., Hanson, P., Stacy, T., Morrison, K., Mather, J., Hu, Y.H., & Milewski, P. (2011). A temperature compensation method for CDOM fluorescence sensors in freshwater. *Limnology and Oceanography: Methods, 9*, 296-301

Williams, C.J., Yamashita, Y., Wilson, H.F., Jaffé, R., & Xenopoulos, M.A. (2010). Unraveling the role of land use and microbial activity in shaping dissolved organic matter characteristics in stream ecosystems. *Limnology and Oceanography, 55*, 1159

Williamson, C.E., Morris, D.P., Pace, M.L., & Olson, O.G. (1999). Dissolved organic carbon and nutrients as regulators of lake ecosystems: resurrection of a more integrated paradigm. *Limnology and Oceanography, 44*, 795-803

Williamson, C.E., Stemberger, R.S., Morris, D.P., Frost, T.M., & Paulsen, S.G. (1996). Ultraviolet radiation in North American lakes: attenuation estimates from DOC measurements and implications for plankton communities. *Limnology and Oceanography, 41*, 1024-1034

Willmott, C.J. (2000). Terrestrial air temperature and precipitation: Monthly and annual time series (1950-1996). *WWW url: http://climate. geog. udel. edu/~ climate/html_pages/README. ghcn_ts. html*

Wu, P., Wood, R., & Stott, P. (2005). Human influence on increasing Arctic river discharges. *Geophysical research letters, 32*

Yallop, A., & Clutterbuck, B. (2009). Land management as a factor controlling dissolved organic carbon release from upland peat soils 1: Spatial variation in DOC productivity. *Science of the Total Environment, 407*, 3803-3813

Yang, D., Kane, D.L., Hinzman, L.D., Zhang, X., Zhang, T., & Ye, H. (2002). Siberian Lena River hydrologic regime and recent change. *Journal of Geophysical Research: Atmospheres, 107*

Yang, D., Ye, B., & Kane, D.L. (2004). Streamflow changes over Siberian Yenisei river basin. *Journal of Hydrology, 296*, 59-80

Yang, L., Chang, S.-W., Shin, H.-S., & Hur, J. (2015). Tracking the evolution of stream DOM source during storm events using end member mixing analysis based on DOM quality. *Journal of Hydrology, 523*, 333-341

Yang, W., Matsushita, B., Chen, J., & Fukushima, T. (2011). A relaxed matrix inversion method for retrieving water constituent concentrations in case II waters: The case of Lake Kasumigaura, Japan. *Geoscience and Remote Sensing, IEEE Transactions on, 49*, 3381-3392

Yang, W., Matsushita, B., Chen, J., Yoshimura, K., & Fukushima, T. (2013). Retrieval of inherent optical properties for turbid inland waters from remote-sensing reflectance. *IEEE Transactions on Geoscience and Remote Sensing, 51*, 3761-3773

Yu, Q., Tian, Y.Q., Chen, R.F., Liu, A., Gardner, G.B., & Zhu, W. (2010). Functional linear analysis of in situ hyperspectral data for assessing CDOM in rivers. *Photogrammetric Engineering and Remote Sensing, 76*, 1147-1158

Zhao, J., Barnes, B., Melo, N., English, D., Lapointe, B., Muller-Karger, F., Schaeffer, B., & Hu, C. (2013). Assessment of satellite-derived diffuse attenuation coefficients and euphotic depths in south Florida coastal waters. *Remote sensing of Environment, 131*, 38-50

Zhu, W., Tian, Y.Q., Yu, Q., & Becker, B.L. (2013a). Using Hyperion imagery to monitor the spatial and temporal distribution of colored dissolved organic matter in estuarine and coastal regions. *Remote sensing of Environment, 134*, 342-354

Zhu, W., & Yu, Q. (2013). Inversion of Chromophoric Dissolved Organic Matter From EO-1 Hyperion Imagery for Turbid Estuarine and Coastal Waters. *Geoscience and Remote Sensing, IEEE Transactions on, 51*, 3286-3298

Zhu, W., Yu, Q., Tian, Y., Becker, B., & Carrick, H. (2015). Issues and Potential Improvement of Multiband Models for Remotely Estimating Chlorophyll-a in Complex Inland Waters. *IEEE JOURNAL OF SELECTED TOPICS IN APPLIED EARTH OBSERVATIONS AND REMOTE SENSING*

Zhu, W., Yu, Q., & Tian, Y.Q. (2013b). Uncertainty analysis of remote sensing of colored dissolved organic matter: Evaluations and comparisons for three rivers in North America. *ISPRS Journal of Photogrammetry and Remote Sensing, 84*, 12-22

Zhu, W., Yu, Q., Tian, Y.Q., Becker, B.L., Zheng, T., & Carrick, H.J. (2014). An assessment of remote sensing algorithms for colored dissolved organic matter in complex freshwater environments. *Remote sensing of Environment, 140*, 766-778

Zhu, W., Yu, Q., Tian, Y.Q., Chen, R.F., & Gardner, G.B. (2011). Estimation of chromophoric dissolved organic matter in the Mississippi and Atchafalaya river plume regions using above-surface hyperspectral remote sensing. *Journal of Geophysical Research: Oceans (1978–2012), 116*

Zhulidov, A.V.e. (1997). *Atlas of Russian wetlands: biogeography and metal concentrations*: [Saskatoon]: National Hydrology Research Institute